ALEKSANDRA WROŃSKA

NEAR THRESHOLD η MESON PRODUCTION IN THE $dd \rightarrow {}^4He\eta$ REACTION

A DOCTORAL DISSERTATION
PERFORMED IN THE RESEARCH CENTRE JÜLICH, GERMANY
AND SUBMITTED TO THE FACULTY OF PHYSICS, ASTRONOMY
AND APPLIED COMPUTER SCIENCE
OF THE JAGIELLONIAN UNIVERSITY

THESIS SUPERVISOR:
PROF. DR. HAB. ANDRZEJ MAGIERA

CRACOW 2005

Aleksandra Wrońska

Przyprogowa produkcja mezonu η w reakcji $dd \to {}^4He\eta$

Dysertacja doktorska
wykonana w Centrum Badawczym Jülich, Niemcy
i przedstawiona Radzie Wydziału Fizyki, Astronomii
i Informatyki Stosowanej
Uniwersytetu Jagiellońskiego

Promotor:
Prof. dr hab. Andrzej Magiera

Kraków 2005

Man sieht die Gedanken ihre Hände aus dem Wasser strecken,
man glaubt, sie rufen um Hilfe; wie das täuscht,
sie leben unten innig und sehr vertraut miteinander,
man probiere es doch nur und ziehe einen einzeln heraus!

Widzimy, jak myśli wyciągają ręce z wody,
sądzimy, że wołają o pomoc, cóż za złudzenie,
one żyją pod wodą w zażyłej przyjaźni,
spróbujmy tylko wyciągnąć jedną oddzielnie!

Elias Canetti, *Die Provinz des Menschen*
Elias Canetti, *Prowincja ludzka*

Abstract

The present work is a contribution to the investigation of the η meson interactions. Although the meson has been known for over forty years now, physics issues related to it remain a lively field of nuclear physics.

The experiment, which is the subject of the work, aimed at a measurement of total cross sections and angular distributions of the reaction $\mathrm{dd} \to {}^4\mathrm{He}\eta$ for several excess energies Q. Due to a very small near–threshold total cross section, so far only two experiments succeeded in determination of this quantity for several energies ($Q < 8.4$ MeV). None of them, however, reported on angular distributions. These are important issues in such physics problems as the η production mechanism or existence of η–nucleus quasi–bound states, just to mention a few.

The experiment is thus the first in the world to measure differential cross sections for the $\mathrm{dd} \to {}^4\mathrm{He}\eta$ process. It was performed using the ANKE facility, located at an internal target position of the accelerator COSY in the Institute for Nuclear Physics of Forschungszentrum Jülich, Germany. It comprised measurements at three beam momenta, corresponding to Q–values of -2.6 MeV, 2.6 MeV and 7.7 MeV. The subthreshold measurement was performed for studying the physics background.

The opening chapter presents a brief characterisation of the η meson and a selection of physics problems related to it. Technical details of the detection setup as well as the course of the performed experiment are described in the second chapter. The following part contains a detailed description of methods used in data analysis, including subsequent steps leading to the main goal – determination of total cross sections and angular distributions. In the fourth chapter the major results are given and total cross sections obtained in the experiment are compared to the existing data. Several options of a decomposition into partial amplitudes are discussed along with their consequences concerning determination of the s–wave scattering length. The last chapter gives an outlook for further investigation in the field.

Streszczenie

Niniejsza praca ma na celu wniesienie wkładu w badania oddziaływania mezonu η. Pomimo, iż od odkrycia tej cząstki upłynęło już ponad czterdzieści lat, zagadnienia z nią związane pozostają wciąż w centrum zainteresowania fizyki jądrowej.

Eksperyment będący przedmiotem tej dysertacji miał na celu pomiar całkowitych przekrojów czynnych oraz rozkładów kątowych reakcji $\mathrm{dd} \to {}^{4}\mathrm{He}\eta$ dla kilku energii nad progiem Q. Zapewne to bardzo mały przekrój czynny dla tej reakcji w pobliżu progu sprawił, że dotychchczas jedynie dwie grupy eksperymentalne dokonały jego pomiaru, łącznie przy 10 energiach ($Q < 8.4$ MeV). Jednakże żadna z tych grup nie przedstawiła informacji dotyczących rozkładów kątowych. Te ostatnie są bardzo istotne przy badaniu takich problemów fizycznych jak np. mechanizm produkcji mezonu η czy istnienie stanów związanych mezonu η z jądrami atomowymi.

Przedstawiony eksperyment jest zatem pierwszym, który zaowocował pomiarem różniczkowych przekrojów czynnych dla procesu $\mathrm{dd} \to {}^{4}\mathrm{He}\eta$. Został on wykonany przy pomocy układu pomiarowego ANKE, zlokalizowanego na wewnętrznej wiązce akceleratora COSY w Instytucie Fizyki Jądrowej Centrum Badawczego Jülich w Niemczech. Eksperyment obejmował pomiary przy trzech energiach wiązki, odpowiadających energiom Q wynoszącym -2.6 MeV, 2.6 MeV oraz 7.7 MeV. Pierwszy z tych pomiarów, dokonany poniżej progu zachodzenia reakcji miał na celu zbadanie fizycznego tła.

Pierwszy rozdział tej pracy zawiera krótką charakterystykę mezonu η oraz wybór zagadnień z nim związanych. Szczegóły techniczne układu detekcyjnego, jak również przebieg eksperymentu opisane zostały w rozdziale drugim. Kolejna część zawiera szczegółowy opis metod użytych podczas analizy danych: kolejnych kroków prowadzących do osiągnięcia głównego celu – wyznaczenia przekrojów czynnych i rozkładów kątowych. W czwartym rozdziale zestawione zostały najważniejsze wyniki pracy. Tamże otrzymane całkowite przekroje czynne są porównane z istniejącymi danymi. W rozdziale tym dyskutowane są również możliwości rozkładu na amplitudy cząstkowe i ich konsekwencje dla wyznaczenia długości rozpraszania w fali s. Ostatni rozdział dotyczy perspektyw dalszych badań w tej dziedzinie.

Contents

1 Theory and data overview

The η meson was discovered in 1961 in the bubble chamber data taken at the Lawrence Radiation Laboratory. It manifested itself as an enhancement in the spectrum of the invariant mass of three pions stemming from the reaction $\pi^+ d \rightarrow pp\pi\pi\pi$ [1]. The discovery fitted very well to the Eightfold Way, a model which organised the particles into families, a forerunner of the quark model.

Although since then over 40 years have passed, physics of the η meson is still a lively branch of nuclear physics. Firstly, the properties of the low energy ηN interaction are still far from being well known, although they are very important in the meson–exchange models of the strong interaction. Secondly, this particle is suspected to be not a pure flavour SU(3) state, but a mixture of such states. Its properties, which could allow conclusions to be drawn about the mixing mechanism, are of great interest. They can be investigated either in production reactions or in decays. Apart from that, the η decays give insight into isospin symmetry breaking due to the light quark mass difference, parameters of the QCD triangle, CP violation or transition form–factors. Not known is the η meson production mechanism. Simple models do not reproduce the close–to–threshold data. Last but not least, a strong attractive interaction of the η meson with nucleons and nuclei may lead to a formation of quasi–bound states. Some of the issues will be discussed in the following sections.

1.1 Nature of the η meson

The η meson is one of the particles, whose existence was predicted before their discovery, like the baryon Ω^- [2]. The model with such a strong predictive power was the Eightfold Way proposed by Murray Gell–Mann and Yuval Ne'eman. It classified the known particles into subgroups with respect to their properties. Those subgroups turned out to be mathematically higher representations (multiplets) of the SU(3) symmetry group, which we call nowadays the flavour symmetry. Therefore, assuming the SU(3) symmetry holds, the existence of the lowest non–trivial representation was predicted. The members of this representation are quarks and the Eightfold Way evolved into the quark model.

One of the multiplets comprises pseudoscalar mesons (i.e. $J^P = 0^-$). Its members are plotted in a weight diagram shown in fig. 1.1.

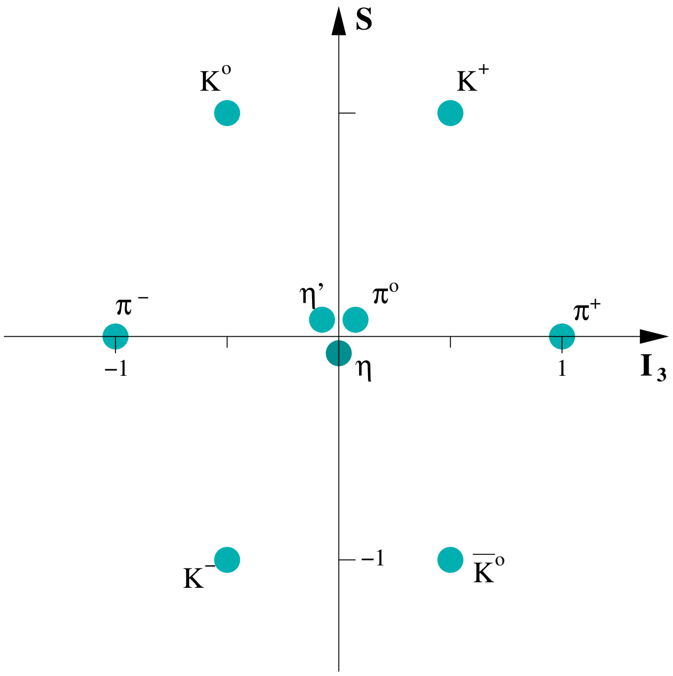

Figure 1.1: The SU(3) nonet of pseudoscalar mesons. The η meson is located in the centre together with two partners.

The η meson, together with two other mesons: π^o and η′ occupies the centre of the diagram. If the mentioned particles were clean eigenstates of the flavour symmetry, their quark contents would be as follows

$$\begin{aligned}\widetilde{\eta} &= (u\bar{u}+d\bar{d}+s\bar{s})/\sqrt{3}\,,\\ \widetilde{\eta}' &= (u\bar{u}+d\bar{d}-2s\bar{s})/\sqrt{6}\,,\\ \widetilde{\pi}^o &= (d\bar{d}-u\bar{u})/\sqrt{2}\,.\end{aligned}$$

The tildas are added to distinguish those from physical states. However, the states realised in nature η, η′ and π^o are considered to be superpositions of the pure SU(3) states listed above. This phenomenon is called meson mixing. It is believed to have two origins: different quark masses and the electroweak interaction [3]. Worth noting is the fact, that $\widetilde{\pi}^o$ has total isospin one, while $\widetilde{\eta}$ and $\widetilde{\eta}'$ have isospin zero. Thus, such mixing violates isospin symmetry. A spectacular evidence of isospin violation is a recent measurement at IUCF of a non–vanishing cross section for the isospin forbidden reaction dd $\rightarrow$ ^{4}Heπ^o [4].

The mass of the η meson reported in the literature varied over years. Different experiments quoted masses differing even by 2 MeV/c^2 (for a review see [5]). The value given by PDG as a valid one for 2002 was 547.3±0.12 MeV/c^2. Hereinafter this value is used in this work for consistency with other experiments. In the update for 2004 new results from the experiment NA48 [6] have been included. This modified the world average which now amounts to 547.75±0.12 MeV/c^2. However, a brand new value of the η mass reported by the GEM collaboration [7] $m_\eta = 547.31 \pm 0.028 \pm 0.032$ MeV/c^2 is consistent with the previously used world–average (however, reducing its error) and thus is questioning the validity of the NA48 result.

1.2 η–Helium systems

The physics of the η meson revived when it was discovered, that the η–nucleus interaction is relatively strong and attractive. In the mid–eighties of the previous century a hypothesis of η–nucleus quasi–bound states was proposed [8–10]. The original predictions based on the optical model approach concerned heavier nuclei (A$>$11). Direct searches for such states with lithium, carbon, oxygen and aluminium, however, proved rather inconclusive [11, 12]. Different theoretical approaches more recently resulted in positive predictions for much lighter nuclei, e.g. helium isotopes [13–17]. Indeed, data on the $\mathrm{pd} \to {}^3\mathrm{He}\eta$ and $\mathrm{dd} \to {}^4\mathrm{He}\eta$ reactions obtained at the SATURNE accelerator in Saclay as well as in other laboratories made some authors claim that already η–helium systems are bound [18, 19].

1.2.1 World data from hadronic reactions

In 1988 Berger and collaborators carried out a measurement at the SATURNE SPESIV spectrometer of the cross section and the deuteron tensor analysing power for the $\vec{\mathrm{d}}\mathrm{p} \to {}^3\mathrm{He}\eta$ reaction near threshold [20]. The η production reaction was identified through the missing mass technique. This measurement, by disclosing an unexpected strength and energy variation of the reaction amplitude near threshold, inspired both theoretical and other experimental groups to undertake research in the field. Soon the SPESIV results were confirmed and supplemented by a measurement at SPESII, covering the excess energy up to approx. 9 MeV [21]. In spite of a refined experimental technique there is, nevertheless, a significant uncertainty in the very–near–threshold points due to energy losses in the target. This is an inherent problem for experiments with external targets with windows. The group reported also results on forward–backward asymmetry, concluding that the distributions are consistent with isotropy.

For $Q > 50$ MeV a pronounced anisotropy was found in the angular distributions presented in [22]. In the measurement carried out at TSL [23] the results obtained in the missing mass technique were verified through the detection in coincidence of photons from the η–decay. They confirmed that the angular distributions are non-isotropic. Also the COSY–11 data exhibit discrepancies from isotropy showing up at $Q \approx 15$ MeV [24]. The striking point to notice about the TSL angular distributions, which have the best precision of the listed data sets, is that the cross sections are maximal for $\cos\theta_\eta \approx +0.5$ rather than in the forward direction, as it is for the π^o production. The data of the other two groups are consistent with the TSL results.

As for the $\mathrm{dd} \to {}^4\mathrm{He}\eta$ reaction, only data on the total cross section exist. They also come from measurements at SATURNE with SPESIV and SPESIII spectrometers [19,25]. In spite of a very good momentum resolution of both spectrometers, small angular acceptance (SPESIV) or insufficient information about the vertical emission angle (SPESIII) prevented the experimentators from extracting the angular distributions. Therefore, no differential cross sections whatsoever are available. Data on total cross sections are restricted to small excess energies ($Q < 9$ MeV).

A summary of the experimental data on η production in $\mathrm{pd} \to {}^3\mathrm{He}\eta$ and $\mathrm{dd} \to {}^4\mathrm{He}\eta$ is to be found in table 1.1.

Observable	Q [MeV]	Comment	Ref.
$\mathrm{pd} \to {}^3\mathrm{He}\eta$			
$\mathrm{d}\sigma/\mathrm{d}\Omega$ & t_{20} $\theta_\eta \approx 0^\circ$ & 180°	$0.05 \leq Q \leq 6.1$	4 energies $\vec{d}$ beam	[20]
$\mathrm{d}\sigma/\mathrm{d}\Omega$	$0.12 \leq Q \leq 6.2$	8 energies angular slope limit	[21,26]
$\mathrm{d}\sigma/\mathrm{d}\Omega$ $\theta_\eta \approx 180^\circ$	$16 \leq Q \leq 712$	16 energies 2–3 angles	[27]
$\mathrm{d}\sigma/\mathrm{d}\Omega$ $14^\circ \leq \theta_\eta \leq 123^\circ$	49	11 angles	[22]
$\mathrm{d}\sigma/\mathrm{d}\Omega$ $\theta_\eta \approx 180^\circ$	$75 \leq Q \leq 163$	4 energies 4 angles/1048 MeV d beam	[28,29]
$\mathrm{d}\sigma/\mathrm{d}\Omega$ $55^\circ \leq \theta_\eta \leq 171.7^\circ$	299	11 angles	[30]
$\mathrm{d}\sigma/\mathrm{d}\Omega$ $36^\circ \leq \theta_\eta \leq 139^\circ$	21.6, 41.1 80.6, 114.8	≈ 25 angles per energy	[23]
$\mathrm{d}\sigma/\mathrm{d}\Omega$	$3 \leq Q \leq 40$	5 energies	[24]
$\mathrm{dd} \to {}^4\mathrm{He}\eta$			
σ_T	$0.3 \leq Q \leq 1.5$	4 energies	[25,31]
σ_T & t_{20}	$0.1 \leq Q \leq 8.4$	6 energies $\vec{d}$ beam	[19]

Table 1.1: Summary of experimental low energy data of the η production on a deuteron. Energy scales (where not quoted directly) were converted to excess energies using $m_\eta = 547.3$ MeV/c^2. The table is a supplemented version of the one from [32].

1.2.2 Reaction amplitude

In order to analyse the available experimental results quantitatively and draw conclusions about the strength of the η–He interaction, a spin averaged reaction amplitude may be extracted using the equation:

$$|f|^2 = \frac{p_i}{p_f}\left(\frac{d\sigma}{d\Omega}\right)_{cm}, \tag{1.1}$$

where p_i and p_f denote the centre–of–mass momenta in the initial and final state, respectively and $\left(\frac{d\sigma}{d\Omega}\right)_{cm}$ stands for the unpolarised cm cross section. The world data for $pd \to {}^3He\eta$ and $dd \to {}^4He\eta$ in terms of this quantity are depicted in fig. 1.2.

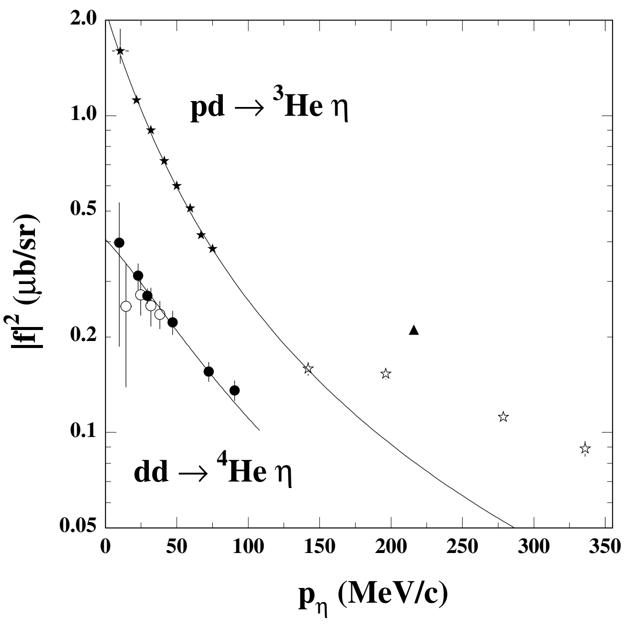

Figure 1.2: Spin and angle averaged reaction amplitudes squared for the $pd \to {}^3He\eta$ and $dd \to {}^4He\eta$ processes versus the cm η momentum. Full and empty stars represent the results from SPESII [21] and TSL [23], respectively. The GEM point [22] (closed triangle) lies well above the trend of the other data. The SATURNE data from the corresponding $dd \to {}^4He\eta$ reaction, shown as open [25] and closed circles [19], have been scaled up by a factor of 10 for display purposes. The curves, taken from ref. [19], result from a combined s–wave optical model fit to near–threshold data from both reactions.

In the case of the $\mathrm{pd} \to {}^3\mathrm{He}\eta$ reaction a striking point to notice is a fall of the amplitude squared by over a factor of three at a small increase of the final cm momentum (from threshold to approx. 70 MeV/c) while remaining isotropic. Such a change in momentum of the produced meson corresponds to a change of only about 9 MeV in the incident beam energy. This rapid fall of the amplitude is therefore associated with a strong interaction of a produced η meson with the recoil nucleus [13]. Worth noticing is also the fact, that the amplitude for the $\mathrm{pd} \to {}^3\mathrm{He}\eta$ process at threshold is comparable with that for the pion production at threshold despite the large momentum transfer.

Both reactions are strongly affected by resonances neighbouring their thresholds. For $\mathrm{pd} \to {}^3\mathrm{He}\eta$ it is the N(1535), which is an s–wave resonance while for $\mathrm{pd} \to {}^3\mathrm{He}\pi^0$ it is Δ(1232), a p–wave resonance. This fact is reflected in the angular dependence of the reaction amplitudes at thresholds. For the $\mathrm{pd} \to {}^3\mathrm{He}\eta$ the production remains isotropic at least up to cm momentum of η of 75 MeV/c [21]. In the case of pion production, a contribution of p–wave in the final state is present as close to threshold as $p_{\pi^0} = 6.4$ MeV/c [33, 34].

1.2.3 Quasi–bound states

A common approximation relating the reaction amplitude and scattering length in case of a weak transition to a channel with a strong final state interaction [35] reads

$$f = \frac{f_B}{pa\cot\delta - ipa}, \tag{1.2}$$

where p denotes the cm momentum of the outgoing particles, δ and a are the s–wave phase shift and the scattering length in the exit channel, respectively. The approximation is valid for the s–wave production (i.e. when s–wave in the final state is allowed by selection rules and no higher partial waves emerge). f_B is a function describing interaction in the initial state and is slowly varying near the reaction threshold, thus approximated by a constant. The usual approximation for the phase shift, neglecting effective range effects [36]

$$\cot\delta = \frac{1}{ap} \tag{1.3}$$

brings the equation 1.2 to the form

$$f = \frac{f_B}{1 - ipa}. \tag{1.4}$$

Thus, experimental investigations of $|f|^2$ provide information about the scattering length. This quantity is an indicator of the existence of a bound state. For bound systems its real part should be negative and relatively large (for the sign the convention of [35] was used). Determination of the total cross section alone, however, provides information about the amplitude squared, i.e.

$$|f|^2 = \frac{f_B^2}{1 + p^2\,|a|^2 + 2p\,\mathfrak{Im}\,a}. \tag{1.5}$$

From such data only the imaginary part and the magnitude of the real part of the scattering length could be extracted. This direct approach cannot provide an evidence but at most a strong hint for a bound state existence. A disadvantage of this approach is that it exploits data from one reaction (not taking into account e.g. related reactions, which could impose certain boundaries) and the real and the imaginary part of the scattering length are strongly coupled in the fit.

Various other theoretical models have been developed during the recent years aiming at the extraction of the scattering length.

Wilkin proposed to use the optical potential model [13] to extract the $\eta^3\mathrm{He}$ scattering length. An input parameter of that model is the η–nucleon scattering length, which was taken from a coupled channels analysis of the πN and ηN around the η threshold as well as from an analysis of the π^0p$\rightarrow \eta$n data within the optical potential model and exploiting the equation 1.5 together. In [13] he found $a(\eta^3\mathrm{He}) = (-2.31 + i\,2.57)\,\mathrm{fm}$.

The same approach used in [19] for a simultaneous analysis of the two allied reactions: $\mathrm{dd} \rightarrow {}^4\mathrm{He}\eta$ and $\mathrm{pd} \rightarrow {}^3\mathrm{He}\eta$ resulted in

$$\begin{aligned} a(\eta^3\mathrm{He}) &= (-2.3 + i\,3.2)\,\mathrm{fm}\,, \\ a(\eta^4\mathrm{He}) &= (-2.2 + i\,1.1)\,\mathrm{fm}\,. \end{aligned}$$

The authors stress that the $\eta^4\mathrm{He}$ system is expected to be more bound than $\eta^3\mathrm{He}$ due to a smaller radius of the $^4\mathrm{He}$ nucleus (rms radii of 1.63 fm and 1.9 fm for $^4\mathrm{He}$ and $^3\mathrm{He}$, respectively) and a presence of an extra nucleon, and this implies

$$|\mathfrak{Re}\, a^{-1}(\eta^4\mathrm{He})| > |\mathfrak{Re}\, a^{-1}(\eta^3\mathrm{He})|\,. \tag{1.6}$$

Another group analysed the available data within the multiple scattering scheme [14]. Using different values of $a(\eta\mathrm{N})$ as input they found that only one gives a reasonable agreement with the $^3\mathrm{He}$ data, but none reproduces the $^4\mathrm{He}$ data. The option which produced the best description of the $^3\mathrm{He}$ data yielded $a(\eta^3\mathrm{He}) = (-0.89 + i\,1.8)\,\mathrm{fm}$. The ηN scattering length employed here gave also $a(\eta^4\mathrm{He}) = (-1.42 + i\,1.3)\,\mathrm{fm}$.

Rakityansky et al. used the finite–rank approximation of the nuclear Hamiltonian [17]. This approximation separates the motion of η from the motion of nucleons inside a nucleus. The latter enters the calculation only in the nuclear wave function. They found that within the uncertainties of the $a(\eta\mathrm{N})$ scattering length all investigated systems, i.e. ηd, ηt, $\eta^3\mathrm{He}$ and $\eta^4\mathrm{He}$ can be bound. Due to some freedom in the choice of parameters, however, it is difficult to quote unique values of $a(\eta^3\mathrm{He})$ and $a(\eta^4\mathrm{He})$ from their work.

Yet a different approach is presented in [15]. The authors investigated the ηt system by solving exactly a four–body problem. The corresponding Fadeev–Yakubovsky equations become solvable when one assumes separable forms of two– and three–body subamplitudes, limiting the basic (two–body) interactions to s–waves only. Their results for a range of $a(\eta\mathrm{N})$ investigated do not support a bound state existence due to a positive real part of the ηt scattering length obtained. The authors argue that the enhancement of the η production cross section (and the reaction amplitude) close to the reaction threshold should be attributed to the existence of a virtual state rather than to a bound state.

As mentioned above, the sign of the real part of the $\eta^3\mathrm{He}$ scattering length is not accessible in 'simple' experiments measuring total cross sections. An interesting possibility to acquire information on this quantity was proposed in [37]. The idea is to exploit the isospin symmetry breaking effects, namely deviation from two of a cross section ratio for the two isospin–related processes: $\mathrm{pd} \to {}^3\mathrm{H}\pi^+$ and $\mathrm{pd} \to {}^3\mathrm{He}\pi^0$. This ratio, or more precisely its energy dependence, carries information about the sought sign. However, the precision and energy range of the existing data are insufficient to draw binding conclusions.

The scattering lengths of $\eta^3\mathrm{He}$ and $\eta^4\mathrm{He}$ systems obtained in the works cited above together with the input values of $a(\eta\mathrm{N})$ are collected in table 1.2.

$a(\eta\mathrm{N})$ [fm]	$a(\eta^3\mathrm{He})$ [fm]	Calculation scheme	Ref.
	$\pm 3.8 + i1.6$	direct fit of $\|f\|^2$	[21]
$0.55 + i0.30$	$-2.31 + i2.57$	optical model	[13]
$0.52 + i0.25$	$-2.3 + i3.2$	optical model^a	[19]
$0.29 + i0.36$	$-0.89 + i1.8$	multiple scattering^b	[14]
$0.476 + i0.279$	$1.89 + i2.6$	multiple scattering	[14]
$0.75 + i0.27$	$4.2 + i5.7$	Fadeev–Yakubovsky	[15]
$0.55 + i0.30$	$2.35 + i1.68$	Fadeev–Yakubovsky	[15]
	$a(\eta^4\mathrm{He})$ [fm]		
$0.52 + i0.25$	$-2.2 + i1.1$	optical model^a	[19]
$0.29 + i0.36$	$-1.42 + i1.30$	multiple scattering^b	[14]
$0.476 + i0.279$	$-2.05 + i1.13$	multiple scattering	[14]

Table 1.2: Scattering lengths of the $\eta^3\mathrm{He}$ and $\eta^4\mathrm{He}$ systems obtained within various model calculations. Where appropriate, input $\eta\mathrm{N}$ scattering length is given.

At a first glance already one notices a wide range of both $\eta\mathrm{He}$ scattering length and the input $\eta\mathrm{N}$ one. Not only that the first value is strongly model dependent, there is also much uncertainty concerning the basic $\eta\mathrm{N}$ interaction. Moreover, a part of data existing at present seem to be the subject of underestimated systematic errors. Such a conclusion has been drawn in ref. [38], where the world collection of data on $\mathrm{pd} \to {}^3\mathrm{He}\eta$ is critically reanalysed. Therein authors also call for new, precision experimental data.

Most of the models described here work in the proximity of the reaction threshold, i.e. assuming s–wave production. Therefore, for their verification appropriate data should be used. In the case of η–$^3\mathrm{He}$ system, thanks to the high–quality CELSIUS data comprising also angular distributions [23] as well as COSY–11 data [24], the onset of higher partial waves has been localised at the excess energy of ca. 15 MeV. As mentioned above, in the case of the η–$^4\mathrm{He}$ system angular distributions are virgin territory and it is not clear which data points should be included in the model calculations. Many of them are based upon an unsaid assumption of an s–wave production.

^{a}simultaneous fit to $^3\mathrm{He}$ and $^4\mathrm{He}$ data
^{b}best description of $^3\mathrm{He}$ data

An important point to make is that the properties of η–He systems should be independent of the way they are produced. However, data from other reactions with such final states are rather scant. Attempts to measure $p^3H \rightarrow {}^4He\eta$ failed due to problems with the tritium target (see [32] and references therein). Data on the η production by bombarding ${}^3He$ with pion beams start only at η cm momentum of 80 MeV/c, so far above threshold [39]. In photoproduction only η^3He system can be produced (η^4He is forbidden due to spin–parity selection rules; an upper limit for the cross section has been determined in [40]). Indeed, the TAPS experiment reported recently very suggestive results on η photoproduction off ${}^3He$ [41]. The group investigated hypothetical η–mesic ${}^3He$ by studying its two decay channels: the coherent η production and the decay into π^op. The extracted binding energy$= (-4.4 \pm 4.2)$ MeV and full width$= (25.6 \pm 6.1)$ MeV of the observed resonance are in line with expectations for an η^3He bound state, see e.g. [42]. The authors of the latter work, however, argue that the data presented in [41] do not unambiguously confirm the η^3He bound state hypothesis but can be also explained by a casp effect. This is due to their insufficient quality and the fact, that they do not resolve the sign problem for the real part of the scattering length.

1.2.4 Reaction mechanism

Dynamics of the η–He systems described in sec. 1.2.3 is a hot topic, but so is the underlying production mechanism. The authors of ref. [43, 44] pointed out, that in contrast to pion production, it is necessary to include three–body processes to explain the strength of the $pd \rightarrow {}^3He\eta$ reaction. They found that one– and two–body mechanisms strongly underestimate the cross section. The η meson is over three times heavier than π^o, which leads to a larger momentum transfer in the η production. Mechanisms involving all three nucleons in the reaction allow sharing the momentum transfer between all nucleons, thus increasing the cross section.

Moreover, Kilian and Nann showed that the kinematics of $pd \rightarrow {}^3He\eta$ exhibit a certain interesting feature, which they called a 'kinematic miracle' [45]. They showed that close to threshold the η momentum is such, as if η was obtained in a sequence of two processes: $pp \rightarrow d\pi^+$ followed by $\pi^+n \rightarrow p\eta$ when there is no relative motion between the final proton and the deuteron. In such 'magic' kinematics p and d tend to form a ${}^3He$ nucleus. Worth noticing is the fact, that in this scenario an intermediate pion is almost on its mass shell and no Fermi momenta are required. Fig. 1.3 shows the graphs illustrating the reaction driven by a two–body mechanism (the so called spectator model, as one of the nucleons does not participate in the reaction) or by the three–body mechanism discussed in [45] called the two–step model (left and right, respectively).

Quantum mechanical calculation of the two–step model confirmed that this scenario significantly enhances the cross section [46]. The authors, using experimentally determined amplitudes for the processes $pp \rightarrow d\pi^+$ and $\pi^+n \rightarrow p\eta$, managed to reproduce the energy dependence of experimental cross section. However, their overall normalisation

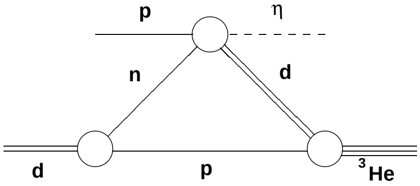

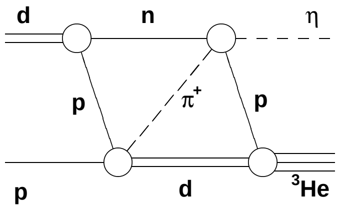

Figure 1.3: Two different ways of producing η^3He final state in pd collisions. Left: spectator model, one of the nucleons is not involved in the process. Right: two–step model, where all nucleons participate. Here there is also a contribution from a similar graph with an intermediate π^0.

was a factor of about 2.8 too small[1]. They ascribe it to omitting in their calculation terms with an intermediate NN singlet state instead of a deuteron or a possible constructive interference with the graph depicted on the left in fig. 1.3.

Subsequently the same group performed calculation for $\mathrm{dd} \to {}^4\mathrm{He}\eta$ assuming that the reaction is a sequence of two processes: $\mathrm{pd} \to {}^3\mathrm{He}\pi^0$ followed by a transmutation step $\pi^o\mathrm{n} \to \mathrm{n}\eta$ [47]. The corresponding graph is shown in fig. 1.4.

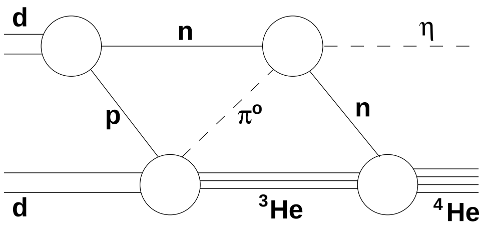

Figure 1.4: Two step model adopted for the reaction $\mathrm{dd} \to {}^4\mathrm{He}\eta$. In fact the calculation comprises eight similar diagrams corresponding to interchanges of neutron to proton, ^{3}He to triton and π^o to π^+ in such a way that charge is conserved.

For this case the obtained result only slightly overshoots the data. This improvement according to the authors may result from the inclusion of all constituents in the nuclear wave function. However, the model can be compared to data only very close to threshold due to lack of data for higher η cm momenta. Also the experimental observation of the onset of higher partial waves could put further constraints on the model [48].

[1] The factor 2.5 given in the original paper has been corrected in [47].

1.2.5 Decomposition into partial amplitudes[2]

To consider the $\mathrm{dd} \rightarrow {}^4\mathrm{He}\eta$ reaction amplitude formally, let us list the properties of the involved particles and introduce the following notation:

particle	cm momentum	spin$^{\text{parity}}$	polarisation
beam d	$\vec{p}$	1^+	$\vec{\varepsilon}_1$
target d	$-\vec{p}$	1^+	$\vec{\varepsilon}_2$
η	$\vec{p_\eta}$	0^-	–
^{4}He	$-\vec{p_\eta}$	0^+	–

besides:
$\vec{L_f}$ – orbital angular momentum in the final state,
$\vec{L_i}$ – orbital angular momentum in the initial state,
$\vec{S}$ – total spin in the initial state.

Due to the presence of two spinless particles in the final state

$$\vec{L_f} = \vec{L_i} + \vec{S}\,, \tag{1.7}$$

while the presence of two identical bosons in the entrance channel implies

$$S + L_i = \text{even}\,. \tag{1.8}$$

Parity conservation requires additionally that

$$L_i - L_f = \text{odd}\,. \tag{1.9}$$

These three equations cannot be satisfied for $S = 0$ and so the only possibilities are ($S = 1$, $L_i =$ odd) and ($S = 2$, $L_i =$ even) with $L_f = L_i \pm 1$ in both cases. The first few partial waves are thus

$$\begin{aligned} &S = 1,\ L_f = 0,\ L_i = 1,\\ &S = 2,\ L_f = 1,\ L_i = 2,\\ &S = 1,\ L_f = 2,\ L_i = 1,3,\\ &S = 2,\ L_f = 3,\ L_i = 2,4. \end{aligned}$$

The amplitude for the $\mathrm{dd} \rightarrow {}^4\mathrm{He}\eta$ reaction must be a pseudoscalar to take account of the parity of the η meson. Thus, it may be constructed of the following four terms, each entering with its own complex weight (amplitudes A', B, C and D) which is a function of $(\vec{p_\eta} \cdot \vec{p})^2$:

$$\begin{aligned} M \;=\;& A'(\vec{\varepsilon}_1 \times \vec{\varepsilon}_2) \cdot \vec{p} \\ +\;& B(\vec{\varepsilon}_1 \times \vec{\varepsilon}_2) \cdot \vec{p_\eta}\,(\vec{p_\eta} \cdot \vec{p}) \\ +\;& C\left[(\vec{\varepsilon}_1 \cdot \vec{p})\,(\vec{\varepsilon}_2 \cdot (\vec{p_\eta} \times \vec{p})) + (\vec{\varepsilon}_2 \cdot \vec{p})\,(\vec{\varepsilon}_1 \cdot (\vec{p_\eta} \times \vec{p}))\right] \\ +\;& D\left[(\vec{\varepsilon}_1 \cdot \vec{p_\eta})\,(\vec{\varepsilon}_2 \cdot (\vec{p_\eta} \times \vec{p})) - (\vec{\varepsilon}_2 \cdot \vec{p_\eta})\,(\vec{\varepsilon}_1 \cdot (\vec{p_\eta} \times \vec{p}))\right]\,. \end{aligned} \tag{1.10}$$

[2] This section is a result of collaboration with C. Wilkin.

Letting $\vec{p}$ lie along the z–axis and $\vec{p_\eta}$ lie in the x–z plane, $\vec{p_\eta} = p_\eta(\sin\theta, 0, \cos\theta)$, implies that $\vec{p_\eta} \times \vec{p} = -p_\eta p \sin\theta\,(0,1,0)$. Then the amplitude M reads

$$
\begin{aligned}
M &= A' p\,(\vec{\varepsilon}_1 \times \vec{\varepsilon}_2)_z \\
&+ B p_\eta^2 p \cos\theta\,[(\vec{\varepsilon}_1 \times \vec{\varepsilon}_2)_z \cos\theta + (\vec{\varepsilon}_1 \times \vec{\varepsilon}_2)_x \sin\theta] \\
&- C p_\eta p^2 \sin\theta\,[\varepsilon_{1z}\varepsilon_{2y} + \varepsilon_{2z}\varepsilon_{1y}] \\
&- D p_\eta^2 p \sin\theta\,[(\varepsilon_{1z}\cos\theta + \varepsilon_{1x}\sin\theta)\,\varepsilon_{2y} - (\varepsilon_{2z}\cos\theta + \varepsilon_{2x}\sin\theta)\,\varepsilon_{1y}]\,. \qquad (1.11)
\end{aligned}
$$

Introducing $A = A' + B p_\eta^2 \cos^2\theta$ one obtains

$$
\begin{aligned}
M &= A p\,(\vec{\varepsilon}_1 \times \vec{\varepsilon}_2)_z \\
&+ B p_\eta^2 p \sin\theta \cos\theta (\vec{\varepsilon}_1 \times \vec{\varepsilon}_2)_x \\
&- C p_\eta p^2 \sin\theta\,[\varepsilon_{1z}\varepsilon_{2y} + \varepsilon_{2z}\varepsilon_{1y}] \\
&- D p_\eta^2 p \sin\theta\,[(\varepsilon_{1z}\cos\theta + \varepsilon_{1x}\sin\theta)\,\varepsilon_{2y} - (\varepsilon_{2z}\cos\theta + \varepsilon_{2x}\sin\theta)\,\varepsilon_{1y}]\,. \qquad (1.12)
\end{aligned}
$$

The term proportional to C is the only one that changes sign under $\vec{p_\eta} \to -\vec{p_\eta}$ and thus represents odd partial waves p, f, *etc.* The term multiplied by A has no explicit angular dependence, unless in A itself. Therefore it is the only one which can comprise the s–wave contribution. The terms proportional to B and D contain higher even partial waves. Therefore at threshold only the A–term survives. Since this depends upon the x and y components of $\vec{\varepsilon}_1$, only $m_1 = \pm 1$ is allowed and so the tensor analysing power $t_{20} = +1/\sqrt{2}$ at threshold[3].

Furthermore, because the A and B terms are proportional to different components of the cross product of the deuteron polarisation vectors, there is no A–B interference for the unpolarised cross section nor for t_{20}. This is a mathematical depiction of the fact that the cross section has to be symmetric under $\theta \rightleftharpoons \pi + \theta$. There can be no terms linear in $\sin\theta$ or $\cos\theta$ here.

On the track to evaluate the unpolarised cross section define the auxiliary quantity averaged over the spin direction of the target deuteron:

$$
Z = \tfrac{1}{3} \sum_{m_2} M^\dagger M\,. \qquad (1.13)
$$

Let us consider the p–wave term contribution to Z as an example. It reads

$$
\begin{aligned}
Z_C = \tfrac{1}{3} \sum_{m_2} M_C^\dagger M_C &= \tfrac{1}{3} |C|^2 p_\eta^2 p^4 \sin^2\theta \sum_{m_2} (\varepsilon_{1z}\varepsilon_{2y} + \varepsilon_{2z}\varepsilon_{1y})^\dagger\,(\varepsilon_{1z}\varepsilon_{2y} + \varepsilon_{2z}\varepsilon_{1y}) \\
&= \tfrac{1}{3} |C|^2 p_\eta^2 p^4 \sin^2\theta \left(\varepsilon_{1z}^\dagger \varepsilon_{1z} + \varepsilon_{1y}^\dagger \varepsilon_{1y}\right)\,. \qquad (1.14)
\end{aligned}
$$

The first term contributes to the $m_1 = 0$ cross section while the second corresponds to the $m_1 = \pm 1$ terms in equal amounts. The other two terms to the order p_η^2 contributing to Z,

[3] The tensor analysing power is defined by the formula:
$\sqrt{2} t_{20} = [\mathrm{d}\sigma(m_1 = 1) + \mathrm{d}\sigma(m_1 = -1) - 2\mathrm{d}\sigma(m_1 = 0)]\ /\ \sum_{m_1} \mathrm{d}\sigma(m_1)\,.$

i.e. the $|A|^2$ term and the A^*D interference add to the $m_1 = \pm 1$ cross section and vanish for $m = 0$.

Averaging over the spin directions of the beam deuteron as well:

$$W = \tfrac{1}{9} \sum_{m_1,m_2} M^\dagger M \tag{1.15}$$

and keeping terms to order p_η^2 leads to three contributions

$$\begin{aligned} W_C &= \tfrac{1}{3}\sum_{m_1} Z_C = \tfrac{2}{9}|C|^2 p_\eta^2 p^4 \sin^2\theta\,, & (1.16)\\ W_A &= \tfrac{1}{9}\sum_{m_1 m_2} |A|^2 p^2 (\vec{\varepsilon}_1^{\,\dagger} \times \vec{\varepsilon}_2^{\,\dagger})_z (\vec{\varepsilon}_1 \times \vec{\varepsilon}_2)_z = \tfrac{2}{9}|A|^2 p^2\,, & (1.17)\\ W_{AD} &= -\tfrac{1}{9}\sum_{m_1 m_2} 2\mathfrak{Re}(A^*D) p_\eta^2 p^2 \sin^2\theta \left[(\vec{\varepsilon}_1^{\,\dagger} \times \vec{\varepsilon}_2^{\,\dagger})_z\,(\varepsilon_{1x}\varepsilon_{2y} - \varepsilon_{2x}\varepsilon_{1y})\right] & \\ &= -\tfrac{4}{9}\mathfrak{Re}(A^*D) p_\eta^2 p^2 \sin^2\theta\,, & (1.18) \end{aligned}$$

and so

$$W = \tfrac{2}{9}p^2\left[|A|^2 - 2\mathfrak{Re}(A^*D)p_\eta^2 \sin^2\theta + |C|^2 p_\eta^2 p^2 \sin^2\theta\right]. \tag{1.19}$$

In order to separate the s–wave contribution A is split into an isotropic and an angle–dependent part, which to order p_η^2 gives

$$|A|^2 \longrightarrow |A_0|^2 + 2\mathfrak{Re}(A_0^* A_2)\,(\vec{p}\cdot\vec{p_\eta})^2 \tag{1.20}$$

while the A^*D becomes A_0^*D. The differential cross section formula depends on the normalisation that one chooses for the amplitudes. Let us take

$$\begin{aligned} \frac{d\sigma}{d\Omega} = \frac{p_\eta}{p} W &= \tfrac{2}{9} p p_\eta \left[|A_0|^2 + 2\mathfrak{Re}(A_0^* A_2)\, p^2 p_\eta^2 \cos^2\theta\right. \\ &\qquad \left. - 2\mathfrak{Re}(A_0^* D) p_\eta^2 \sin^2\theta + |C|^2 p^2 p_\eta^2 \sin^2\theta\right]\,, \end{aligned} \tag{1.21}$$

where $|A_0|^2$, containing the s–wave η–^{4}He final state interaction, still varies with p_η^2.

Hence, any deviation from isotropy in the unpolarised differential cross section, though clearly indicating presence of higher partial waves, can arise either from the square of the $L_f = 1$ amplitude or the interference between the $(L_f, L_i) = (0,1)$ and the $(L_f, L_i) = (2,1)$ or $(2,3)$ amplitudes.

However, it is worth noticing that the tensor analysing power for the pure p–wave production deduced from eq. 1.14 amounts to $t_{20} = -1/2\sqrt{2}$, while the $|A_0|^2$ and the A_0^*D terms both have $t_{20} = 1/\sqrt{2}$. Thus, the p–waves could be isolated by measuring this quantity.

2 Experiment

The experiment which is described in this work was performed in the Institute for Nuclear Physics of the Forschungszentrum Jülich, Germany. The institute hosts a synchrotron COSY, capable of delivering proton and deuteron beams. The measurement was done with the use of the ANKE facility. The preparation of experimental programme concerning the study of the η production in the $\mathrm{dd} \to {}^4\mathrm{He}\eta$ was launched in autumn 2002.

In the reaction $\mathrm{dd} \to {}^4\mathrm{He}\eta$ two particles are produced, one neutral and one of charge two. As there is no appropriate high–acceptance detector of neutral particles at COSY, the principle of the measurement assumed detection of ${}^4\mathrm{He}$ particles and reconstruction of its momentum followed by the reconstruction of a momentum four–vector of the accompanying particle.

2.1 Experimental environment

2.1.1 COSY

COSY stands for a cooler synchrotron, which is operated in Forschungszentrum Jülich, Germany [49]. Fig. 2.1 on the following page is a schematic sketch of this synchrotron, together with the experiments using an internal or extracted beam of COSY, as well as the injection cyclotron JULIC.

COSY delivers polarised and unpolarised proton and deuteron beams of momenta from 0.3 GeV/c to 3.7 GeV/c. In the standard operation the number of particles stored in the ring reaches 10^{11}. The synchrotron is equipped with two cooling systems, the electron cooling working in the lower momentum regime and the stochastic cooling for beams of higher momenta. They ensure small momentum spread and a small emitance of a beam.

The first tests with injection and acceleration of deuterons in COSY were performed in 2000 [50]. The achieved intensities of the deuteron beam were at least as good as in the case of protons. Since autumn 2003 also the option of a polarised deuteron beam has been available. The technical data of COSY are collected in table 2.1.

COSY delivers beams to four experiments located at internal target stations: COSY–11, PISA, ANKE and EDDA. There are three more experimental installations: BIG KARL, COSY–TOF and JESSICA which use the extracted beam.

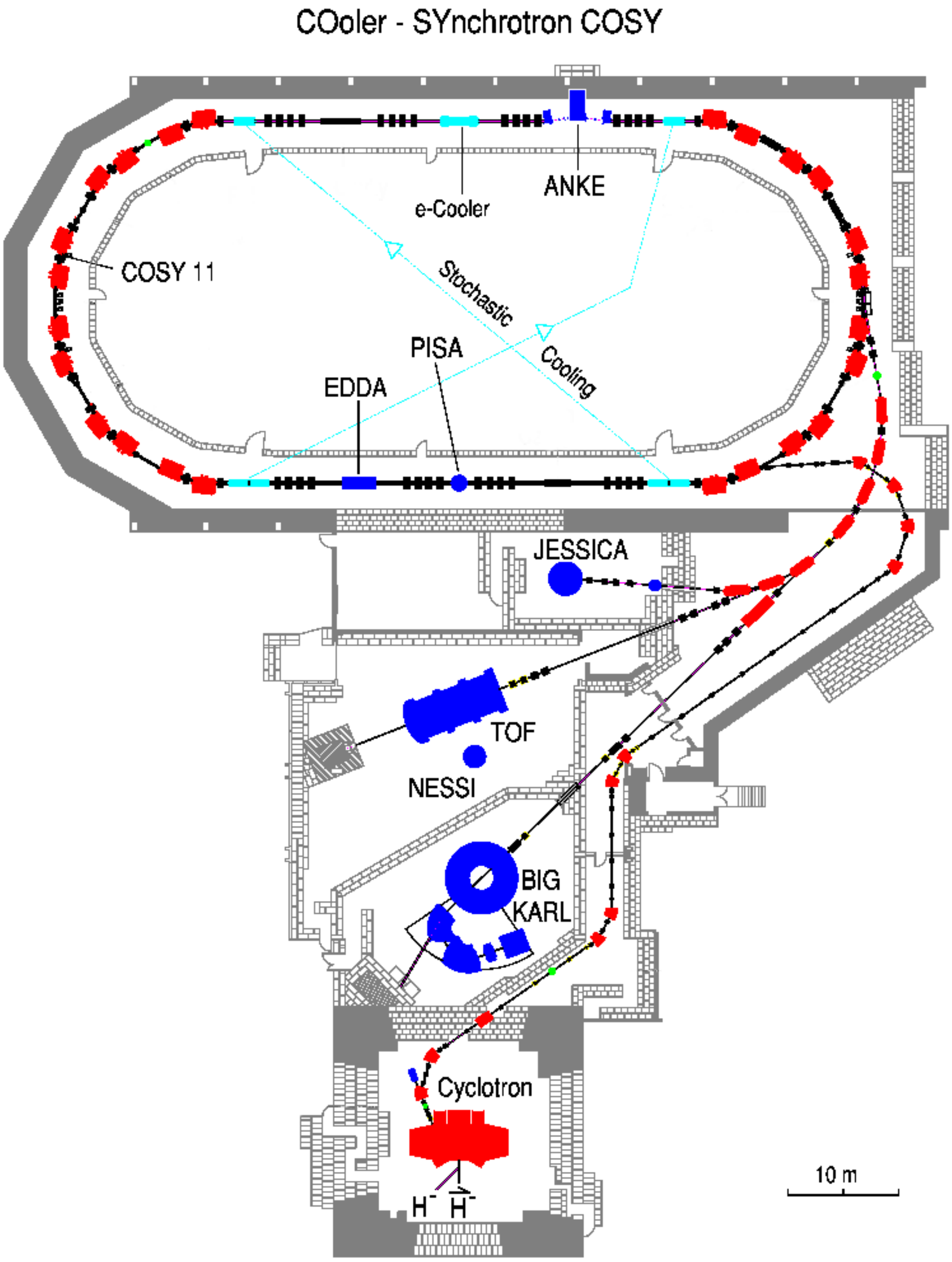

Figure 2.1: The view of the COSY–facility.

feature	description
circumference	184 m
number of magnets	24 dipoles, 54 quadrupoles
momentum range	0.3 GeV/c – 3.7 GeV/c
cooling	electron (p_{beam} <290 MeV/c)
	stochastic (p_{beam} >1.5 GeV/c)
momentum spread	10^{-3} without cooling
	10^{-4} with cooling
number of particles stored	10^{11} (uncooled, unpolarised)

Table 2.1: Specifications for the COSY synchrotron.

2.1.2 ANKE

ANKE is one of the internal experiments at COSY. Its name is an abbreviation of the **A**pparatus for studies of **N**ucleon and **K**aon **E**jectiles. A detailed description can be found in [51]. In the following the main features of ANKE are discussed. The detection system, see fig. 2.2, is based on three magnets D1–D3, forming a chicane in the COSY ring. The target position is located between D1 and D2. Currently there are two options available: a strip target and a cluster jet target [52]. While the first is used for nuclear targets, the latter can be operated with hydrogen or deuterium. A third option will soon be available. The Polarised Internal Target [53], providing polarised hydrogen and deuterium, will be installed in the COSY ring in June 2005.

The D2 magnet serves as a spectrometer. It bends the charged particle trajectories into the different detector installations. One can distinguish five independent detection subsystems:

Positive Side Detector (PD) located in the focal plane of D2. It comprises an array of range telescopes, a set of scintillation counters for time of flight (TOF) measurement and a set of multiwire proportional chambers for tracking. Its acceptance covers forward angles at a rigidity range from about 200 MeV/c to 1400 MeV/c.

Negative Side Detector (ND) serves for detection of negatively charged particles. It consists of scintillation counters for energy loss and TOF measurement as well as tracking detectors (multiwire proportional chambers) allowing momentum reconstruction.

Backward Detector (BD) detects backward emitted, positively charged particles of rigidity between 300 MeV/c and 600 MeV/c. It consists of drift chambers and a scintillation hodoscope.

Vertex Detector (VD) is a near–target detector, mounted in the target vacuum chamber. It comprises 3 layers of silicon strip detectors and provides the position and energy loss information. It is used to detect spectator protons in the measurements of quasi–free reactions on the deuteron target and for the luminosity determination.

Forward Detection System (FD) serves for detection of fast, positively charged ejectiles. It covers rigidities between about 0.5 GeV/c and 2.5 GeV/c (depending

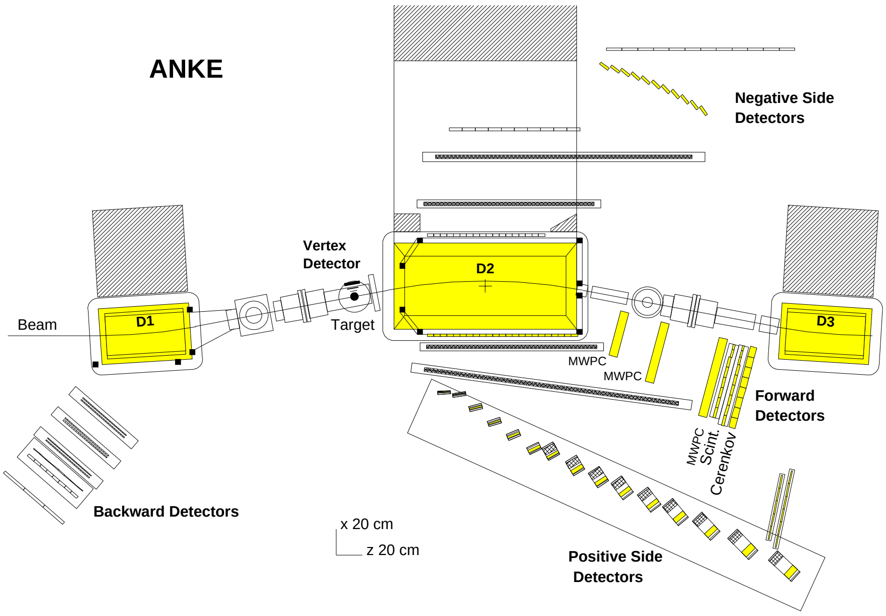

Figure 2.2: The floor view of ANKE.

on the spectrometer setting) and provides information on energy loss, tracking and Čerenkov effect. This part of ANKE was exploited in the $dd \to {}^4He\eta$ measurement, therefore its detailed description is provided in the next section.

2.1.3 Forward Detection System

The standard layout of the FD system comprises tracking detectors, energy loss and Čerenkov detectors. For beam momenta close to threshold for $dd \to {}^4He\eta$ all the ${}^4He$ particles produced in this process propagate forward in the laboratory system and are in the acceptance of the FD system, where they can be detected. The layout of the Forward Detection System and examples of ${}^4He$ trajectories are plotted in fig. 2.3.

For the energy loss measurement a two–layer scintillation hodoscope is used. The first layer consists of 8 and the second one of 9 counters. The second layer is shifted half–width with respect to the first layer. Both are mounted on the common support structure, separated by a 5 cm gap. The counters height is 36 cm, the width and thickness for most of the counters are 8 cm and 2 cm, respectively, except for 2 counters in the first layer and 3 counters in the second one, in the high momentum side. Their thickness is reduced to 1.5 cm and, due to a higher count rate in this region (proximity of the beam), their width decreases gradually to 4 cm. After gaining the experience in a calibration run, the hodoscope was supplemented by an additional layer of counters. One of the PD detectors was placed behind the hodoscope. That layer of six scintillation counters, each having the

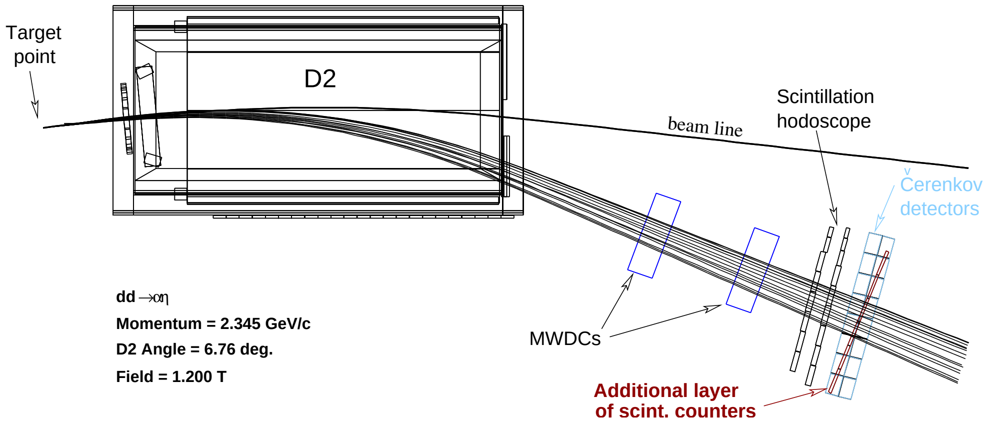

Figure 2.3: Forward Detection System and its modifications: the new pack of MWDCs and the additional layer of scintillation counters in the former location of the Čerenkov detectors. Several trajectories of ^{4}He particles produced in dd $\rightarrow$ ^{4}Heη at p_{beam}=2.345 GeV/c are shown.

dimensions of 10 cm $\times$ 100 cm $\times$ 1 cm, was moved to a position, previously occupied by the Čerenkov detectors. Although this detector was not employed in the trigger, it provided additional information (time and energy loss) necessary for the ^{4}He identification in the off–line analysis.

Tracking in FD in the standard operation mode is realised with the use of three multiwire proportional chambers. Each chamber contains two wire planes (oriented vertically and horizontally) with wire spacing of 1 mm as well as 2 inclined strip planes with the strip width of about 4 mm. The typical position resolution achieved is 1.2 mm. However, about half a year before the scheduled beam time the aging effects in the existing set of chambers became very significant. Their efficiency was very unstable and low. As a replacement for MWPCs, a pack of two multiwire drift chambers (MWDCs) was first tested (see sec. 2.2.2) and finally used in the measurement. The chambers were constructed in Cracow as a prototype of a larger installation [54]. However, due to their satisfactory operation, they became alternately parts of the COSY–11 and GEM setups. This set of 2 MWDCs is constructed in a 'sandwich–like' form: the chambers are fixed in an aluminium frame. Therefore they are easily movable without losing their relative adjustment. Each chamber consists of 4 identical planes, 2 with wires oriented vertically and 2 with horizontal wire orientation. A plane layout is shown in fig. 2.4. There are 16 cells of the width of 2 cm in each plane, which determines the active area of 32 cm $\times$ 32 cm. The double sense wire construction resolves the left–right ambiguity and makes the cell orientation opposite for neighbouring cells. The working conditions for the chambers are the following: the voltage on the cathode wires set to -2100 V, on sense wires to 2250 V, the gas mixture consisting of equal parts of ethane and argon with a small admixture of ethanol.

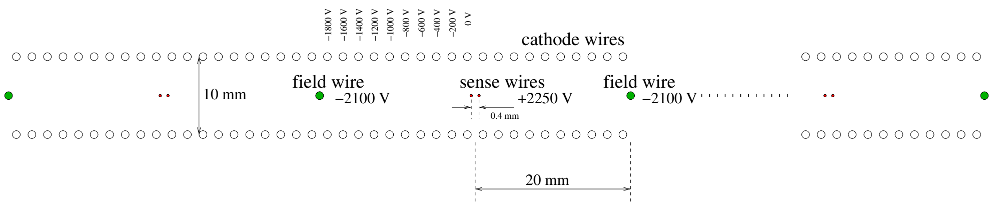

Figure 2.4: Layout of a sensitive plane in MWDCs used in the experiment. Thanks to the double–sense–wire construction cells are single–sided, which allows one to avoid a left–right ambiguity.

2.1.4 Electronics and trigger

Each counter of the forward hodoscope is read out via two photomultipliers (PMs), providing the amplitude and the time information. This allows vertical position reconstruction from the difference of upper and lower times. Additionally, home made discriminators (RALEX) are used to refine the counter timing information by constructing a mean time [55].

There is also a possibility to use the information on the sum of amplitudes from both PMs for each counter on the electronic level (i.e. trigger construction). This is realised by analog integrators [56]. An integrator module contains 9 identical channels, each having a pair of analog inputs and a logic output. A principle of operation is shown in fig. 2.5.

The module for each channel integrates signals from both inputs within a certain time gate and adds them. Then the result signal is discriminated. The discrimination threshold can be set individually for each channel. The way of processing of information from a counter on the electronic level is schematically shown in fig. 2.6. Both RALEX and the integrator modules are used to make an efficient use of the energy loss and timing information. The first one was used to construct the minimum bias trigger (T2), which was used to collect data for particles characterised by a small energy loss in the hodoscope for calibration purposes. The cross section for processes in which protons and deuterons are produced exceed those for helium production by orders of magnitude. Therefore a sufficient statistics could be collected even with an additional prescaling factor imposed on this trigger, which had the advantage of reducing total trigger rate, i.e. increasing the efficiency of the data acquisition system (DAQ). The option with integrators was a basis for the main ^{4}He trigger (T1). It was applied only for the counters of the first two hodoscope layers. This reduced the count rate to a level acceptable by the ANKE DAQ; therefore the additional counters were not employed in this trigger. An additional trigger (T4) was used to read out the scalers information. Scalers are used e.g. for online monitoring and off–line dead time corrections. Fig. 2.7 explains the trigger logic.

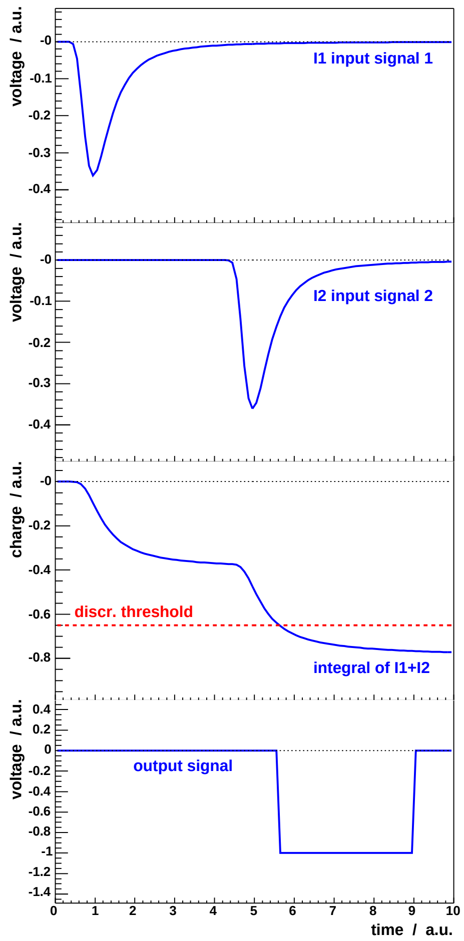

Figure 2.5: Principle of operation of an integrator module. Two analog input signals are integrated and the integral is discriminated. A discrimination threshold is settable for each of the nine channels independently.

2.2 Preparation

2.2.1 GEANT simulations

The simulation showed, that the ANKE acceptance for ^{4}He from dd $\to$ ^{4}Heη is close to 100% up to a Q–value of 6.6 MeV and a coverage of the full polar angle is provided up to a Q–value of 90 MeV. The response of the ANKE setup was simulated using the GEANT simulation package [57, 58]. The capability of ^{4}He identification and the momentum resolution of the system was checked. To test the first feature, the energy losses of ^{4}He particles were simulated and compared with those of the potential background

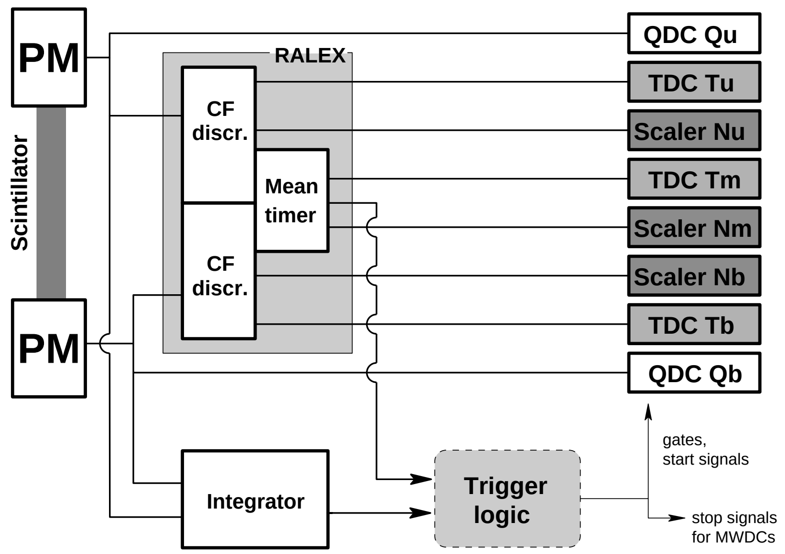

Figure 2.6: Scheme of the electronics serving one hodoscope counter.

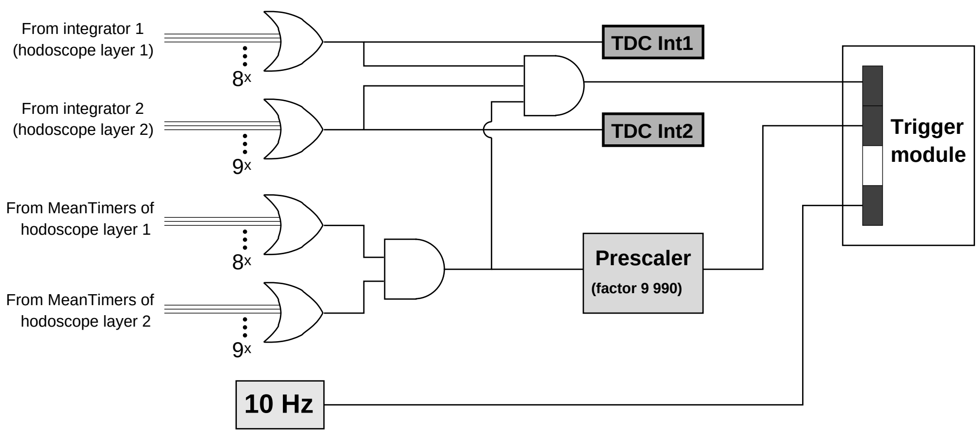

Figure 2.7: Scheme of the trigger logic.

particles: ^{3}He, tritons, deuterons and protons. The result is shown in fig. 2.8. The particles are very well separated. Even for the cross section for ^{3}He production higher by 2 orders of magnitude than the cross section for ^{4}He production both particle types can be very well distinguished. The energy loss of ^{4}He is about 8 times higher than that of protons and about 4 times higher than that of deuterons of the same rigidity. This indicates, that the combined energy loss – rigidity cut, applied together with the similar one for the second

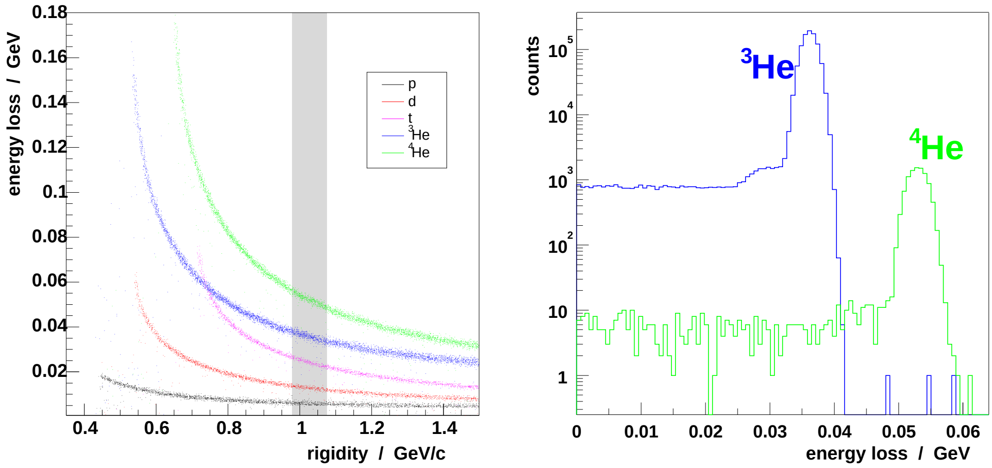

Figure 2.8: Simulated energy losses for ^{4}He particles in the first layer of the hodoscope, in the left figure plotted as a function of rigidity and compared with energy losses of potential background particles. Comparison of energy losses of ^{4}He and ^{3}He particles in the rigidity region of interest (shaded in the left panel) is shown in the right figure.

layer allow a clear identification of the ^{4}He particles.

A crucial feature of a setup when measuring close to threshold is its momentum resolution. The spatial resolution of the MWPCs was known to be 1.2 mm from previous experiments. The extension of the interaction region is determined by the target dimensions in the horizontal plane: 5 mm in both x– and z–directions, while in the y–dimension it is limited by the beam size (approximately 7 mm FWHM)[1]. Taking this information into consideration as well as the physics processes i.e. multiple scattering and energy losses, the momentum and missing mass resolution of the FD setup for $dd \to {}^4\mathrm{He}\eta$ at a beam momentum of 2.345 GeV/c were simulated. The results are collected in table 2.2.

quantity	resolution (FWHM)
total momentum	61 MeV/c
longitudinal momentum	59 MeV/c
transverse momentum	15 MeV/c
missing mass	2.2 MeV/c^2
cm polar angle	19°

Table 2.2: Resolution of the FD setup simulated for a beam momentum of 2.345 GeV/c.

[1]The target coordinate system is oriented as follows: z axis is along the beam direction, y–axis is vertical, oriented upwards, x–axis points out of the COSY ring.

The question of feasibility of the reaction identification can be answered only in the context of the physics background. In the case of the $\mathrm{dd} \rightarrow {}^4\mathrm{He}\eta$ reaction this is considered to be mainly two pion production [59, 60]. In the simulation this background was generated with the use of the package Pluto++ [61], on the basis of parametrised data taken from [62]. Fig. 2.9 shows missing mass and transverse momentum distributions of ${}^4\mathrm{He}$ particles detected in FD setup. The cross sections assumed for simulations were 2 μb and 16 nb for background and signal, respectively.

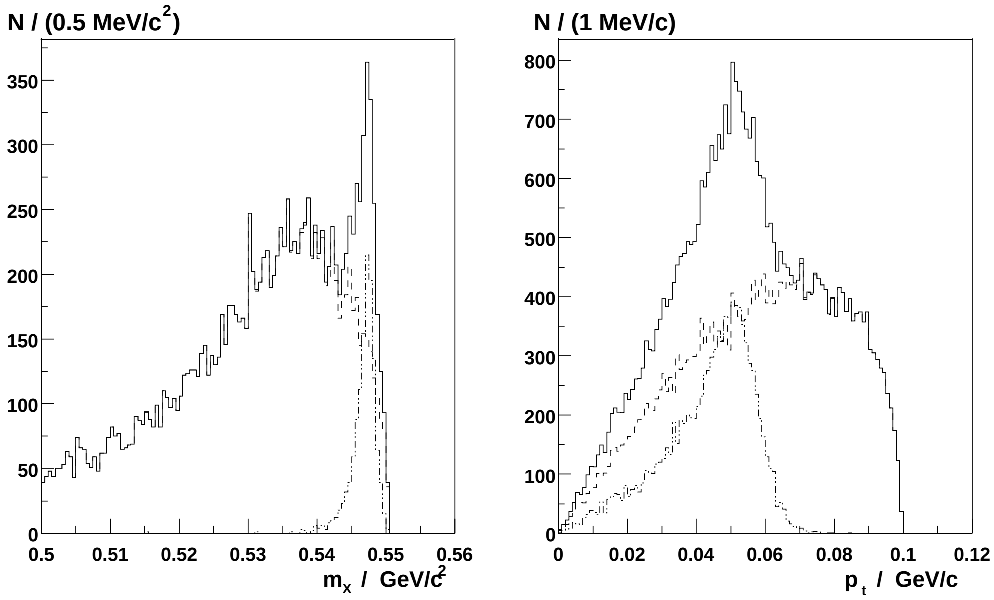

Figure 2.9: Results of the simulation of $\mathrm{dd} \rightarrow {}^4\mathrm{He}\eta$ and background at a beam momentum of 2.345 GeV/c. Left: missing mass distribution (1/10 of an expected two–day statistics). Right: transverse momentum spectrum for events with $\mathrm{m}_X > 0.54$ GeV/c. In both cases the dashed–dotted histogram indicates the signal and the dashed one background from 2–pion production.

Both spectra reveal enhancements stemming from the $\mathrm{dd} \rightarrow {}^4\mathrm{He}\eta$ reaction. Thus, the position resolution of 1.2 mm, which was assumed for simulations, is sufficient to identify the reaction channel of interest. From the distribution of the transverse momentum, the η meson cm momentum can be determined in a way independent of the information on beam momentum provided by COSY, with a similar accuracy (about 5 MeV/c).

2.2.2 Test of drift chambers

For operation of drift chambers at ANKE, two points needed to be checked. One is the count rate capability (up to 10^6/s), the other one is a possible modification of the chamber response due to the presence of a magnetic field. A test measurement was performed in

September 2002. To accomplish the two goals, the test was split into two parts. First, there was no magnetic field switched on and the count rate effect was studied exclusively. In the second part data at various beam intensities were taken with magnetic field switched on. A comparison of the drift time spectra for wire plane 1 (closest to D2, the strongest stray magnetic field) obtained with and without the presence of a magnetic field, as well as the resulting calibrations[2], leads to a conclusion that the differences are very small (well within the chambers resolution assumed for simulations) and can be neglected.

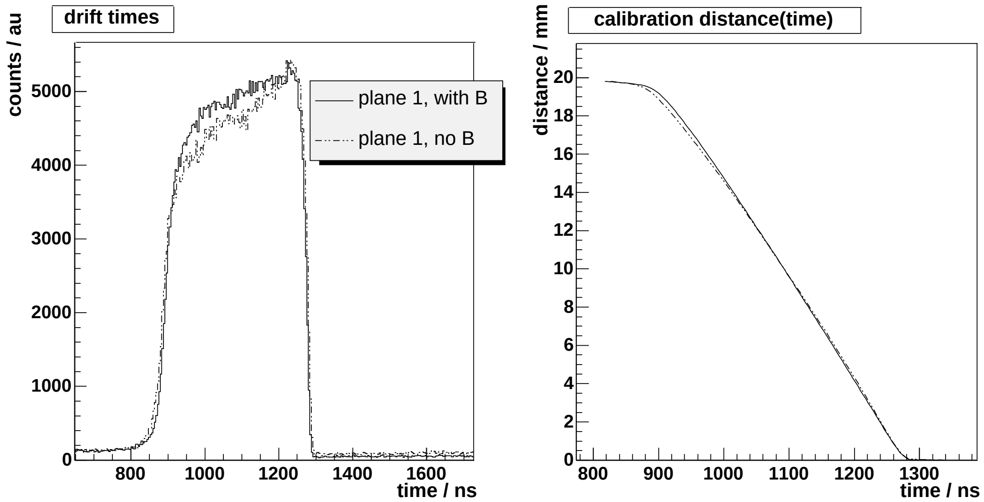

Figure 2.10: Characteristics of the drift chamber: drift time spectra (left) and corresponding calibrations (right). Dotted line indicates data taken without magnetic field, solid line represents data obtained with magnetic field on.

To find a calibration, i.e. a function mapping measured times to positions, the autocalibration method was used [63]. The procedure is described in detail in the next chapter, sec. 3.2.1. It relies only on a shape of a drift time spectrum and the assumption, that the particle flux is uniformly distributed over the cells. In case of these chambers this assumption is in practice always fulfilled. Thanks to their unique construction, when summing up the distributions for all cells within one plane, due to different cell orientation of even and odd cells, one obtains in most cases a uniform distribution.

Concerning the second investigated aspect, the increase of count rate manifested itself in the increase of the accidental background, visible on both sides of the regular drift time spectrum. This effect results in a reduced probability to unambiguously identify single–track events. However, this reduction is relatively small and does not balance the gain in the number of registered events from the increased luminosity. Thus, the limitation in count rate for the MWDCs operation comes only from the current induced on the sense

[2]In context of drift chambers, the calibration means a function mapping drift time to a distance from a sense wire.

wires. The upper limit of 22 μA was reached at a count rate of $1.3 \cdot 10^6$ /s in the forward hodoscope.

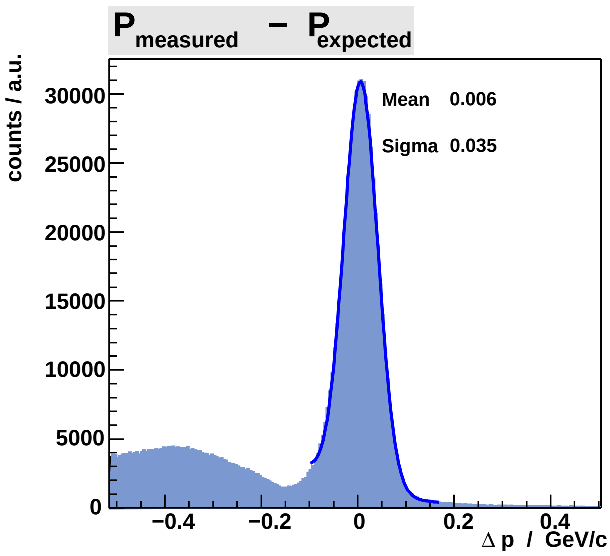

Figure 2.11: Deviation of the reconstructed momenta from the values predicted by kinematics of pp elastic scattering.

As the measurements were done with a 2.085 GeV/c proton beam and solid state targets (C, CH_2), the dominating processes were free– and quasi–free scattering. Hence, the results of the momentum reconstruction were compared with the expectations based on the kinematics of the proton–proton elastic scattering. Fig. 2.11 shows the difference between the reconstructed momentum and the expected value. The distribution reveals a clear peak around zero, with an achieved resolution of σ=1.7%. These are the events obeying kinematics of the proton–proton quasi–free scattering. To the left, a bump originating from multi–body final states is visible.

The outcome of the test was that the tested drift chambers were appropriate for use in the forward region of ANKE. They were operational at the typical count rates. The χ^2 distribution pointed at a position resolution better than the primarily assumed 1.2 mm. The resolution was not significantly affected by the presence of a magnetic field.

2.2.3 Calibration of integrators

Another auxiliary run before the production measurement of $dd \rightarrow {}^4He\eta$ was performed parasitically during the ANKE beam time in August 2002. The aim of this was to calibrate the integrating modules, the function of which was described in sec. 2.1.4. To calibrate those means to find a correlation between the threshold voltage which is set on a given channel and the cut–off level, measured in the QDC channels. Signals from the counters were supplied to the integrators. Outputs of each layer were summed and redirected to the TDC. Thus, events in which a charge collected in the QDC exceeded the imposed threshold value were marked with a signal from the TDC module. The thresholds were varied in the course of the beam time.

The data were then analysed in the following way: for each counter and threshold setting two spectra were created: one containing a sum of signals from upper and lower PMs $Q_s = Q_u + Q_b$ only for events with the integrator time mark, the other one for all events. Subsequently the two spectra were divided. The result was the trigger efficiency as a function of the sum of Q_s (see fig. 2.12).

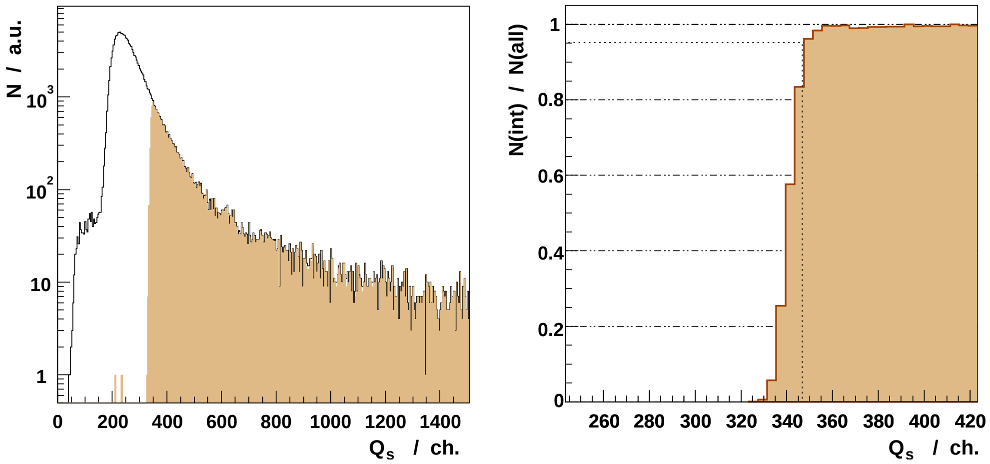

Figure 2.12: The procedure of the calibration of an integrator channel. Left: sum of the two input signals from a QDC for all events (black line) and for events with the integrator time mark (filled spectrum). Right: ratio of the two spectra, reflecting the dependence of the integrator efficiency on the sum of the input signals. Dotted line indicates the determined cut–off level for the current threshold voltage.

As a threshold value the signal corresponding to 0.95 integrator response efficiency was taken.

Fig. 2.13 shows, that the cut–off level depends linearly on the threshold voltage. As expected, the coefficients of the dependence were very similar for all channels with the slope of $\approx$3.1 ch/mV and an insignificant offset. The calibration is independent of the high voltage setting, at which PMs were operated.

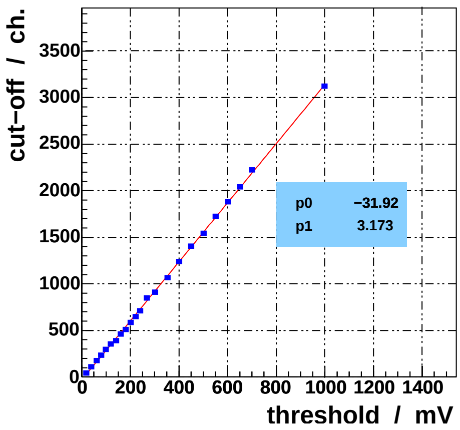

Figure 2.13: Dependence of the cut–off level on the threshold voltage for a channel of an integrator.

2.3 Data taking

The experiment carried out in January 2003 was split into two parts, the first one with a H_2 target, the second one with a D_2 target.

The measurement with a hydrogen target and the beam momentum of 2.345 GeV/c served as a check of an overall performance of the setup as well as to provide calibration data. The tested setup features were:

– adjustment of the hodoscope counters gains,
– performance of the drift chambers,
– drift time calibration,
– momentum reconstruction procedures[3].

Data at three various integrator threshold settings were taken in order to investigate its relation to a suppression factor.

The setup worked properly. The satisfactory suppression of DAQ requests number was achieved with a relatively low discrimination threshold, which was set even below the ^{3}He energy loss – momentum band. Although a hint on the latter was visible, it was impossible to unambiguously identify events with ^{4}He detection without more restrictive software cuts. Data were dominated by a vast amount of events characterised by a momentum of about half a beam momentum and energy losses peaking at the value expected for protons. This group of events was identified as protons originating from the break–up reaction.

In the measurement with a D_2 target data on $\mathrm{dd} \to {}^4\mathrm{He}\,\mathrm{X}$ were taken at three beam

[3]Momentum reconstruction in the forward region of ANKE is very sensitive to the track geometrical parameters, more than e.g. precision with which the chambers positions are known. Therefore it has become a standard, that the latter are adjusted in order to reproduce kinematics of the so–called calibration reactions.

momenta, one below the η production threshold in $\mathrm{dd} \to {}^4\mathrm{He}\eta$ and two above. The luminosity of about $4 \cdot 10^{30}$ $\mathrm{s}^{-1}\mathrm{cm}^{-2}$ was reached. At this luminosity the total particle flux through the detection system was about $7 \cdot 10^5$ s^{-1}. The main trigger rate, with the integrator threshold set below the energy loss – momentum band of ^{3}He, came to 2500 s^{-1}. With approximately 1800 ev/s accepted by DAQ, it results in about 25–30% dead time. The collected data were transferred and written on DLT tapes. In total, 14 tapes (including the H_2 runs) were filled. The runs are listed in appendix A.

p_{beam} / GeV/c	Q / MeV	# of ^{4}He
2.330	-2.0	160 000
2.345	3.2	760 000
2.360	8.3	205 000

Table 2.3: Beam momenta, excess energies and approximate numbers of detected ^{4}He particles in the January'03 beam time.

The nominal beam momenta, corresponding excess energies and approximate numbers of detected ^{4}He particles are collected in table 2.3. The numbers of detected ^{4}He particles were obtained by integration of the momentum spectra.

3 Methods of data analysis

The analysis of experimental data was performed within an analysis framework for ANKE called RootSorter [64]. This is a new analysis tool, based on the ROOT platform [65], entirely written in C++.

In order to achieve the main goal of the experiment and to extract total and differential cross sections for the $\mathrm{dd} \to {}^4\mathrm{He}\eta$ process at each of the excess energies covered, several steps are necessary. The first one is to decode raw experimental information and convert it into physical data. The procedure is described in the first few sections of this chapter. Subsequently, the physical data are used to select events with detection of ${}^4\mathrm{He}$ particles. Here, a set of restrictive, two–dimensional cuts described in sec. 3.3 is needed to identify those events unambiguously. The group of events, where the ${}^4\mathrm{He}$ particle was accompanied by the η meson is then identified via the missing mass technique. Eventually, obtained angular distributions are corrected for effects, which can cause their distortions, i.e. acceptance losses and the impact of the resolution. This is presented in sec. 3.4, together with a method of determination of final centre–of–mass momentum p_{cm}, complementary to the information provided by COSY. As the last step of data analysis, two methods of luminosity determination are described, employing yields for two registered processes.

3.1 Raw event content

The content of the raw experimental information follows from the layout of the detection setup – it is a direct consequence of the used detector types and the electronic modules serving them. The raw information contains the following:

Scintillation counters

Q_u^i, Q_b^i – light output, read out through the upper and lower PM, respectively;
T_u^i, T_b^i, T_m^i – time signals from the upper and lower PM and the mean timer signal;
T_{int}^1, T_{int}^2 – time signals of the integrator response for the first and second layer, respectively;

Drift chambers

Ch^k, Pl^k, Wi^k, Dt^k – chamber, plane and wire numbers together with the registered drift time. For reading out time information the multi–hit TDC modules were used, thus for each event up to 16 entries per wire could be registered;

Scalers

T_i number of triggers of the type i;

T_{out} number of registered events;

COSY – information about the beam current, universal time, presence of a beam (or a time gap between cycles); information on beam energy or polarisation setting in the case of measurements with multiple beam energies or polarisation within one supercycle.

3.2 Calibration procedures

In order to make an efficient use of the collected data, it must be converted to physical quantities, i.e. energy losses in the hodoscope layers, times of flight and a particle momentum vector. This is done with the use of appropriate calibrations, which are the subject of the following sections.

3.2.1 Drift time to position mapping

In order to determine position information from drift chambers, one needs to recalculate a measured drift time to the distance from a sense wire. As mentioned in sec. 2.2.2, for this purpose a method called autocalibration was used. This method is based only on a shape of a drift time spectrum and the assumption that an average particle distribution over a cell is uniform (this assumption is quite well fulfilled thanks to the double–sense–wire construction of MWDCs). The latter point implies that

$$\mathrm{d}N = C \cdot \mathrm{d}x\,,$$

where $\mathrm{d}x$ is an infinitesimal range in distance and $\mathrm{d}N$ is a corresponding number of events. C is a proportionality constant depending on the collected statistics and a cell width. After multiplying the dependence by $\mathrm{d}t/\mathrm{d}t$ and integrating one obtains

$$x(t) - x(t_0) = \frac{1}{C}\int_{t_0}^{t} \frac{\mathrm{d}N}{\mathrm{d}t}\mathrm{d}t\,.$$

If t_0 and t_k stand for times corresponding to hits on the sense wire and end of cell, respectively, then $x(t_0) = 0$ and $x(t_k) = D$ where D denotes the cell width. Those times can be directly extracted from the drift time distribution as the edges of a regular drift time spectrum. From the boundary conditions one determines the constant of the integral

$$C = \frac{1}{D}\int_{t_0}^{t_k} \frac{\mathrm{d}N}{\mathrm{d}t}\mathrm{d}t\,.$$

In a first iteration, for all planes a drift time to position mapping obtained in the test run was used. Based on this, a rough track and momentum reconstruction was done. Tracks, or more precisely track projections on horizontal and vertical planes, were reconstructed with the least square method. For each track projection a response of at least three out of four wire planes was demanded. Momentum reconstruction procedures are described in the next section.

Momentum, together with the energy loss information (calibrated relatively only, not absolutely) enabled a PID–wise particle selection. In this way relatively clean data samples containing events with detection of protons, $^3\mathrm{He}$ and $^4\mathrm{He}$ were separated.

For each particle type and for each plane separately a drift time distribution for clean hits was plotted. A hit was considered clean, when it was unambiguously assigned to a reconstructed track.

Comparison of the drift time spectra for different particle species revealed slight discrepancies between them. Those could originate from differences in the ways the charge is generated when a particle passes a sensitive plane (for $^4\mathrm{He}$ the ionisation effect is stronger and the collected charge reaches faster the discrimination threshold). Another potential source of discrepancies is in a difference in time of flight. The shape of a drift time spectrum changes also with the mean track angle (angle between a track and a sensitive plane) and its range – and those are determined by the physics processes allowed, their cross sections and distributions. For the reasons listed above separate calibrations were performed for different particle types, based on the preselected data samples.

The position resolution achieved was determined from the experimental distribution of sum of squares divided by number of degrees of freedom (ndf). By restricting the sum–of–squares distribution to tracks reconstructed from 4 hits only and neglecting 3–hit tracks (which were, however, also included in the physics analysis) one fixes the number of degrees of freedom to 2. Subsequently one is able to fit the sum–of–squares spectrum with the normalised by ndf χ^2 function for this ndf [5]

$$f(z, ndf = 2) \;=\; \tfrac{1}{2}\exp\left(-\frac{z}{\sigma_x^2}\right) \quad , \quad z = \tfrac{1}{2}\sum_{i=1}^{4}(x_i - \overline{x}_i)^2 \tag{3.1}$$

leaving the resolution σ_x as a free parameter. Symbols x_i and $\overline{x}_i$ denote the measured positions and those of a reconstructed track cross section with the i–th wire plane, respectively. The latter is considered to be an approximation of the real hit position, which remains unknown. When fitting function 3.1 to the experimental resolution one has to insert additional factor to account for the fact that the experimental spectrum is not normalised to unity, as is the function. Fig. 3.1 shows the distribution of sum of squares divided by ndf for 4–hit tracks in the horizontal plane. Clearly, the experimental distribution does not follow the exponential dependence above, which indicates that the position spread may differ from gaussian. One can, however, assume a gaussian position spread and try to fit various ranges of the spectrum above with the formula 3.1. Obtained values of this 'effective' σ_x cover a range between 0.07 mm and 0.2 mm. Even assuming the worst value of 0.2 mm, this position resolution is still several times better than that which was assumed in the simulations with the originally planned setup containing multiwire proportional chambers as a tracking detector.

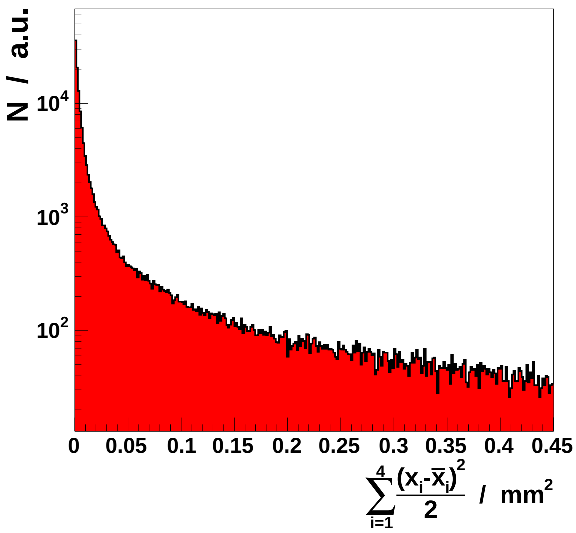

Figure 3.1: The sum–of–squares distribution for horizontal tracks reconstructed out of four hits in MWDCs.

3.2.2 Momentum reconstruction

For reconstruction of a particle momentum vector a procedure described in [66, 67] was applied. As the first step, GEANT simulations of so–called teaching samples were done. They required detailed information on the setup, including target and detectors positions, materials properties and magnetic field maps. The coordinates of each track on the sensitive planes of MWDCs were used to reconstruct the track parameters with the assumption that it can be described by a straight line in the region where the hits were registered. Subsequently, the parameters of that track – tangents of angles in vertical and horizontal planes as well as the coordinates of the track cross section with a well defined, fixed plane[1] – were recorded. Having a sufficiently big sample, for each of the momentum components a second order polynomial expansion in the listed track parameters was fitted (a detailed description is available in [66, 67]). The coefficients of this expansion were later on applied to reconstruct momenta for experimental events. For each of those again, first a straight line was reconstructed and its parameters were converted, with the use of previously found coefficients – to the momentum vector. The precision of this method is comparable with the conventional tracing in magnetic field (which was studied in GEANT

[1] The so–called ANKE coordinate system used for the description of geometry (e.g. detectors positions, track parameters) is defined in a following way: z–axis is along the longer horizontal axis of the D2 dipole and points in the beam direction, y–axis is vertical, oriented upwards, x–axis points out of the COSY ring. It is centred in the centre of D2. As the fixed plane mentioned in the text, traditionally the plane containing the D2 exit window is chosen (z=72 cm).

simulations), with a significantly smaller CPU time consumption.

To account correctly for different charge and energy losses of different particle species, separate teaching samples and coefficient files were created and used for each of the particle types of interest (protons, deuterons, $^3\mathrm{He}$ and $^4\mathrm{He}$).

3.2.3 Energy loss

The energy loss of a particle in material depends on the particle momentum, mass, charge as well as properties of that material. This dependence is known as the Bethe–Bloch formula [5]. The light output was converted on both sides of each of the counters in two photomultipliers and read out via QDC modules. Calibration in this case means finding a function, which maps the measured charge $Q_s = Q_u + Q_b$ (in QDC channels) to energy loss (e.g. in MeV). Additionally, the function should correct for the dependence between the measured charge and the vertical coordinate of a track cross section with a counter y. Former studies showed that the discussed function can be factorised as follows [68]:

$$dE = \frac{Pol2(Q_s)}{Pol2(y)}$$

where $Pol2()$ denotes a second–order polynomial. This means that for each counter a set of 5 parameters had to be found.

Let us consider the correction for the vertical position first. The vertical coordinate of a track cross section with a counter can be determined in two ways: from the extrapolation of the track reconstructed in the MWDCs or from the time difference between signals from the upper and lower PM. The second option was chosen to make the correction independent of other detector response.

For each counter a data sample covering a momentum bin of 50 MeV/c was chosen. Preselected data with one particle type ($^4\mathrm{He}$) were used for this purpose to ensure well defined energy loss. Fig. 3.2, upper left plot, shows the signal dependence on the vertical hit position expressed in terms of a time difference from upper and lower PMs. As an example data for counter no. 5 are shown. The function normalised to unity in its minimum (upper right) is used to correct for this effect independently of a mean value of Q_s. In the lower spectra raw data as well as corrected one are shown. The correction improved the energy loss resolution by ca. 40%.

Subsequently, parameters of a numerator in the above equation were determined. Here, preselected data for various particle types were used: protons, deuterons, $^3\mathrm{He}$ and $^4\mathrm{He}$. For those particle types a counter response was simulated, normalised by a counter thickness and tabulated as a function of momentum. Then, for each counter and particle type, Q_s at several momenta were read out and set against the simulated energy losses. This allowed fitting the parabola coefficients. The result for a typical counter is shown in fig. 3.3. One sees, that the quadratic function very well describes the observed dependence. The fact, that this dependence is not linear is likely to originate from the quenching effect, which was not taken into account in the simulations. This effect is negligible for

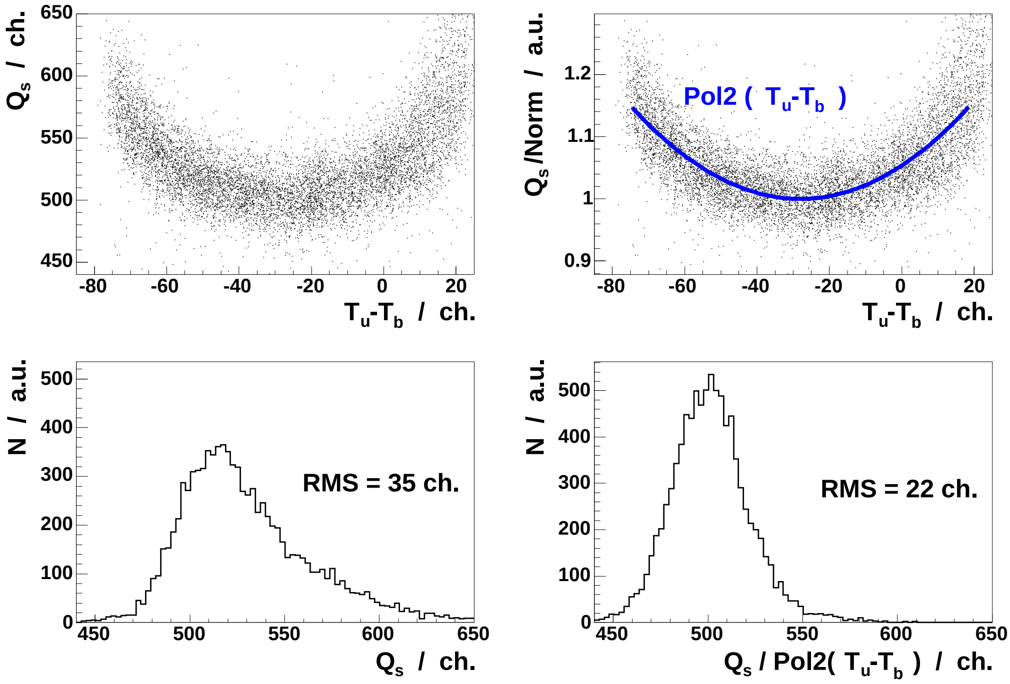

Figure 3.2: Correction of the counter QDC signal for the vertical position dependence of a hit (data for counter 5 as an example). Upper left: collected charge versus time difference of upper and lower PM signal, data restricted to a small momentum bin. Upper right: the same data normalised to unity in the minimum. A trend function, used to correct data later on, is plotted on top of it. Lower figures show data before and after correction (left and right, respectively).

light and fast particles, but plays an important role for the helium particles which lose significant part of their energy when passing the counter material.

3.2.4 Time of flight

Similarly to the energy loss, time of flight was calibrated based on GEANT simulations for the ^{4}He particles. A more simple, analytic approach consisting in calculation of time of flight from the momentum information turned out inappropriate due to very large energy losses, and thus velocity losses, when passing the counter material by particles.

For time signals of counters of the second and third layers of the hodoscope (measured with respect to the trigger time, which in turn was dictated by the timing of the first layer) a linear calibration worked very well. The signals were first divided by the distance between the counters of interest in order to make the response independent of the counter pair. The

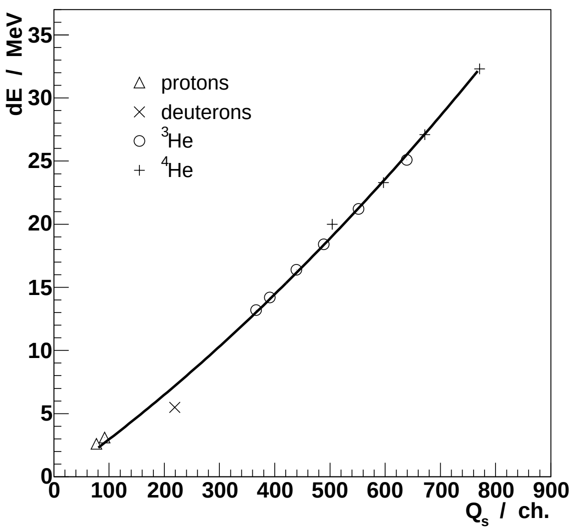

Figure 3.3: Relation between simulated energy loss and the counter response corrected for the vertical position dependence (both are mean values). Different points for the same particle type correspond to different momentum bins. The line represents a fitted quadratic function.

final calibration function used was of the form:

$$TOF(no_1, no_i) = \frac{Pol1(T_i)}{distance(counter_1, counter_i)}$$

where the index 1 refers to counters from the 1st hodoscope layer and the index $i = 2$ or 3 to those from the second or third layer, respectively. Fig. 3.4 shows the outcome of this calibration procedure. T_3 shows a better resolution than T_2. However, one should mention here that the measurement of T_3 was enabled only starting from run 5233, see appendix A. This means that ca. 30% of data collected for the highest beam momentum are devoid of this information. Data for other beam momenta are not affected.

3.3 Identification of ^{4}He particles

A method described here served not only for ^{4}He particles identification, but also for selection of events with ^{3}He detection (with appropriately adjusted cut parameters). Particle identification in this experiment was done by means of the energy loss, momentum and time of flight information.

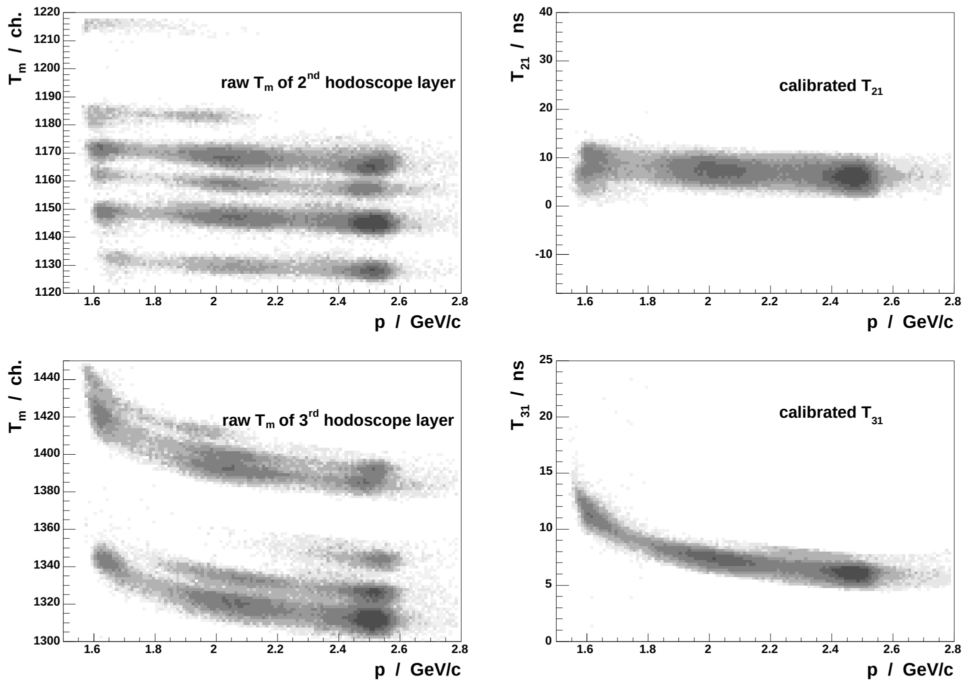

Figure 3.4: Raw (left) and calibrated (right) time of flight information obtained from the hodoscope plotted against reconstructed momentum for preselected ^{4}He particles. Upper row shows data for the second hodoscope layer located ca. 5 cm behind the first layer. Lower plots contain data for the third layer, placed about 30 cm behind the first layer.

3.3.1 Energy loss – momentum cuts

For each hodoscope layer the information on energy loss was plotted against momentum, see fig. 3.5 where data collected at a beam momentum of 2.345 GeV/c are shown as an illustration. A distinct correlation for different particle types – here ^{3}He and ^{4}He – can be observed. However, a significant background contribution centred at the momentum of about 2.35 GeV/c is also visible, in spite of a relatively high energy loss threshold imposed. This, as mentioned in sec. 2.3, was identified as a tail of protons originating mainly from break–up reactions. In this plot, for charge=1 particles, the momentum is doubled.

Based on preselected data for ^{3}He and ^{4}He, the mean value of energy loss and its standard deviation have been found as functions of momentum for those particles. For this purpose, the two–dimensional dE–p spectra were divided into slices in momentum and for each slice the energy loss distribution was fitted with a gaussian function. The mean values determined a line of trend (lying on the simulated energy loss – momentum line, which is a consequence of the calibration method exploited). The standard deviation was used

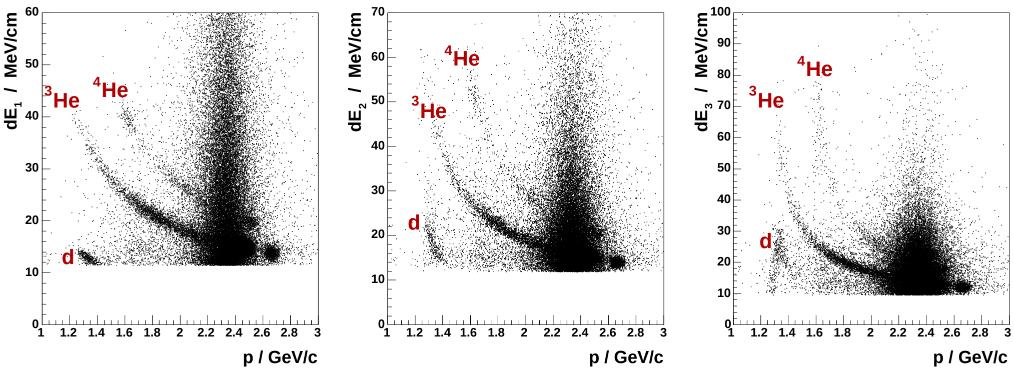

Figure 3.5: Energy loss per counter thickness unit versus momentum for each of the hodoscope layers. Bands formed by ^{3}He and ^{4}He events are partially obscured by a group of events centred at the momentum of 2.35 GeV/c identified as break–up protons.

for determination of a width of a cut, which should be applied in the final event selection. Typically, at least three standard deviations were taken and in case of unambiguities (in the region of the proton background, where fitting failed), cut width was interpolated between background–free points (smaller and higher momenta). Fig. 3.6 shows the determined cut shapes.

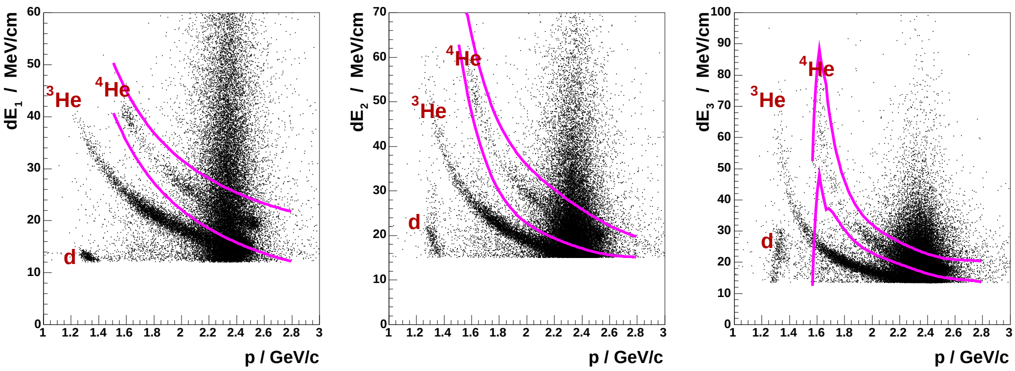

Figure 3.6: Cut shapes for ^{4}He based on the energy loss information in the three layers of the forward hodoscope and reconstructed momentum. For ^{3}He particles not only cut shapes, but also their widths were determined separately to account for different energy loss straggling.

Application of such a threefold condition resulted in the momentum spectrum for the ^{4}He particles, which is shown in the fig. 3.7.

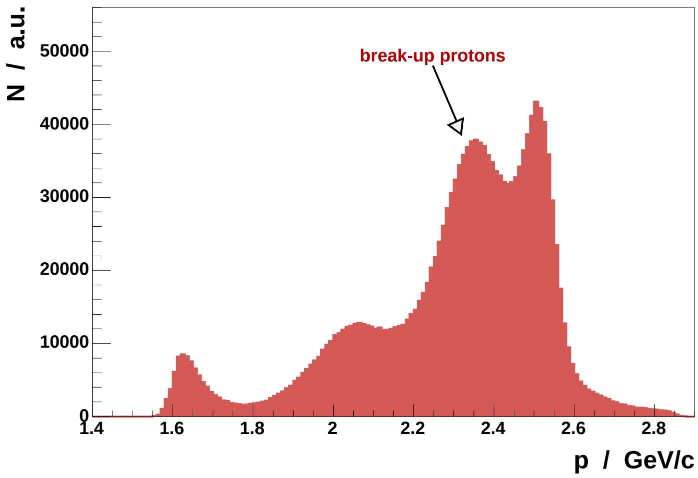

Figure 3.7: Momentum spectrum of the ^{4}He particles detected at a beam momentum of 2.345 GeV/c, obtained with the threefold energy loss – momentum cut. Apart from an expected three–peak structure, a contribution centering around 2.35 GeV/c is seen, identified as protons from break–up of beam deuterons.

The distribution reveals not the expected three–peak structure, as those described in [19, 25, 62], but a four–peak one, the fourth peak being a remnant of the break–up protons. In fact, as the events are characterised by very large energy losses as for protons, a following scenario is plausible: the break–up protons hit the scintillation counters and undergo hadronic reactions with the counter material. The outgoing particles are not only protons but also heavier particles. The energy deposited by them in the counters, though correlated with the original protons momentum, are much larger and do not belong to the 'proton band'.

3.3.2 Time of flight – momentum cut

In order to eliminate background of the break–up protons events, the energy loss – momentum cuts are insufficient. Another criterion which can be used here is time of flight. Time information of signals from the second and the third layer of the scintillation hodoscope was calibrated in a way presented in sec. 3.2.4. This information, like energy losses, was used in combination with momentum. The lines of trend in the time of flight – momentum spectra as well as the cuts widths were determined in a way analogous to the one applied for energy losses. Events passing the threefold dE–p criterion, i.e. those forming the momentum spectrum depicted in fig. 3.7, are characterised by the times of flight shown in fig. 3.8 as a function of the reconstructed momentum.

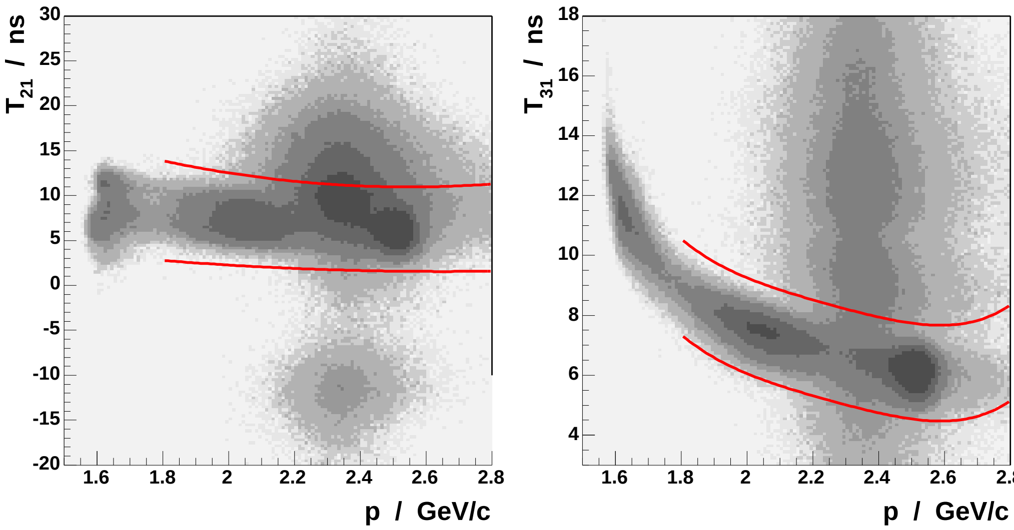

Figure 3.8: Times of flight versus momentum for the second (left) and for the third (right) hodoscope layer for events selected with the threefold dE–p cut. The unwanted break–up contribution can be well eliminated by imposing cuts represented by the solid lines.

The left scatter plot represents the information from the second layer, while the right one from the third layer. A striking point to notice is that apart from the relatively clean ^{4}He bands there are also contributions centred at a momentum of 2.35 GeV/c. These events are quite well separated from the ^{4}He ones. Thus, the time of flight – momentum spectra are well suited to dispose of the unwanted proton contribution by imposing appropriate cuts. The final cuts used are marked in the figures by the solid lines. For momenta lower than 1.8 GeV/c all events are accepted.

All applied cuts ensured a sufficiently clean selection of events with ^{4}He detection. In particular in the momentum region where ^{4}He particles produced together with the η mesons are located (centred around 2.05 GeV/c) the background contribution is negligible.

Fig. 3.9 shows subsequent steps of the ^{4}He discrimination. The spectrum with the most rich population (red) represents the minimum bias trigger T2. This spectrum is scaled by 9990 to remove the hardware prescaling factor introduced in the experiment to reduce deadtime. The blue line corresponds to all events registered with the energy loss trigger T1. The grey and brown spectra are created from the events which survive the threefold dE–p cut (grey) as well as the twofold T–p cut (brown). Altogether, the applied hardware– and software restrictions resulted in the suppression factor of about 10^5. The final momentum spectrum shows indeed the expected triple–peak structure.

As for the selection of ^{3}He, it was done in a very similar way, therefore it is not

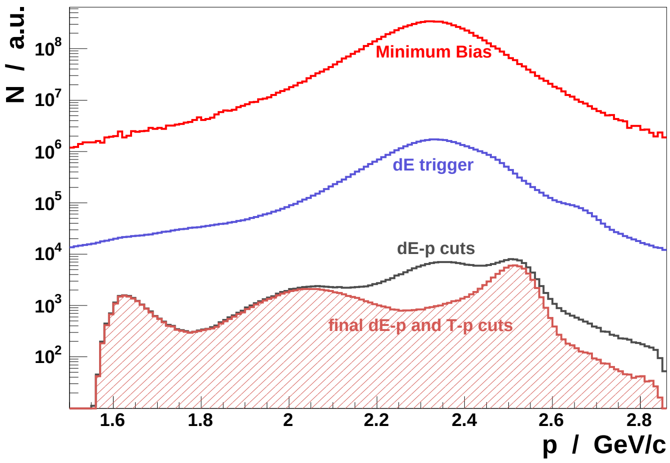

Figure 3.9: Subsequent levels of ^{4}He discrimination. Red and blue lines represent events collected with the minimum bias and energy loss triggers, respectively. Depicted in grey are events which pass the dE–p cuts and in brown those, which additionally fulfil the T–p conditions. The overall suppression factor is about 10^5.

discussed here in detail. The main interest was in the events stemming from the reaction $\mathrm{dd} \to {}^3\mathrm{He}\,\mathrm{n}$, which were used in one of the two ways of luminosity determination. The momenta in the registered events of this reaction peak at about 2.66 GeV/c (forward angles of outgoing ^{3}He), i.e. relatively far from the centre of the background proton peak.

3.4 Analysis of the dd→^{4}Heη reaction

Having accomplished a clean ^{4}He selection, the subsequent challenge is to identify signatures of the $\mathrm{dd} \to {}^4\mathrm{He}\eta$ reaction. They can be observed in various spectra, e.g. momentum components distributions.

3.4.1 Adjustment of momentum reconstruction procedure

It is very instructive to look at the distributions of individual centre–of–mass momentum components p_x, p_y and p_z. As already mentioned, for the data collected at the nominal beam momentum of 2.345 GeV/c the acceptance of the detection system for $\mathrm{dd} \to {}^4\mathrm{He}\eta$ is close to 100%. Therefore it is clear that the enhancements in the mentioned distributions for this beam momentum, when set against the corresponding spectra for $p_{beam} = 2.330$ GeV/c should show a mean value of zero. Of course the subthreshold data must be scaled with phase space to the same energy[2] as well as normalised to the same luminosity. For the latter point, a corresponding factor was found by comparing the above– and below threshold histograms outside of the region containing events from the η production. The excess events would be concentrated around zero if all the setup parameters: its geometry, deuteron beam position and angle, magnetic field maps and its central values, *etc.* were known with an infinite precision. In reality all the items from this list are measured with a certain error. Let us consider positions and angle of the multiwire drift chambers as an example. The absolute positions[3] are measured with an accuracy of about 2 mm. This implies the accuracy of the chambers angle of several mrad. Such an error of the drift chambers geometry propagates to the reconstructed momentum and may cause a shift of each of the components even by several tens of MeV/c. Most sensitive is the p_z component.

Distributions of the centre–of–mass momentum components are depicted in fig. 3.10. Spectra in the left column represent data taken at the nominal beam momentum of 2.345 GeV/c (red solid line) and 2.330 GeV/c (scaled kinematically to the first beam momentum, dotted line). Results of the subtraction for each momentum component (corresponding to the events with η production) are drawn in the right column.

Although the precision with which the mean values of p_x, p_y and p_z can be determined from these spectra is not better than 5 MeV/c, it is clear that they differ from zero. This fact must be corrected for before proceeding to further, physical analysis of data.

Two ways have been developed in order to correct the shift of the centre of the ^{4}He momentum sphere associated with the η production. One way was to adjust the MWDCs positions and angle, i.e. to find an effective geometry. Results obtained with this method will be marked with a subscript *geomod*. The other way made use of the fact that the momentum reconstruction procedure uses positions and angles of the track cross section with the D2 exit window. By imposing a well chosen set of offsets on those track parameters one is able to relocate the momentum sphere to be centred at zero. As it uses the original geometry, outcome of this method will be provided with the subscript *nominal*. Starting from here, where it is not mentioned, the *nominal* results are taken as default for illustration. In each case, however, it has been checked that the conclusion from the corresponding *geomod* spectra would be the same. Consistency of the two results is a condition for the consistency of the whole analysis. Here, the influence of other quantities listed above on the momentum reconstructed is neglected. This is justified, because the MWDCs positions and angle have the strongest impact. Other quantities are unlikely to change the momentum reconstruction outcome as it is observed. To achieve this, their values would need to be changed by much more than the precision with which they are

[2]Scaling with phase space (called also 'kinematic scaling') was done in a following way: for events collected at the original excess energy Q_0, first the momentum vector was boosted back to the centre–of–mass system with the boost vector corresponding to Q_0. Subsequently the momentum vector was multiplied by the ratio of maximal centre–of–mass momenta possible in two–pion production $F = p(Q_1)/p(Q_0)$ and eventually boosted back to the laboratory system with a boost vector of Q_1. The event was assigned a weight equal to F.

[3]Hereinafter the absolute positions mean the coordinates in the ANKE coordinate system.

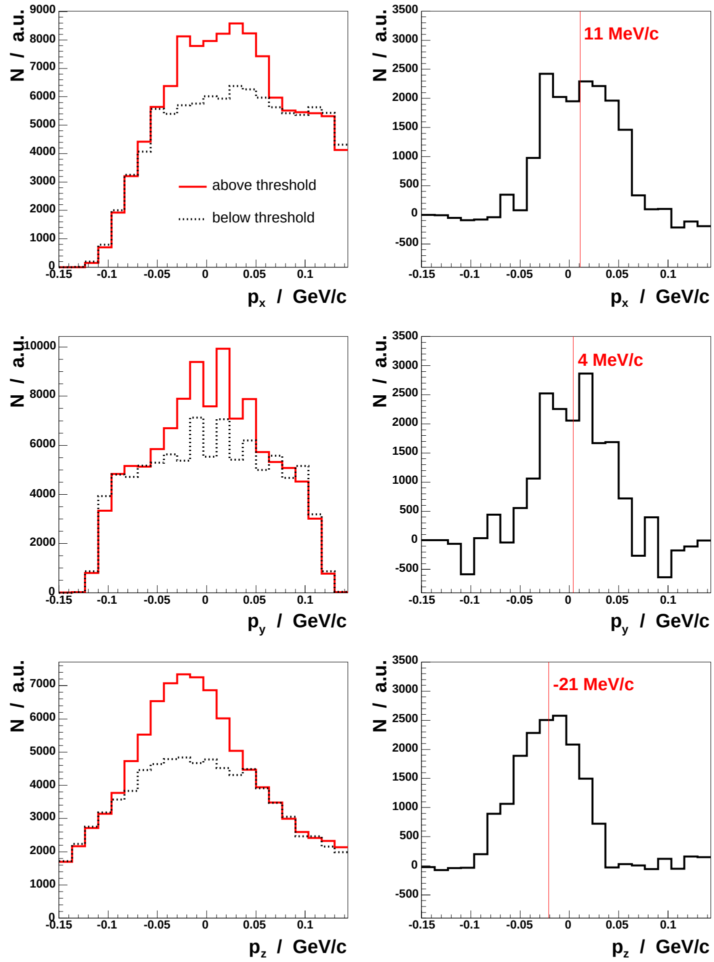

Figure 3.10: Distributions of components of the centre–of–mass momentum vector. Left: data collected at $p_{beam} = 2.345$ GeV/c and $p_{beam} = 2.330$ GeV/c scaled to the same beam momentum and luminosity. Right: result of the subtraction. Instead of zero, spectra in the right indicate mean value of $\vec{p} = (11, 4, -21)$ MeV/c.

known. Changes of the target position, beam angle and central values of magnetic field could cause a change of a few MeV/c rather than a few tens MeV/c.

3.4.2 Determination of centre–of–mass η momentum

Simulations showed, that the analysis of the transverse momentum spectrum can provide information on p_{cm} of the outgoing particles, and thus the excess energy (see sec. 2.2.1).

Experimental distributions of the ^{4}He transverse momentum p_t are shown in fig. 3.11. Only events fulfilling the condition of missing mass greater than 0.54 GeV/c^2 are taken into consideration here.

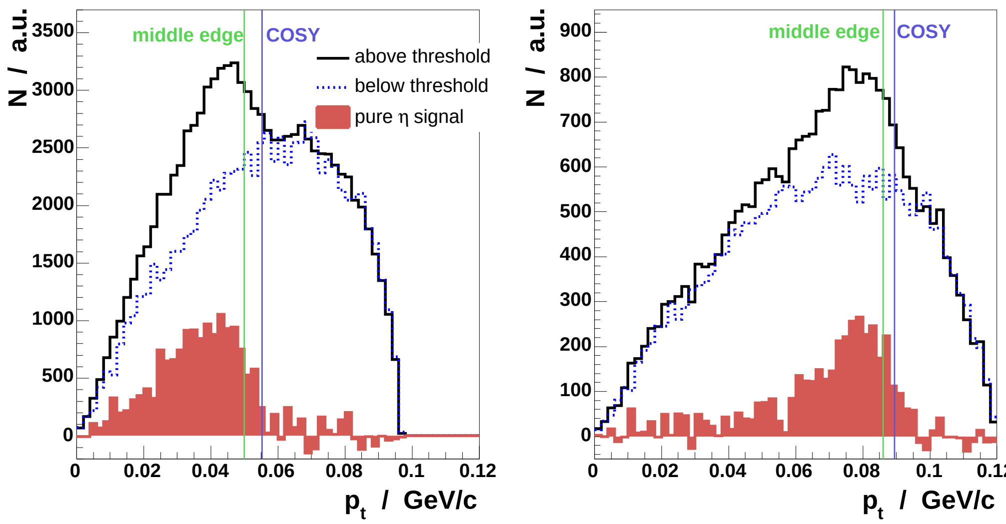

Figure 3.11: Distributions of transverse momentum obtained for nominal beam momenta 2.345 GeV/c (left, solid line) and 2.360 GeV/c (right, solid line) for events with m_X >0.54 GeV/c^2. On top of them the kinematically scaled distribution obtained at p_{beam} =2.330 GeV/c is drawn in dotted line. The difference, corresponding to events with η production is represented by filled histograms. Vertical lines indicate p_{cm} calculated from the nominal beam momenta (blue) and deduced from the presented spectra (green).

In the left figure the solid line represents data obtained at a beam momentum of 2.345 GeV/c, while in the right one for 2.360 GeV/c. Dotted lines indicate background scaled to the given beam momenta from the measurement below threshold. Filled histograms result from a subtraction of those two, and thus correspond to pure η production events. It has been found in the simulations that the final p_{cm} can be found as the middle of the steeper edge of the latter distributions. In fact the original p_t distribution has a sharp cut–off at p_{cm}, which is, however, smeared in the experiment due to the resolution effects. In fig. 3.11 for the nominal p_{beam} = 2.345 GeV/c the middle of the edge of the p_t distribution points at a p_{cm} of 50 MeV/c rather than 55 MeV/c as calculated from the nominal beam momentum. This difference indicates, that the real beam momentum in the experiment was by about 2 MeV/c lower than the nominal value. This difference is well within the precision of COSY. The relative beam momenta, however, are known with a 10 times better precision (for small changes). The discussed beam momentum of 2.345 GeV/c was developed by the COSY operators as first, the other two being developed relatively to that one. The differences are small (only 15 MeV/c) so that it is sensible to assume that the other two beam momenta exploited in the experiment were lower than their nominal values by 2 MeV/c as well. The spectra on the right of fig. 3.11 do not contradict this hypothesis.

A direct measurement of the beam momentum was conducted during the experiment. The frequency spectrum of the circulating beam was recorded in the beginning and at the end of a cycle. For this purpose the HP 3589 A FFT frequency analyser was used. The frequency shift between the two measurements can be recalculated to the momentum shift due to the energy losses in the target [69]. This measurement yields also information on the beam momentum spread in the beginning of a cycle and at the end. It was found, that the starting spread was

$$\frac{\delta p_{beam}}{p_{beam}}(t=0) = 2.6 \cdot 10^{-4},$$

while after 15 minutes of circulation

$$\frac{\delta p_{beam}}{p_{beam}}(t=15\,\mathrm{min}) = 7.5 \cdot 10^{-4}.$$

The shift of the central value of beam momentum amounted to

$$\frac{\Delta p_{beam}}{p_{beam}} = p_{beam}(t=15\,\mathrm{min}) - p_{beam}(t=0) = 2.5 \text{ MeV/c}.$$

Thus, the results of the experiment are in fact averaged over such a beam momentum interval. The mean value of beam momentum measured in this method is even closer to the result obtained from the analysis of the transverse momentum spectrum. As all results are of similar precision, the one favoured by the data analysis has been chosen for further calculations and presentation of the results. Excess energy has been calculated according to the formula which relates it with the final centre–of–mass momentum

$$Q = p_{cm}^2 \Big/ \frac{2m_\alpha m_\eta}{m_\alpha + m_\eta}. \tag{3.2}$$

The results of this section are collected in table 3.1.

p_b / GeV/c nominal	**p_b / GeV/c from exp. p_t**	p_b / GeV/c from FA	p_{cm} / MeV/c nominal	**p_{cm} / MeV/c from exp. p_t**	Q / MeV nominal	**Q / MeV from exp. p_t**
2.330	**2.328**	–	–	–	-2.0	**-2.6**
2.345	**2.343**	2.344	55	**50**	3.2	**2.6**
2.360	**2.358**	–	89	**86**	8.3	**7.7**

Table 3.1: Nominal and deduced from data values of beam momenta, centre–of–mass final momenta and excess energies. For a full description see text. For further analysis highlighted values were used.

The uncertainty in determination of beam momentum and final centre–of–mass momentum must be reflected in properly assigned errors of p_{cm} and Q. From fig. 3.11 p_{cm} can be determined with an accuracy of about 5 MeV/c so the following errors have been assigned to the lower energy point:

$$\begin{aligned}\Delta p_{cm,1} &= 5\ \mathrm{MeV/c}\,,\\ \Delta Q_1 &= \frac{\mathrm{d}Q}{\mathrm{d}p_{cm}}\cdot\Delta p_{cm,1}\ =\ 0.6\ \mathrm{MeV}\,.\end{aligned}$$

For the point at the higher energy, the error in p_{cm} determination from p_t was propagated from the lower energy and is equal to 4 MeV/c

$$\Delta p_{cm,2} = 4\ \mathrm{MeV/c}\,,$$

which implies

$$\Delta Q_2 = \frac{\mathrm{d}Q}{\mathrm{d}p_{cm}}\cdot\Delta p_{cm,2}\ =\ 0.8\ \mathrm{MeV}\,.$$

3.4.3 Signatures of dd$\rightarrow$^{4}Heη

Apart from the transverse momentum spectrum (fig. 3.11), in which the contribution of the events with η production is very well visible on top of background, footprints of the investigated reaction can be seen also in other spectra. An important check is the missing mass spectrum, where a peak centred in the mass of the η meson is expected. Indeed, for both beam energies above threshold missing mass spectra reveal such a structure, see fig. 3.12. Again, on top of the spectra obtained for the two energies above threshold, the below–threshold data are plotted to indicate the shape of background. Differences between above– and below–threshold data are plotted as filled histograms. They correspond to pure η production events. Histograms plotted here are not acceptance corrected. In line with the expectations the missing mass resolution for the higher energy is worse than for the lower one, which is a kinematic effect.

Fig. 3.10 shows one–dimensional projections of the sphere formed in the momentum space by ^{4}He stemming from the $\mathrm{dd} \rightarrow {}^4\mathrm{He}\eta$ process. A cross section of this sphere for the lower beam momentum is depicted in the fig. 3.13. It is a scatter plot of one transverse momentum component versus the other one, with longitudinal centre–of–mass momentum restricted near zero and the condition on missing mass to be greater than 540 MeV/c^2. Thus, the expected structure in such a spectrum is a 'slice' of a sphere, i.e. a ring. Indeed, such a structure is identifiable in the presented figure.

3.4.4 Acceptance and resolution correction

Two features of the detection setup, which must be corrected for before drawing physics conclusions from the data, are its momentum resolution and acceptance limitation. These were simulated after the experiment. The previously used simulation program (see

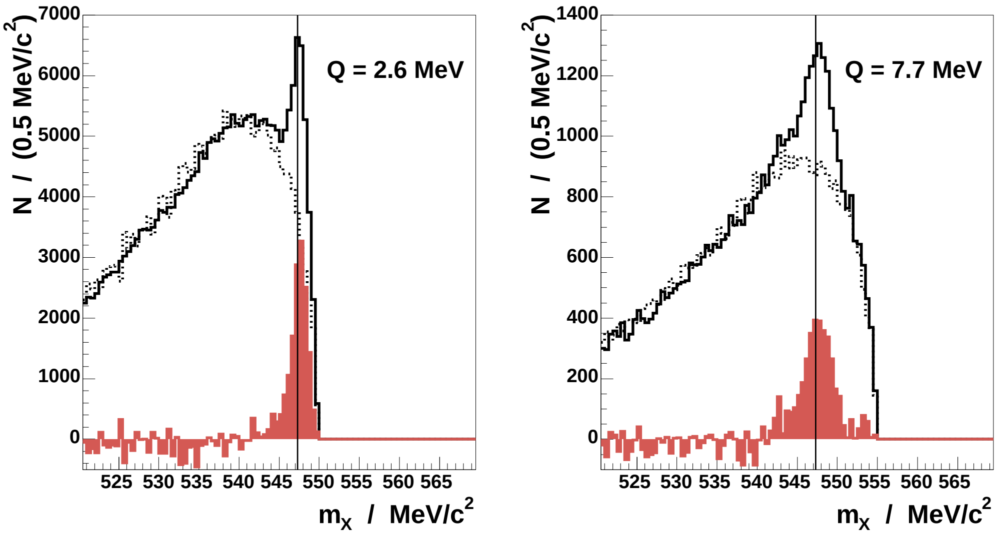

Figure 3.12: Raw missing mass spectra for lower (left) and higher (right) energy. Background extrapolated from the subthreshold measurement is plotted in dotted line. Pure η signals are represented by filled histograms.

sec. 2.2.1) was adopted to the actual experimental setup (use of drift chambers instead of proportional chambers, addition of the third hodoscope layer, *etc.*).

Although a finite momentum resolution does not cause loss of events directly, it is though responsible for the fact, that events migrate from the histogram bins they should belong to according to their original kinematics to the neighbouring ones. This effect can be consistently treated together with acceptance corrections assuming a good knowledge of the original distributions. This is the case for the inclusive ^{4}He production in dd collisions. Also for the other exploited process, dd $\rightarrow$ ^{3}Hen, differential distributions are known for beam momenta close to the investigated ones.

Momentum resolution is affected by a number of physics processes as well as by construction of the detection setup. In the first group the most important process is the small angle scattering of outgoing particles in the materials they pass. The largest contribution here comes from the D2 exit window, which is a 0.5 mm thick aluminium plate. Apart from the small angle scattering, processes leading to energy loss also change momenta of ejectiles. Both mentioned processes are enhanced for ^{4}He particles in comparison to e.g. protons due to a double charge and a large mass of those particles. Thus, it is absolutely necessary to take them into account in the simulation program.

As momentum is determined from the position information on the chambers, their position resolution is another important factor. The way it was estimated is described in sec. 3.2.1. In order to investigate how the position resolution affects the momentum resolution, a gaussian position spread was assumed and simulations were performed assuming two different values of standard deviation for that spread. The values of 0.07 mm and

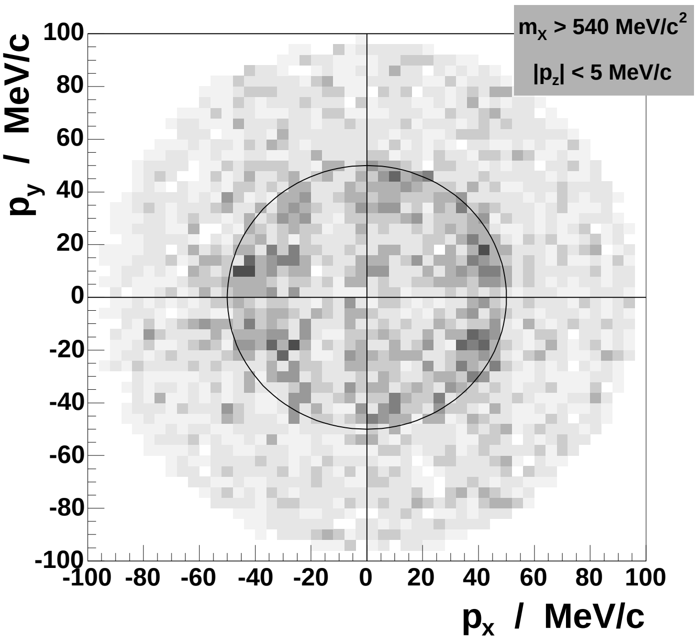

Figure 3.13: Cross section through the momentum space with a plane perpendicular to the p_z axis. A ring formed by the events with η meson production is clearly visible. A line indicating kinematic relation between p_y and p_x at $p_z = 0$ is drawn to guide the eye.

0.2 mm were taken as the extremes. It was found, that between those two simulations there is no noticeable difference. The impact of the small angle scattering is so big that it obscures the contribution from the MWDC position resolution, at least for such a good position resolution. To see the effect of the latter, its values worse than 1 mm would be needed.

The extended (not point–like) target also contributes slightly to the momentum resolution. Horizontal dimensions of the vertex region are determined by dimensions of both the cluster beam and the COSY beam. A diameter of the used cluster beam collimator was chosen to obtain the target diameter of 5 mm in the beam–target interaction region in x and z–directions [70]. The COSY beam dimensions are known to be close to that value, therefore it was used in the simulations. In the y direction the reaction points are also determined by the COSY beam size. This information, however, can be extracted from the distribution of the reconstructed y–position of the reaction point after unfolding the experimental resolution. Such an analysis resulted in the y–target extension of ca. 6.4 mm.

The acceptance is limited due to the finite size of the exit window and MWDCs. There are also certain losses caused by spaces between individual counters in the hodoscope planes as well as dead areas in the wire planes between the double sense wires. These factors have been included in the simulations. The C++ class serving cuts in the analysis of experimental data was used also in the simulations to ensure identical criteria for the event selection.

The acceptance was expressed in terms of the missing mass and the cosine of the cm polar angle $A(m_X, \cos\theta_{cm})$. Two interfaces were provided: a correction on the event basis and a correction of a given spectrum. The latter ensured that statistical errors of the simulated acceptance are correctly incorporated into the errors of the final, acceptance corrected spectra.

As discussed above, due to the migration effects, a starting distribution plays an important role for the determination of the acceptance. Thus, an event generator based on the existing experimental $\mathrm{dd} \to {}^4\mathrm{He}\,\mathrm{X}$ data was used to generate a sample of $5{\cdot}10^6$ events. Additionally, to ensure a good statistics also in the cells that are poorly populated in that event generator that sample was supplemented with a sample of 10^5 events uniformly distributed in the $(m_X, \cos\theta_{cm})$ basis. For the total event distribution it makes only a small correction, but significantly helps in reduction of the final statistical uncertainty.

For the energies above the η production threshold separate samples of η production events were generated. These were used to correct the angular distributions only. As a starting point, an isotropic distribution was used.

The generated event samples were used as inputs for the GEANT simulations. For the events in the acceptance a response of all detectors was recorded, for those out of the ANKE acceptance only the original momentum vector. In the analysis of the simulations results for accepted events the momentum vector was reconstructed from the MWDCs response and the events were confronted with the software cuts. Each event was then supplied with a software trigger flag containing that information: equal to 1 for events in the acceptance and within the cuts, 0 for the rest.

Fig. 3.14 presents the course of the acceptance simulations and its results for the lower energy above the η production threshold as an illustration. The upper part of the figure shows spectra for the background and in the lower two panels spectra for the reaction of interest. Entitled 'all events' are the starting distributions, input of the simulation. The 'accepted events' spectra represent those for which the software trigger flag was set to 1. Spectra provided with a title 'acceptance' result from a division of 'accepted events' by 'all events'. Worth noting is the fact, that as the first one is expressed in terms of the reconstructed missing mass and angle and the second one in terms of the original GEANT values, acceptance calculated in this way contains information on the migration effect described above. Thus, the use of such acceptance correction automatically corrects for that effect, too.

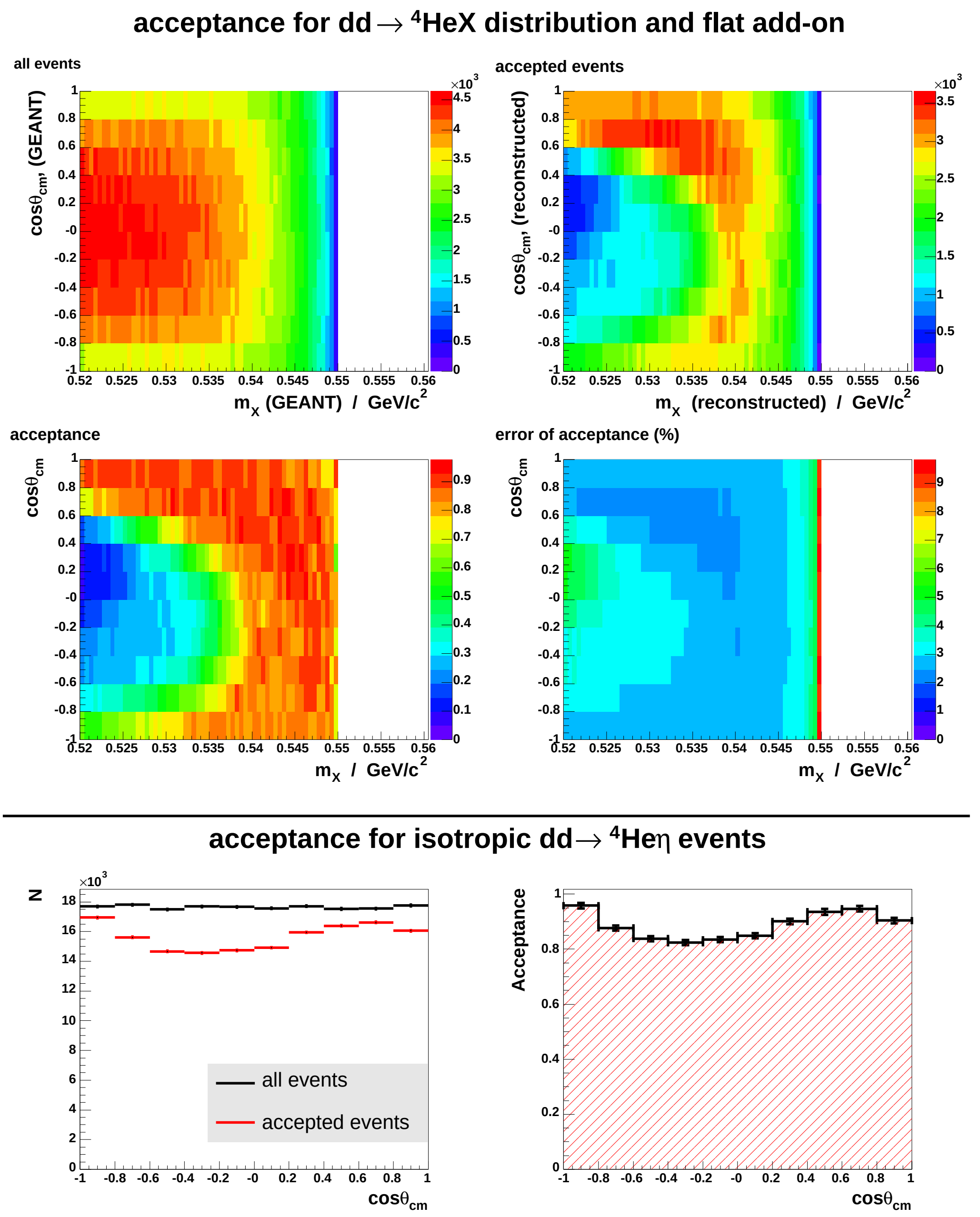

Figure 3.14: The method of acceptance calculation. The two–dimensional figures show simulation results of the dd $\rightarrow$ ^{4}He X event sample, while in the lower panels the dd $\rightarrow$ ^{4}Heη simulations are displayed. For a more detailed description see text.

3.4.5 Extraction of angular distributions

The crucial point for extraction of angular distribution for $\mathrm{dd} \to {}^4\mathrm{He}\eta$ from the collected data is that the events with η production are indistinguishable from the two pion production background on the event basis. The reaction signal can only be identified as a peak in e.g. the missing mass spectrum. After disentanglement of signal from background, the number of events for the signal can be determined. Therefore, to find angular distributions for this process a missing mass spectrum for each angular bin must be considered separately. In order to determine the background shape, the data collected below the η production threshold were used. As that background is considered mainly to be due to the two pion production, so far above its threshold it is not expected to vary much over a beam momentum range of 30 MeV/c. Those data were scaled kinematically to the investigated energy and also plotted for the same angular bins.

For the lower energy above threshold the collected statistics allowed a division into ten angular bins of equal width in $\cos\theta_{cm}$. For the higher energy, where the statistics is several times worse as is the missing mass resolution, data were divided into five bins. The presence of the identical particles in the entrance channel leads to a conclusion, that the angular distribution for the $\mathrm{dd} \to {}^4\mathrm{He}\eta$ process must be symmetric around $90°$. This feature is not exploited here to double the bin content by simultaneous restriction of the $\cos\theta_{cm}$ range to $\langle 0, 1\rangle$. Instead, it was considered as an additional test of the analysis.

In fig. 3.15 the missing mass spectra with the cuts on the cm polar angle are displayed for lower energy above threshold (Q_1 – the first two rows), background extrapolated to that energy (the third and the fourth row), higher energy above threshold (Q_2 – the fifth row) and the corresponding background (the sixth row). Those spectra are acceptance corrected using the correction obtained in the simulation of $\mathrm{dd} \to {}^4\mathrm{He}\,\mathrm{X}$.

The excess of events in the region of the η mass in the spectra above threshold when compared to those below threshold is well visible. It is sharper and more pronounced for angles close to $90°$. This results from a several times better resolution for the transverse momentum components than for the longitudinal one.

In fig. 3.15 the spectra for signal and background are not normalised to the same luminosity. Matching background amplitudes was done by studying the histogram ratio in the region outside of the η peak. For each angular bin the ratio of integrals of missing mass spectra above and below threshold was calculated for the m_X range from 530 MeV/c^2 to 538 MeV/c^2. The graphs shown in fig. 3.16 convey obtained results, including their statistical errors. Their mean values were used as scaling factors F_i for the background spectra and their standard deviations as the errors of those factors. The two ways of adjusting momentum reconstruction yield slightly different results. This fact will be taken into account when calculating systematic errors of the total cross section.

From the acceptance corrected missing mass spectra obtained above the η production threshold those from below threshold were subtracted, after previous scaling of those spectra by the factors F_i. The resulting spectra represent pure η signal, however, corrected for acceptance and resolution with the correction obtained for the background. To amend

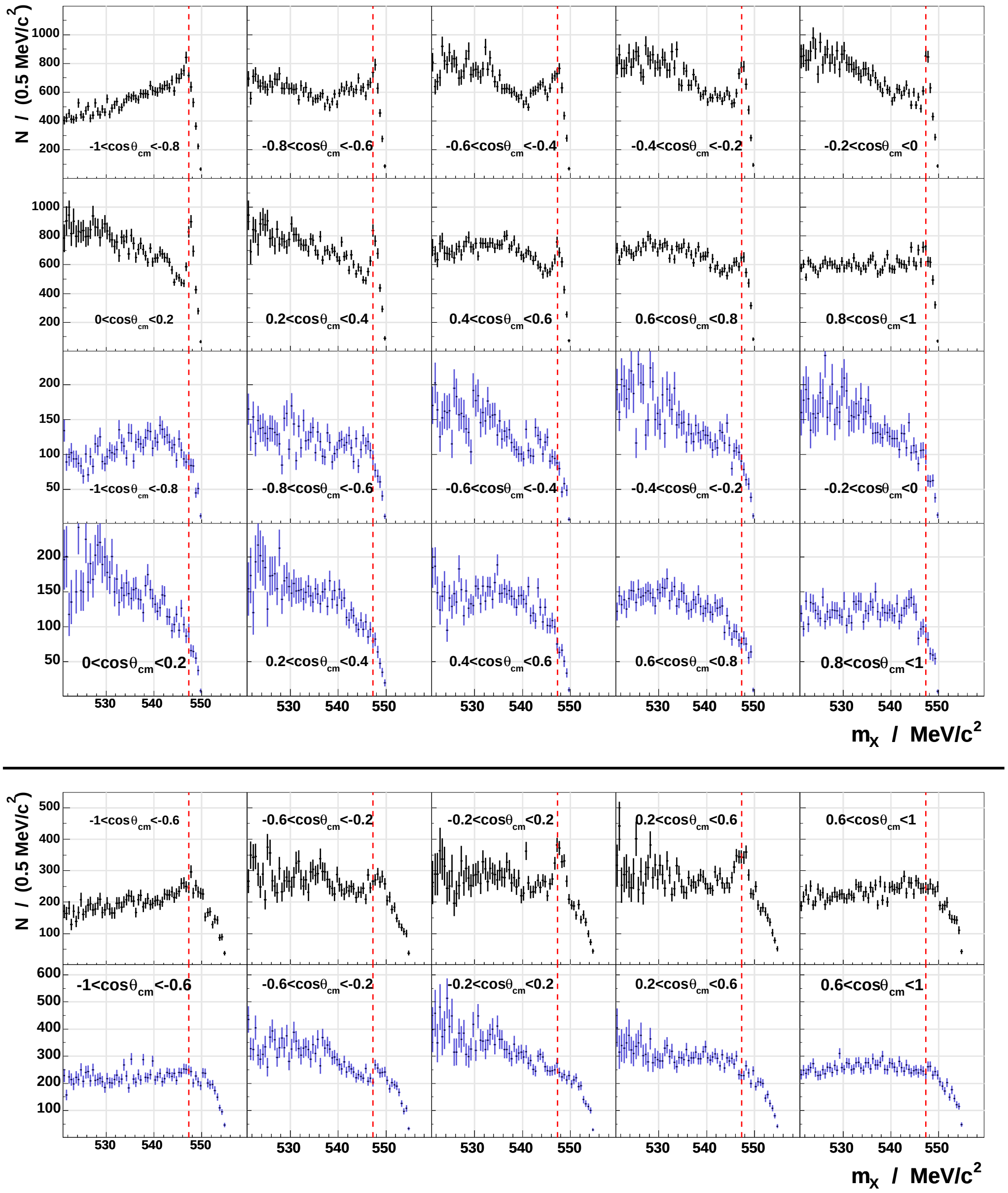

Figure 3.15: Missing mass spectra for individual bins in polar cm angle θ_{cm}. The collection above the line displays data for the lower energy above the η production threshold and the measurement below threshold scaled to that energy for background study (in blue). Data for the higher energy together with the corresponding background are presented below the line. The red dashed line is drawn in the position of the η mass.

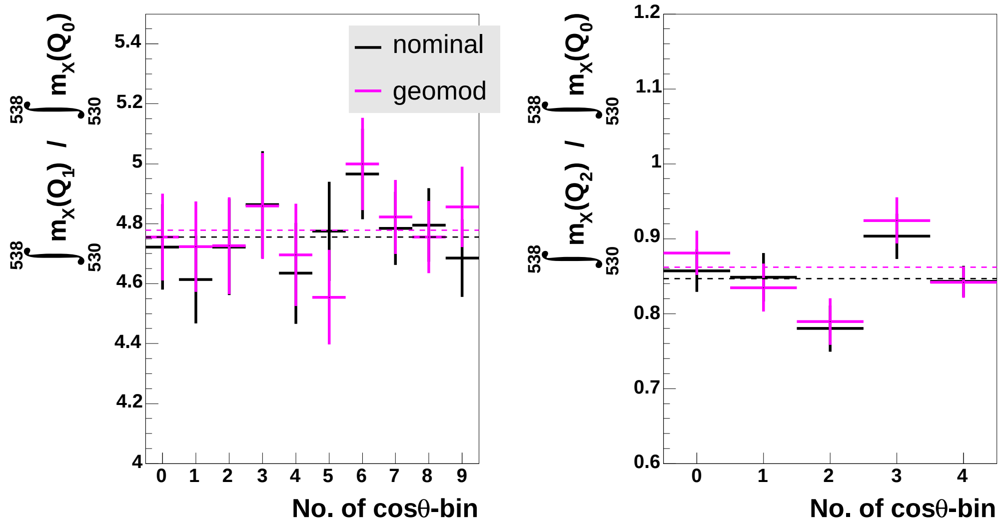

Figure 3.16: Ratio of the missing mass spectrum integrals out of the η peak above and below threshold in angular bins. Mean values (represented by dashed lines) were used to scale the background spectra before subtracting them from the ones obtained above the η production threshold. The standard deviations are considered to be uncertainties of those factors.

it, this acceptance correction was unfolded from the signal spectra. Subsequently, the spectrum for each angular bin was integrated – an unnormalised angular distribution was obtained. This distribution was then corrected with the acceptance obtained in simulation of $\mathrm{dd} \rightarrow {}^4\mathrm{He}\eta$ events. By this operation, the acceptance was corrected in the right way for both: background (when calculating scaling factors and subtracting background from signal its shape was crucial) and signal (essential in determination of angular distribution). Fig. 3.17 shows the outcome of the described procedure for the *nominal* case. The errors displayed in the angular distributions presented in fig. 3.17 are purely statistical. In order to determine impact of various factors on the shape of angular distributions, the above described procedure (including simulation of acceptance corrections) was repeated with different conditions, listed below.

Tuning of momentum reconstruction was done in two ways described in section 3.4.1, called *nominal* and *geomod*.

MWDCs efficiency amounted to over 95% therefore no separate efficiency maps were used to correct the spectra. In order to determine such maps with sufficiently fine grid size, comparable to MWDC position resolution, a much larger event sample would be needed. Otherwise, the statistical errors of the calculated efficiency correction would be much larger than the significance of the correction itself. Therefore a different method was used to investigate the impact of efficiency on the angular distributions.

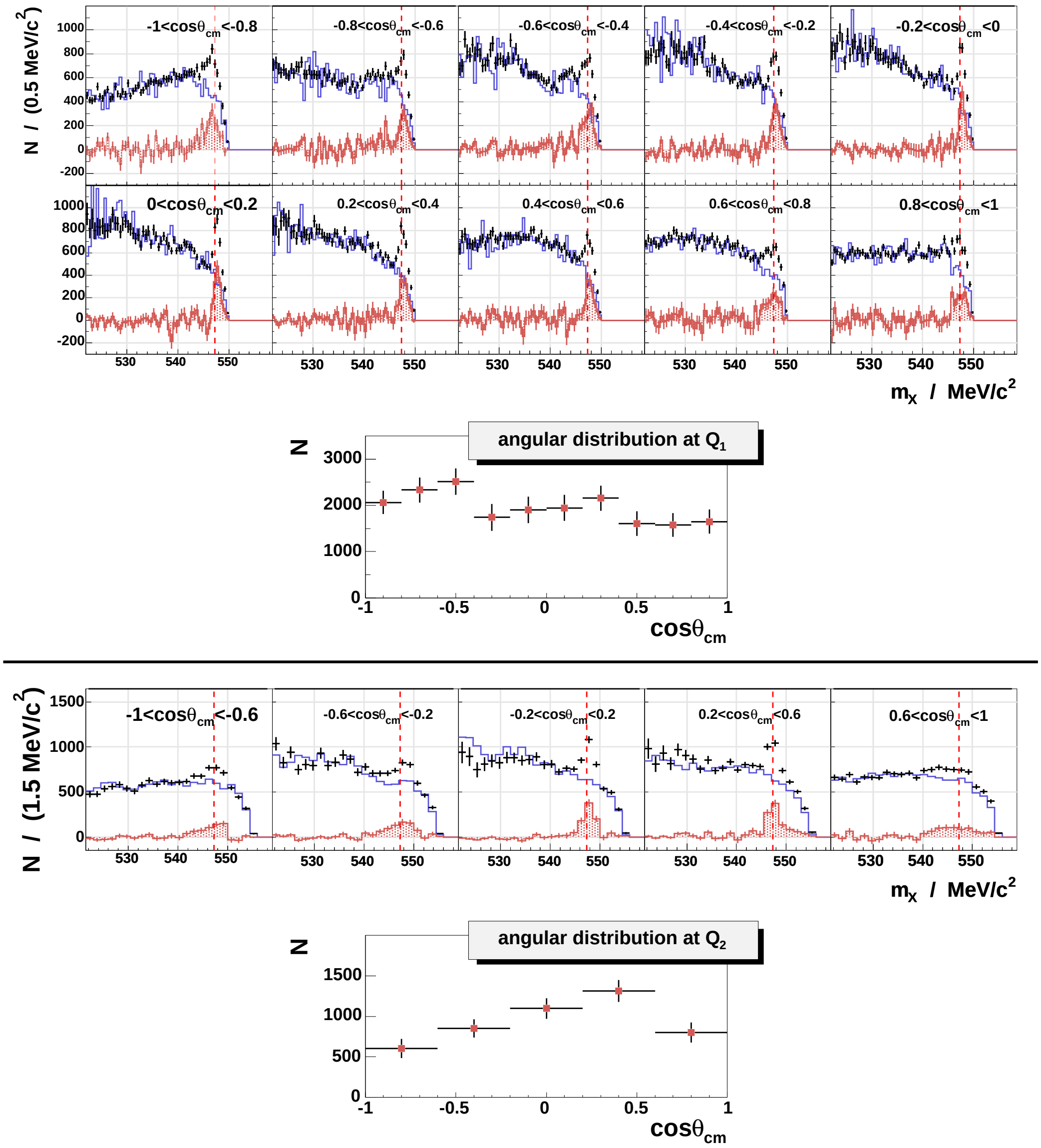

Figure 3.17: The course of extraction of an angular distribution. The upper part concerns data at Q_1, the lower one represents data at Q_2. From the missing mass spectra obtained above the η production threshold (black) those obtained below threshold and scaled by phase space and luminosity (blue) are subtracted. Both sets are corrected for acceptance before subtraction. The results are corrected with the reversed acceptance correction simulated for background and those spectra (maroon) are integrated. The angular bin integrals are subsequently corrected with the acceptance correction appropriate for the isotropic η production distribution. The unnormalised angular distributions obtained this way are plotted below the missing mass spectra.

It is well known, that inefficiencies in the MWDC response are likely to be located at the end of cells, close to field wires. Following this track, a simulation of the acceptance was performed assuming small inefficiencies at the end of each cell (1 mm in the 19.8 mm long cell). The results obtained with this acceptance corrections are labelled *ineff*.

MWDC position resolution is not well defined since the position spread is not gaussian. In simulations, however, a gaussian shape was assumed. As a default value 0.07 mm was taken. Another acceptance simulation was also performed assuming the position resolution of 0.2 mm in order to check the influence of this parameter. This set of acceptance corrections is labelled *res02*.

This investigation yielded four different results concerning the angular distributions as well as the total the cross section. To determine the systematic uncertainties having origins in the sources listed above, those results were set against each other and the scatter of the results for each angular bin was read out. The biggest discrepancy was assigned to the systematic error of a bin content. As the total cross section was considered separately, to exclude the differences in angular distributions resulting from different total number of η production events, the angular distribution spectra were normalised to one before comparing. Fig. 3.18 shows sets of the normalised angular distributions for both excess energies and the deduced bin errors.

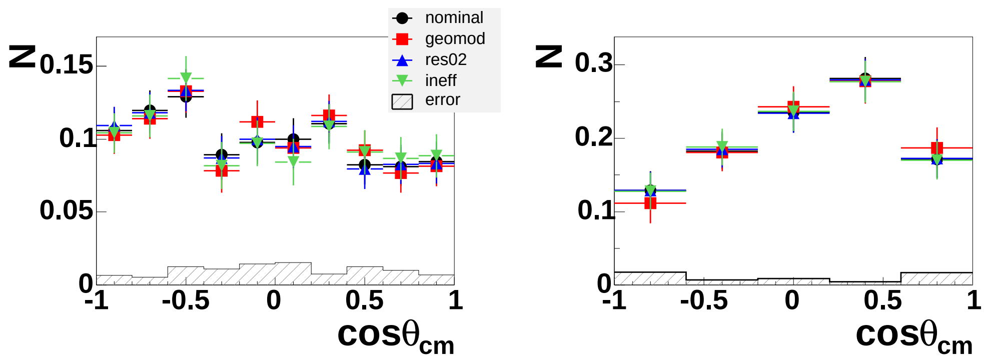

Figure 3.18: Angular distributions at Q_1 (left) and Q_2 (right) obtained with different analyses (a detailed description of those in the text). Systematic errors (striped histograms) are calculated as the largest difference in the bin content of the whole histogram set.

Averaging over the sets of four angular distribution spectra is not well justified. None of the analyses is more reliable than the others, either. Thus, the choice of one from the set of four angular distribution spectra to represent the final distribution is somewhat arbitrary. Hereinafter the *nominal* angular distribution is chosen as the final result.

As mentioned in the beginning of this section, angular distributions for the $dd \to {}^4He\eta$ reaction must be symmetric around 90°, e.g. around 0, when presented as functions of $\cos\theta_{cm}$. One can see that, in spite of some scatter in the bin contents, angular distributions presented in fig. 3.18 contain a certain linear contribution. For Q_1 its slope is negative while for Q_2 positive. This is a consequence of an insufficient precision in tuning of the momentum reconstruction procedure. The accuracy of the reconstruction, in particular the p_z component of the momentum vector, is crucial to ensure the symmetry of angular distributions. The adjustment of the momentum reconstruction procedure described in sec. 3.4.1 allowed an accuracy of ca. 5 MeV/c for each momentum component. Clearly, for p_z it is not satisfactory. Therefore, by varying this momentum component within $\pm$5 MeV/c the offsets are found which restore the symmetry of angular distributions. The physics boundary $($symmetry of $\mathrm{d}N/\mathrm{d}\,(\cos\theta_{cm}))$ is used to do fine tuning of the momentum reconstruction removing effect of parameters which are inaccessible directly with a sufficient precision (as mentioned before, these are wire chambers positions, beam angle on the target, target position, central values of magnetic field, *etc.*). It was found that p_z must be corrected as follows:

$$
\begin{aligned}
p_z \quad &\rightarrow \quad p_z + 3\ \mathrm{MeV/c} \quad \text{for}\ \ Q_1\,, \\
p_z \quad &\rightarrow \quad p_z - 3\ \mathrm{MeV/c} \quad \text{for}\ \ Q_2\,.
\end{aligned}
$$

Those offsets are so small that they are considered unimportant for the acceptance calculation.

As for the transverse momentum components, the impact of their possible shift was investigated on simulated events. It was found that the modification of the angular bin content arising from offsets of 5 MeV/c imposed on p_x and p_y is on 1%–level and thus can be neglected.

Another point which needed investigation was the dependence of results on the angular distribution assumed for acceptance simulation. It was argued before, that the migration effects can be corrected in the right way only if the angular distribution of the event sample used in simulations was similar to the experimental one. In the case of the result obtained at Q_1, the production seems isotropic. For the angular distribution obtained at Q_2, however, there seems to be a relatively strong contribution proportional to $\cos^2\theta_{cm}$. A kind of an iterative procedure was applied: the experimental θ_{cm}–distribution was used as an input for acceptance simulations. Subsequently, data were reanalysed with that new acceptance correction and results were compared. The difference was added to systematic errors calculated before (both expressed in fraction of the bin content). Application of the acceptance correction simulated with the use of the experimental angular distribution as an input resulted in an increase of the contribution of the term proportional to $\cos^2\theta_{cm}$ by ca. 5%. For the final result at Q_2 this acceptance correction was applied.

In fig. 3.19 the final shape of the angular distributions for both excess energies above the η production threshold is displayed. The striped histograms show total systematic errors derived in the way presented above.

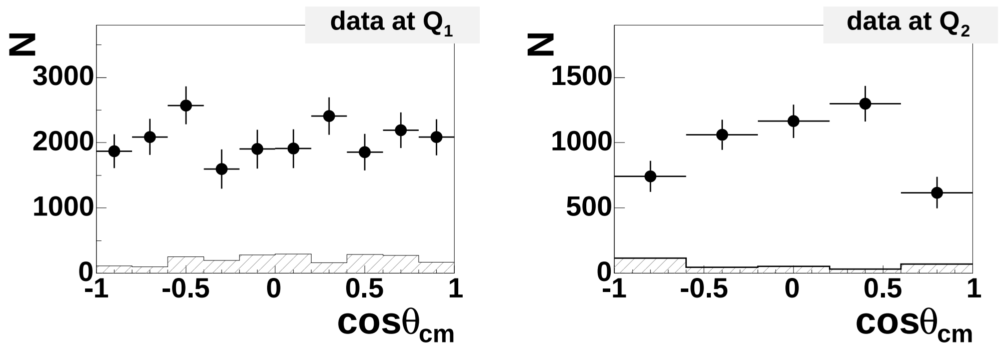

Figure 3.19: Unnormalised angular distributions for the $\mathrm{dd} \to {}^4\mathrm{He}\eta$ reaction at the two excess energies investigated in the experiment. Error bars attached to the points represent statistical errors. Systematic uncertainties are displayed as striped bars.

3.5 Luminosity determination

In order to normalise the results of the previous sections absolutely, it is necessary to determine integrated luminosities for all energies. Data for two processes involving helium nuclei can be exploited for this purpose: $\mathrm{dd} \to {}^4\mathrm{He}X$ and $\mathrm{dd} \to {}^3\mathrm{He}n$. The first reaction is preferable since its registration consists in detection of ${}^4\mathrm{He}$ particle, just as in the case of $\mathrm{dd} \to {}^4\mathrm{He}\eta$. Moreover, ${}^4\mathrm{He}$ particles stemming from both reactions have similar momenta (partially overlapping – these are events from the η peak in the missing mass and events from the background below the peak). Therefore when normalising to the $\mathrm{dd} \to {}^4\mathrm{He}X$ process, uncertainties originating from the detection setup efficiency cancels out completely and uncertainties of the acceptance cancel partially. For these reasons the normalisation to $\mathrm{dd} \to {}^4\mathrm{He}X$ data will be used to obtain final results, while luminosity determination based on $\mathrm{dd} \to {}^3\mathrm{He}n$ will serve as an additional, independent check.

3.5.1 Normalisation to dd→^{4}He X data

Differential cross sections $\mathrm{d}^2\sigma/\mathrm{d}p\,\mathrm{d}\Omega_{LAB}$ for the inclusive helium production in the dd collisions were measured by the Banaigs group [62] at several beam momenta between 1.89 GeV/c and 3.82 GeV/c. Table 3.2 summarises the data.

The events with η production ($X = \eta$) for beam momenta as in the experiment are located around $\theta_{LAB} = 0°$ and $p = 2.05$ GeV/c. This is the region of the central bump in the three–peak structure spectra. Thus, the cross section behaviour was parametrised in the region of that bump by a gaussian function with parameters dependent on the polar

p_{beam} / GeV/c	θ_{LAB} / degrees
1.89	0.3
2.10	0.3
2.29	**0.3**
2.50	**0.3, 4.5, 6.4, 7.4, 8.3**, 11.0
2.70	**0.3**
3.32	0.3
3.66	0.3
3.82	0.3

Table 3.2: Beam momenta and laboratory angles at which the differential cross sections for $\mathrm{dd} \rightarrow {}^4\mathrm{He}\,\mathrm{X}$ are available. Highlighted data sets were used to interpolation.

angle and the beam momentum:

$$\frac{\mathrm{d}^2\sigma}{\mathrm{d}p\,\mathrm{d}\Omega_{LAB}}(p,\theta_{LAB},p_{beam}) = N \cdot exp\left(-\frac{1}{2}\frac{(p-Mean)^2}{Sigma^2}\right) \tag{3.3}$$

where

$$\begin{aligned} N &= N(p_{beam},\theta_{LAB}) = Pol2(p_{beam}) \cdot Pol2(\theta_{LAB}) \ , \\ Mean &= Mean(p_{beam}) = Pol2(p_{beam}) \ , \\ Sigma &= Sigma(p_{beam},\theta_{LAB}) = Pol2(p_{beam}) \cdot Pol2(\theta_{LAB}) \ . \end{aligned}$$

$Pol2()$, as before, denotes a second–order polynomial. The dependence on θ_{LAB} is known only at a beam momentum of 2.5 GeV/c. Therefore for the parametrisation it was assumed that the same θ_{LAB}–dependence is valid in the whole investigated beam momentum range. The behaviour fitted to the Banaigs data was compared with the one observed in the experiment (which was, of course, not normalised absolutely). They were consistent within 5%. Fig. 3.20 displays a two–dimensional result of that parametrisation at a fixed beam momentum equal to the lowest one studied in the experiment. It is worth noticing that the cross section is interpolated between the beam momenta, at which the η production either is not allowed ($p_{beam} = 2.29$ GeV/c is below threshold) or is only a small correction, which can be neglected when compared with the two pion production (for p_{beam} =2.5 GeV/c and higher). Thus, to calculate the luminosity only background events should be taken into account. For the measurement below the η production threshold this is done automatically. For the two higher beam momenta it is done by exploiting the measurement below threshold together with the scaling factor needed to match background amplitudes.

The obtained function describing the double differential cross section of $\mathrm{dd} \rightarrow {}^4\mathrm{He}\,\mathrm{X}$ was integrated over the the region covered by the acceptance of the forward detection system:

$$\sigma_X(p_{beam}) = \int_{\phi=0}^{\phi=\pi}\int_{\theta_{LAB}=0}^{\theta_{LAB}=2.7^\circ}\int_{p=1.95}^{p=2.15}\frac{\mathrm{d}^2\sigma}{\mathrm{d}p\,\mathrm{d}\Omega_{LAB}}\,\sin\theta_{LAB}\,\mathrm{d}\theta_{LAB}\,\mathrm{d}p\,\mathrm{d}\phi\,. \tag{3.4}$$

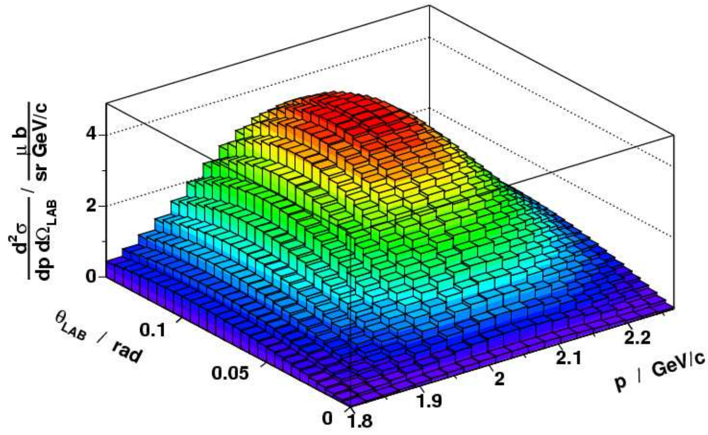

Figure 3.20: Parametrised double differential cross section of the reaction dd $\rightarrow$ ^{4}He X at $p_{beam} = 2.328$ GeV/c.

Results are collected in table 3.3.

p_{beam} / GeV/c	σ_X / nb 1.95 GeV/c$< p <$2.15 GeV/c $0< \phi < \pi$ $0< \theta_{LAB} < 2.7^\circ$
2.328	43.91
2.343	42.19
2.358	40.22

Table 3.3: Total cross sections of dd $\rightarrow$ ^{4}He X in the indicated range of ^{4}He kinematic variables. The numbers are obtained by integration of the interpolated double differential cross section of [62].

As mentioned before, the accuracy of the interpolation is estimated to amount 5%. Moreover, the data used for interpolation are the subject of a 15% uncertainty concerning the absolute normalisation.

Let us adopt the following notation:

σ_i	–	the total cross section for η production at an excess energy Q_i,
$\sigma_{X,i}$	–	the total cross section for $\mathrm{dd} \rightarrow {}^4\mathrm{He}\,\mathrm{X}$ at an excess energy Q_i and momentum vector of outgoing ${}^4\mathrm{He}$ fulfilling conditions listed in table 3.3,
N_X	–	the number of events fulfilling those conditions detected at Q_0,
$N_{\eta,i}$	–	the number of events with η production at Q_i,
W_i	–	the weight assigned to the subthreshold events at phase space scaling to Q_i,
F_i	–	the scaling factor for the phase–space–scaled background spectra to match background in the spectra obtained above threshold at Q_i,
L_i	–	the integrated luminosity at an excess energy Q_i.

The key relations are:

$$\sigma_i = \frac{N_{\eta,i}}{L_i}\,, \tag{3.5}$$

$$L_i = \frac{N_X \cdot W_i \cdot F_i}{\sigma_{X,i}}\,. \tag{3.6}$$

The efficiency correction is omitted in eq. 3.5 since it affects background and signal events in the same way. The acceptance correction was performed elsewhere. The numerator in the right hand side of eq. 3.6 approximates the number of background events observed in the region of interest at the positive excess energies. They cannot be extracted directly due to the fact that the application of the restrictions listed in table 3.3 reshapes the missing mass spectrum in a way which makes an estimate of the η production events impossible.

The numbers are used to calculate total cross sections are set together in table 3.4. Errors quoted here are of statistical origin.

	data at Q_1 $(i=1)$	data at Q_2 $(i=2)$
$N_{\eta,i}$	$20\,480 \pm 900$	$4\,890 \pm 280$
F_i	4.699 ± 0.046	0.845 ± 0.013
W_i	1.01209	1.02415
$\sigma_{X,i}$	42.19	40.22
N_X	$13\,890 \pm 130$	

Table 3.4: The numbers used for calculation of the total cross sections. Where applicable, statistical errors are given.

The calculation based on those numbers yields:

$$\begin{aligned} \sigma_1 &= 13.1 \,\pm\, (0.7)_{stat.}\ \text{nb}\,, \\ \sigma_2 &= 16.4 \,\pm\, (1.0)_{stat.}\ \text{nb}\,. \end{aligned} \tag{3.7}$$

It is also worthwhile to write out the integrated luminosities and their statistical errors explicitly:

$$
\begin{aligned}
L_0 &= 316.3 \pm (3.0)_{stat.}\ \mathrm{nb}^{-1}\,, \\
L_1 &= 1566\ \pm (21)_{stat.}\ \mathrm{nb}^{-1}\,, \\
L_2 &= 298.9 \pm (5.4)_{stat.}\ \mathrm{nb}^{-1}\,.
\end{aligned} \tag{3.8}
$$

Estimation of the systematic errors was done in a way similar to that for the angular distributions. Each of the four independent analyses performed (for the detailed description see sec. 3.4.5) yielded a certain number for the total cross section. The largest difference is one of the components of the systematic error. Another component comes from the interpolation of the cross section. It is estimated to amount to 5% and is added linearly to the previous one. The overall uncertainty in the absolute normalisation of the Banaigs data also propagates onto these results. This component, however, according to a common manner, is not added to the rest but expressed in words since it affects both measured points in the same way. The systematic uncertainties of the measured cross sections amount to

$$
\Delta\sigma_{1,syst.} = 1.8\ \mathrm{nb}\,, \tag{3.9}
$$

$$
\Delta\sigma_{2,syst.} = 2.1\ \mathrm{nb}\,. \tag{3.10}
$$

3.5.2 Normalisation to dd→^{3}He n data

For the $\mathrm{dd} \to {}^3\mathrm{He}\,\mathrm{n}$ process the angular distributions were measured for several beam momenta between 1.1 GeV/c and 2.5 GeV/c [71]. Thus, there exists a possibility of interpolation to the beam momenta studied in the experiment. The original data are expressed in terms the momentum transfer as $\mathrm{d}\sigma/\mathrm{d}t$ and cover the cm angular range between 0 and 60°. They are recalculated to $\mathrm{d}\sigma/\mathrm{d}\Omega_{cm}$ according to the formula [72]

$$
\frac{\mathrm{d}\sigma}{\mathrm{d}\Omega_{cm}} = \frac{1}{\pi} p_{\mathrm{d}}\, p_{\mathrm{He}} \frac{\mathrm{d}\sigma}{\mathrm{d}t}\,. \tag{3.11}
$$

Data for beam momenta of 1.651 GeV/c, 1.890 GeV/c, 1.992 GeV/c and 2.492 GeV/c restricted to $\theta_{cm} < 20°$ were fitted with the following function

$$
\frac{\mathrm{d}\sigma}{\mathrm{d}\Omega_{cm}} = Pol2_0(\theta_{cm}) + Pol2_1(\theta_{cm}) \cdot p_{beam} + Pol2_2(\theta_{cm}) \cdot p_{beam}^2 \tag{3.12}
$$

where $Pol2()$ as usual denotes a second–order polynomial marked with an additional subscript to emphasise different parameters for polynomials multiplying different powers of p_{beam}. The fitted function describes a smooth surface falling down towards larger angles and beam momenta.

In the case of ^{3}He, acceptance was simulated using this parametrised cross section as an input distribution. The acceptance was expressed in terms of θ_{cm}. For the cm polar angles from the range between 3° and 14° it is smooth and this range was chosen for luminosity calculation.

Fig. 3.21 shows the acceptance corrected missing mass distribution obtained at the lowest beam momentum studied in the experiment.

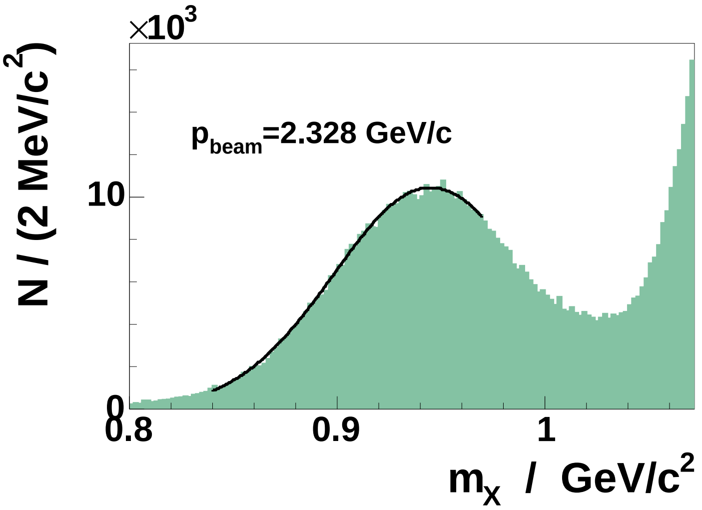

Figure 3.21: Missing mass of the reaction d(d,^{3}He) at a beam momentum of 2.328 GeV/c. The peak stems from the two–body reaction where next to the ^{3}He particle a neutron is produced.

Corresponding spectra for the two higher energies look almost identical, therefore they are not plotted here. The missing mass spectra were used to fit a shape of the neutron peak. From the fit parameters the total number of detected $\mathrm{dd} \to {}^3\mathrm{He\,n}$ events was calculated. Depending on the fit limits the result varied within 5%.

This information, together with the integral of $\mathrm{d}\sigma/\mathrm{d}\Omega_{cm}$ between 3° and 14° allowed an alternative way of luminosity determination as a ratio of the number of events to the cross section. All necessary quantities are set together in table 3.5.

p_{beam} / GeV/c	$\int_0^{2\pi} \mathrm{d}\phi \int_{3°}^{14°} \frac{\mathrm{d}\sigma}{\mathrm{d}\Omega_{cm}} \sin\theta_{cm}\, \mathrm{d}\theta_{cm}$ / nb	N_n	L_i / nb^{-1}
2.328	1912.71	606682	317
2.343	1854.72	2642995	1425
2.358	1798.64	459229	255

Table 3.5: Quantities necessary for the luminosity determination based on the $\mathrm{dd} \to {}^3\mathrm{He\,n}$ process and the results.

Also here it must be mentioned that the Bizard data exploited here are the subject of ca. 7% uncertainty in the absolute normalisation.

The obtained results are to be compared with those of eq. 3.8. Taking into account the uncertainties, the two sets of results are consistent with each other, which proves the reliability of the analysis.

4 Results and conclusions

4.1 Summary of experimental results

Let us summarise the results. The presented experiment comprised measurements of the total cross sections and angular distributions of the $\mathrm{dd} \to {}^4\mathrm{He}\eta$ reaction at two excess energies above the reaction threshold as well as a subthreshold measurement aiming at background study. The momenta in the final state as well as corresponding excess energies are listed below

$$\begin{aligned} p_{cm,1} &= (50 \pm 5) \ \text{MeV/c}, \\ Q_1 &= (2.6 \pm 0.6) \ \text{MeV}, \\ p_{cm,2} &= (86 \pm 4) \ \text{MeV/c}, \\ Q_2 &= (7.7 \pm 0.8) \ \text{MeV}. \end{aligned} \tag{4.1}$$

The analysis of experimental data presented in the previous chapter yielded the following total cross sections

$$\begin{aligned} \sigma_1 &= (13.1 \pm 0.7_{stat.} \pm 1.8_{syst.}) \ \text{nb}, \\ \sigma_2 &= (16.4 \pm 1.0_{stat.} \pm 2.1_{syst.}) \ \text{nb}, \end{aligned} \tag{4.2}$$

where the uncertainty in the overall normalisation of 15%, propagated from the $\mathrm{dd} \to {}^4\mathrm{He}\,\mathrm{X}$ data is not added to the systematic error.

The corresponding angular distributions are depicted in fig. 4.1. The distribution obtained at the excess energy Q_1 appears isotropic and the one measured at Q_2 reveals a strong angular dependence. In order to quantify these features both angular distributions were fitted with two functions each: a constant $Pol0(\cos^2\theta) = C_0$ and a modified second order polynomial $Pol2(\cos^2\theta) = C_0 \cdot \left(1 + C_2 \cos^2\theta\right)$. For fitting purposes systematic and statistical errors are added in squares. The curves being the fit results are superimposed on the experimental data in fig. 4.2 while the numbers are collected in table 4.1.

The analysis of the fit results leads to a conclusion, that at Q_1 the angular distribution is consistent with isotropic. A situation looks differently at Q_2, where the χ^2–value favours the $Pol2(\cos\theta)$ hypothesis with a relatively large C_2 coefficient.

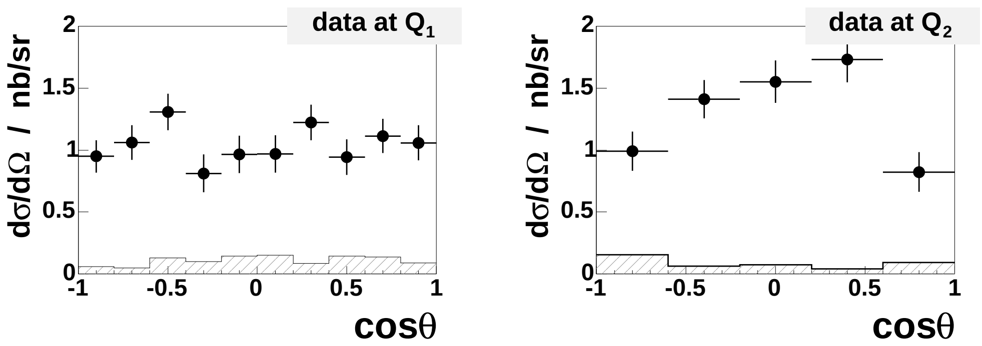

Figure 4.1: Experimental angular distributions. Error bars attached to the points represent statistical errors, while the systematic errors are drawn as striped histograms.

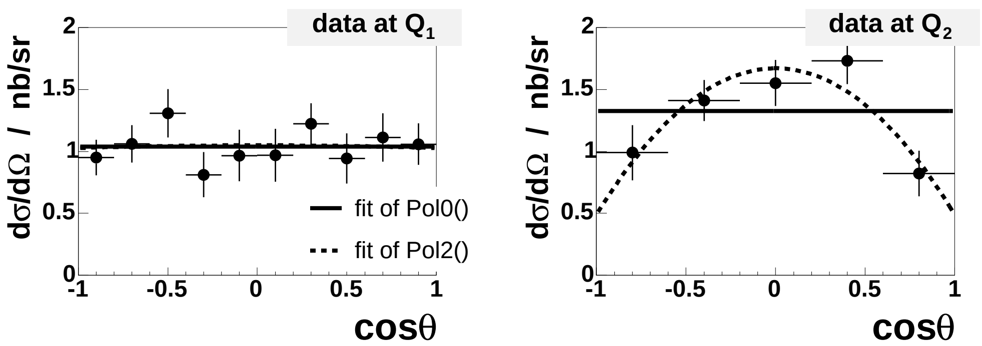

Figure 4.2: Fits of a constant and a second order polynomial to experimental angular distributions. At Q_1 the two curves overlap, while at Q_2 the fit of $Pol2(\cos\theta)$ much better describes the data.

	fit of $Pol0(\cos\theta)$		**fit of $Pol2(\cos\theta)$**		
	C_0	χ^2/ndf	C_0	C_2	χ^2/ndf
Q_1	1.041 ± 0.057	$5.64/9 = 0.63$	1.050 ± 0.092	0.02 ± 0.18	$5.63/8 = 0.70$
Q_2	1.326 ± 0.084	$16.10/4 = 4.03$	1.67 ± 0.13	-0.71 ± 0.16	$2.74/3 = 0.91$

Table 4.1: Results of the fits of experimental angular distributions.

4.2 Consistency with world data

The results of this work should be compared with the world data, i.e. total cross sections from [19, 25]. However, to address a question of their consistency, one should note that the [19] data were obtained with a polarised beam $m = \pm 1$. The group observed no signal of $\mathrm{dd} \to {}^4\mathrm{He}\eta$ for a beam polarisation $m = 0$ at $p_\eta = 48$ MeV/c. According to the discussion from sec. 1.2.5, very close to threshold when the entire production is in the s–wave, no signal is expected for $m = 0$, i.e. this result of Willis et al. is in line with the fact, that the angular distribution at $p_\eta = 50$ MeV/c measured at ANKE is isotropic.

The way of deriving the formula 1.21 implies that all terms related to the even partial waves appear only for beam polarisation $m = \pm 1$. Thus, assuming the presence of s– and d–wave one obtains the unpolarised cross section from the polarised one by multiplication by 2/3. The situation is different when one assumes that s– and p–wave contribute to the total production. In this case the $m = 0$ polarisation contributes to the C–term with a double weight of the $m = \pm 1$ contribution. Hence,

$$\left(\frac{\mathrm{d}\sigma}{\mathrm{d}\Omega}\right)_{m=\pm 1} = \tfrac{2}{9} p p_\eta \left[\tfrac{3}{2}|A_0|^2 + \tfrac{3}{4}|C|^2 p^2 p_\eta^2 \sin^2\theta\right], \tag{4.3}$$

$$\left(\frac{\mathrm{d}\sigma}{\mathrm{d}\Omega}\right)_{m=0} = \tfrac{2}{9} p p_\eta \cdot \tfrac{3}{2}|C|^2 p^2 p_\eta^2 \sin^2\theta\,, \tag{4.4}$$

which provides a correct spin averaged cross section. In order to compare the ANKE results with those of [19] it is necessary to use the $|C|^2$ amplitude extracted from the ANKE data and derive σ for the data of Willis et al. based upon eqs. 4.3 and 4.4:

$$\begin{aligned}
\sigma_{(s+p)-wave} &= \frac{4\pi}{3}\left[2\cdot\left\langle\left(\frac{\mathrm{d}\sigma}{\mathrm{d}\Omega}\right)_{m=\pm 1}\right\rangle + \left\langle\left(\frac{\mathrm{d}\sigma}{\mathrm{d}\Omega}\right)_{m=0}\right\rangle\right] \\
&= \frac{8\pi}{27} p p_\eta \left[2\cdot\left(\tfrac{3}{2}|A_0|^2 + \tfrac{1}{2}|C|^2 p^2 p_\eta^2\right) + \left(|C|^2 p^2 p_\eta^2\right)\right],
\end{aligned} \tag{4.5}$$

where $\langle\cdots\rangle$ represents averaging over the θ angle and $|A_0|^2$ is given by eq. 4.3 and the experimental cross section. Fig. 4.3 presents the data on the total cross section for the two scenarios, in which the s–wave is accompanied either by p–wave or d–wave. In each case the data points of Willis et al. have been recalculated according to the aforegiven description.

The ANKE results are, within errors, consistent with the SATURNE data independently on the partial wave composition assumed. Although they do not allow to exclude any of the investigated hypotheses the message concerning a contribution of higher partial waves is important.

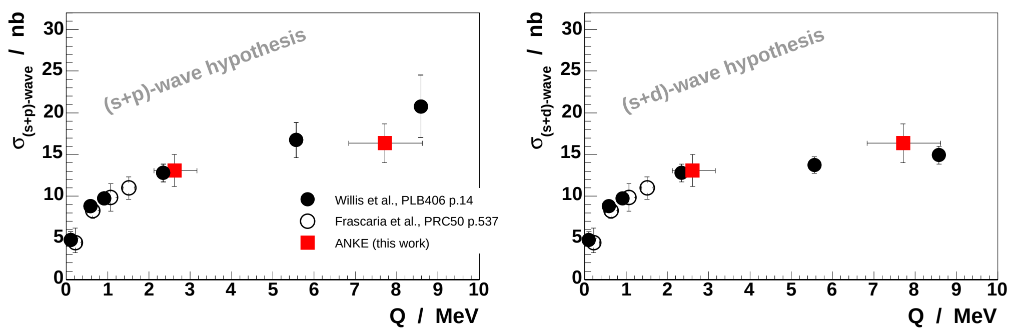

Figure 4.3: World data on the total cross section for dd $\to$ ^{4}Heη including the results of this work. The data of [19] (σ for $m = \pm 1$) have been recalculated to unpolarised cross section assuming that apart from s–wave also p–wave (left) or d–wave (right) contributes to the total production.

4.3 Consequences for partial amplitudes

The results of the previous section may be used to draw conclusions concerning the amplitude $|f|^2$ defined in sec. 1.2.2 on page 5. This amplitude is in close relation to $|A_0|^2$ from eq. 1.21

$$\frac{2}{9} p p_\eta |A_0|^2 = \frac{p_\eta}{p} |f_s|^2 \, ,$$

where the amplitude f is supplied with a subscript s to stress that it is the amplitude of the s–wave production.

The angular distribution alone does not provide sufficient information to extract all of the amplitudes in the formula 1.21. One can, however, consider the special cases, when two of the four amplitudes vanish. Such discussion will result in different contributions of the s–wave production in the total yield. For each discussed case the corresponding set of $|f_s|^2$ can be fitted with the formula 1.5 resulting in different values of the real part of the scattering length $\Re\mathfrak{e}\, a$. As the real and imaginary parts of a are very strongly coupled in the fit, the imaginary part derived in [19] will be adopted, leaving f_B and $\Re\mathfrak{e}\, a$ as the only free parameters. Variation of the result between different assumptions concerning the partial amplitudes will give an impression on the sensitivity of the $\Re\mathfrak{e}\, a$ to those assumptions.

Let us write explicitly the conditions, formulae and the values of the amplitudes obtained from the fit of angular distribution at Q_2 (for momenta in GeV/c).

i) $A_2 = D = 0$ corresponds to the presence of s– and p–waves,

$$\frac{d\sigma}{d\Omega} = \frac{2}{9} p p_\eta \left[|A_0|^2 + |C|^2 p^2 p_\eta^2 \sin^2\theta \right] \, ,$$

$$|A_0|^2 = 25 \pm 13 \, ,$$

$$|C|^2 = (7.6 \pm 2.1) \cdot 10^3 \, ,$$

$$|f_s|^2 = (5.9 \pm 3.3) \text{ nb/sr} \, ,$$

ii) $C = D = 0$ describes onset of a d–wave (no p–wave contribution) with a vanishing D amplitude,

$$\frac{\mathrm{d}\sigma}{\mathrm{d}\Omega} = \tfrac{2}{9}pp_\eta\left[|A_0|^2 + 2\mathfrak{Re}(A_0^*A_2)\,p^2p_\eta^2\cos^2\theta\right] ,$$

$$\begin{aligned} |A_0|^2 &= 84.7 \pm 6.4\,, \\ \mathfrak{Re}\,(A_0^*A_2) &= (-3.8 \pm 1.1)\cdot 10^3\,, \\ |f_s|^2 &= (20.1 \pm 3.4)\,\text{nb/sr}\,, \end{aligned}$$

iii) $C = A_2 = 0$ represents emergence of d–wave with vanishing A_2 amplitude,

$$\frac{\mathrm{d}\sigma}{\mathrm{d}\Omega} = \tfrac{2}{9}pp_\eta\left[|A_0|^2 - 2\mathfrak{Re}(A_0^*D)\,, p_\eta^2\sin^2\theta\right] .$$

This case is mathematically equivalent to i) and so will yield the same value of $|A_0|^2$. Therefore it will not be treated separately here.

The aforegiven errors of $|A_0|^2$, $|C|^2$ and $\mathfrak{Re}\,(A_0^*A_2)$ are obtained from the fitting procedure, while the errors of the amplitudes $|f_s|^2$ contain already uncertainty of the total cross section added in squares to the error resulting from the fit.

The two points of Willis et al. at the highest energies have been analysed in the way described in the previous section in order to extract the $|A_0|^2$ and subsequently the $|f_s|^2$ amplitude using values of $|C|^2$ and $\mathfrak{Re}\,(A_0^*A_2)$ determined in the ANKE experiment at the excess energy Q_2.

The results of this investigation are displayed in fig. 4.4.

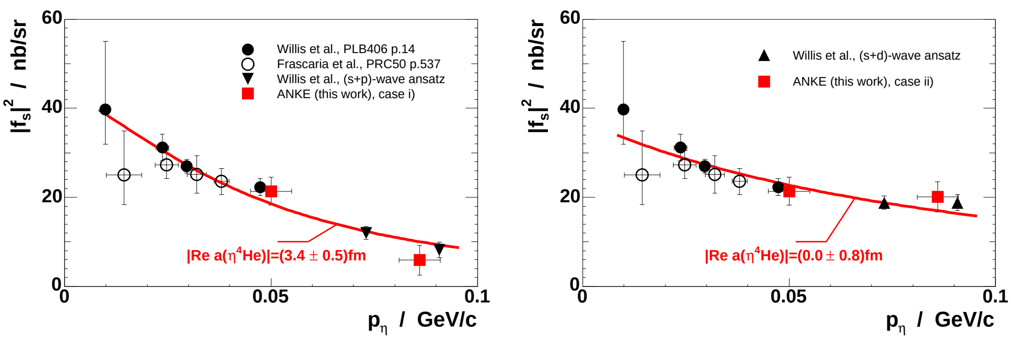

Figure 4.4: The s–wave reaction amplitudes calculated under different assumptions concerning the partial wave composition of the total dd $\to$ ^{4}Heη production. Left: only s– and p–wave contribute. Right: s– and d–wave occur, with an additional demand of $D = 0$. Curves represent fits of the s–wave scattering length.

The following values of $|\mathfrak{Re}\,a(\eta^4\text{He})|$ have been obtained for the two discussed cases:

$$\begin{aligned} \text{i)}\quad |\mathfrak{Re}\,a(\eta^4\text{He})| &= (3.4 \pm 0.5)\ \text{fm}\,, \\ \text{ii)}\quad |\mathfrak{Re}\,a(\eta^4\text{He})| &= (0.0 \pm 0.8)\ \text{fm}\,. \end{aligned}$$

The large difference indicates enormous sensitivity of the real part of the η^4He scattering length to the onset of higher partial waves. Moreover, it shows that it is not only important to affirm that the higher partial waves contribute, but it turns out necessary to identify the contribution of individual waves. This question can be addressed in a polarised measurement.

5 Outlook

The experiment presented in the previous chapters aimed at a measurement of the $\mathrm{dd} \to {}^4\mathrm{He}\eta$ reaction in the excess energy region, where data concerning the total cross section were already available. However, the experiment provided, apart from the total cross sections, information on the angular distributions which had never been measured before. A strong variation of the reaction cross section with angle was observed already as close to threshold as Q =7.7 MeV.

The experimental programme found its continuation in the second beam time performed in November 2003. The measurement comprised two beam momenta: 2.40 GeV/c and 2.46 GeV/c corresponding to Q–values of 22 MeV and 43 MeV, respectively. Due to a larger opening angle of the ^{4}He–cone, the small acceptance multiwire drift chambers had to be replaced by a larger set of proportional chambers.

The data are currently under analysis. Preliminary missing mass spectra are shown in fig. 5.1. The presented spectra are not corrected for acceptance losses. Vertical lines

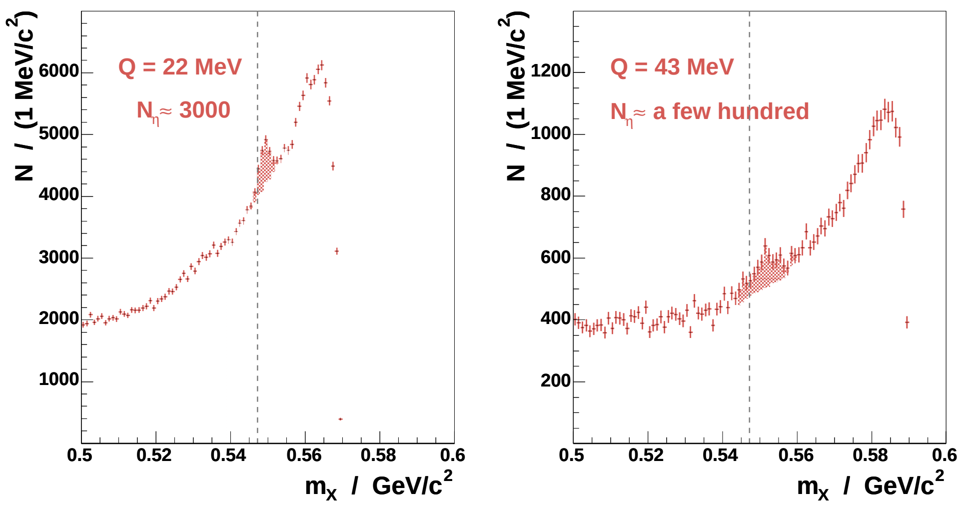

Figure 5.1: Preliminary missing mass spectra obtained at beam momenta of 2.40 GeV/c (left) and 2.46 GeV/c (right).

indicate the η–meson mass. Enhancements corresponding to the $\mathrm{dd} \rightarrow {}^4\mathrm{He}\eta$ reaction (shaded peaks) are slightly off the expected value, which indicates that for these data the momentum reconstruction procedures need tuning of the parameters as well. Due to worse experimental conditions the collected statistics is much poorer and the extraction of angular distributions is in doubt. In this energy region, however, no data on the total cross section exist either. Therefore, even this information alone is very valuable.

In autumn 2003 another experiment concerning measurement of $\mathrm{dd} \rightarrow {}^4\mathrm{He}\eta$ was proposed to the Programme Advisory Committee of the COSY accelerator by the GEM collaboration [73]. Its main goal is a measurement of the tensor and vector analysing powers t_{20} and t_{11} along with the differential cross sections for several beam momenta starting at 2.4 GeV/c. It will provide deeper insight in the structure of the $\mathrm{dd} \rightarrow {}^4\mathrm{He}\eta$ amplitude and will contribute to further studies of the reaction mechanism.

A List of runs

Runs used in the analysis of the beam momentum of 2.328 GeV/c.

Run	Tape	Time	Events	I_{beam} $[10^9/\mathrm{s}]$	Trigger
5233	4	2003/01/30, 13:52 - 14:57	10,164,538	50.0	T1 FD int, T2 FD/999, T4 Scaler
5234	4	2003/01/30, 14:58 - 15:55	7,848,260	50.0	T1 FD int, T2 FD/9990, T3 Scaler
5236	4	2003/01/30, 16:26 - 17:28	8,611,461	50.0	T1 FD int, T2 FD/9990, T3 Scaler
5237	4	2003/01/30, 17:29 - 18:42	10,017,337	50.0	T1 FD int, T2 FD/9990, T3 Scaler
5238	4	2003/01/30, 18:44 - 20:04	9,933,945	50.0	T1 FD int, T2 FD/9990, T3 Scaler
5239	4	2003/01/30, 20:05 - 21:12	6,800,808	50.0	T1 FD int, T2 FD/9990, T3 Scaler
5240	4	2003/01/30, 21:13 - 22:22	5,983,975	50.0	T1 FD int, T2 FD/9990, T3 Scaler
5241	4	2003/01/30, 22:22 - 00:40	10,013,740	50.0	T1 FD int, T2 FD/9990, T3 Scaler
5242	4	2003/01/31, 00:44 - 03:02	10,042,749	50.0	T1 FD int, T2 FD/9990, T4 Scaler
5243	4	2003/01/31, 03:27 - 06:00	10,421,538	50.0	T1 FD int, T2 FD/9990, T4 Scaler
5244	5	2003/01/31, 06:07 - 08:15	6,219,119	50.0	T1 FD int, T2 FD/9990, T4 Scaler
5245	5	2003/01/31, 08:17 - 09:28	6,174,739	38.8	T1 FD int, T2 FD/9990, T4 Scaler
5246	5	2003/01/31, 09:37 - 10:11	2,864,032	38.8	T1 FD int, T2 FD/9990, T4 Scaler
5247	5	2003/01/31, 10:45 - 11:51	8,823,228	38.8	T1 FD int, T2 FD/9990, T4 Scaler
5248	5	2003/01/31, 12:06 - 13:44	10,126,065	28.6	T1 FD int, T2 FD/9990, T4 Scaler
5249	5	2003/01/31, 13:46 - 14:37	4,611,622	28.6	T1 FD int, T2 FD/9990, T4 Scaler

Runs used in the analysis of the beam momentum of 2.343 GeV/c.

Run	Tape	Time	Events	I_{beam} [10^9/s]	Trigger
5250	5	2003/01/31, 15:20 - 16:43	9,936,637	68.0	T1 FD int, T2 FD/9990, T4 Scaler
5251	5	2003/01/31, 16:45 - 18:17	10,284,951	68.0	T1 FD int, T2 FD/9990, T4 Scaler
5252	5	2003/01/31, 18:18 - 19:49	9,529,954	68.0	T1 FD int, T2 FD/9990, T4 Scaler
5253	5	2003/01/31, 19:53 - 21:19	9,166,111	68.0	T1 FD int, T2 FD/9990, T4 Scaler
5254	5	2003/01/31, 21:24 - 22:10	5,425,122	68.0	T1 FD int, T2 FD/9990, T4 Scaler
5255	5	2003/01/31, 22:18 - ??:??	6,583,214	68.0	T1 FD int, T2 FD/9990, T4 Scaler
5256	6	2003/01/31, 23:21 - 00:55	10,468,964	39.0	T1 FD int, T2 FD/9990, T4 Scaler
5257	6	2003/02/01, 00:56 - 02:28	12,280,557	36.5	T1 FD int, T2 FD/9990, T4 Scaler
5258	6	2003/02/01, 02:29 - 03:49	10,424,072	36.5	T1 FD int, T2 FD/9990, T4 Scaler
5259	6	2003/02/01, 03:51 - 05:27	10,208,556	36.5	T1 FD int, T2 FD/9990, T4 Scaler
5260	6	2003/02/01, 05:28 - 07:10	10,009,511	24.5	T1 FD int, T2 FD/9990, T4 Scaler
5261	6	2003/02/01, 07:12 - 08:42	10,015,232	38.5	T1 FD int, T2 FD/9990, T4 Scaler
5262	6	2003/02/01, 08:49 - 10:22	10,021,642	38.5	T1 FD int, T2 FD/9990, T4 Scaler
5263	6	2003/02/01, 10:24 - 12:04	10,010,858	36.3	T1 FD int, T2 FD/9990, T4 Scaler
5264	6	2003/02/01, 12:07 - 13:53	10,008,785	32.4	T1 FD int, T2 FD/9990, T4 Scaler
5265	7	2003/02/01, 13:56 - 15:51	10,216,121	32.4	T1 FD int, T2 FD/9990, T4 Scaler
5266	7	2003/02/01, 15:54 - 17:49	11,321,472	32.4	T1 FD int, T2 FD/9990, T4 Scaler
5267	7	2003/02/01, 17:54 - 19:29	10,003,318	32.4	T1 FD int, T2 FD/9990, T4 Scaler
5268	7	2003/02/01, 19:31 - 21:18	10,467,320	32.4	T1 FD int, T2 FD/9990, T4 Scaler
5269	7	2003/02/01, 21:19 - 22:55	10,018,145	32.4	T1 FD int, T2 FD/9990, T4 Scaler
5270	7	2003/02/01, 22:56 - 00:31	10,014,408	32.4	T1 FD int, T2 FD/9990, T4 Scaler
5271	7	2003/02/02, 00:32 - 01:41	7,194,947	32.4	T1 FD int, T2 FD/9990, T4 Scaler
5273	7	2003/02/02, 02:27 - 03:39	10,016,194	32.4	T1 FD int, T2 FD/9990, T4 Scaler
5274	7	2003/02/02, 03:41 - 04:49	10,226,597	32.4	T1 FD int, T2 FD/9990, T4 Scaler
5275	8	2003/02/02, 05:07 - 06:37	10,728,303	32.4	T1 FD int, T2 FD/9990, T4 Scaler
5276	8	2003/02/02, 06:39 - 08:25	10,382,816	32.4	T1 FD int, T2 FD/9990, T4 Scaler
5277	8	2003/02/02, 08:29 - 10:18	11,630,469	32.4	T1 FD int, T2 FD/9990, T4 Scaler
5278	8	2003/02/02, 10:19 - 12:26	10,663,075	32.4	T1 FD int, T2 FD/9990, T4 Scaler
5279	8	2003/02/02, 12:27 - 13:35	6,029,496	32.4	T1 FD int, T2 FD/9990, T4 Scaler
5307	10	2003/02/10, 13:17 - 13:36	3,050,434	?	T1 FD int, T2 FD/9990, T4 Scaler
5308	10	2003/02/10, 13:38 - 13:38	51,801	?	T1 FD int, T2 FD/9990, T4 Scaler
5309	10	2003/02/10, 13:41 - 14:31	5,092,141	?	T1 FD int, T2 FD/9990, T4 Scaler
5310	10	2003/02/10, 14:31 - 15:41	5,656,251	?	T1 FD int, T2 FD/9990, T4 Scaler
5311	10	2003/02/10, 16:09 - 16:14	756,410	56.0	T1 FD int, T2 FD/9990, T4 Scaler
5312	10	2003/02/10, 16:15 - 17:10	10,007,937	56.0	T1 FD int, T2 FD/9990, T4 Scaler
5313	10	2003/02/10, 17:15 - 17:20	487,644	56.0	T1 FD int, T2 FD/9990, T4 Scaler
5314	10	2003/02/10, 17:22 - 17:22	82,653	56.0	T1 FD int, T2 FD/9990, T4 Scaler
5315	10	2003/02/10, 17:29 - 18:26	10,014,307	56.0	T1 FD int, T2 FD/9990, T4 Scaler
5316	10	2003/02/10, 18:27 - 19:16	6,805,761	56.0	T1 FD int, T2 FD/9990, T4 Scaler
5317	10	2003/02/10, 19:18 - 19:39	1,541,257	56.0	T1 FD int, T2 FD/9990, T4 Scaler
5318	10	2003/02/10, 19:43 - 19:43	813,381	56.0	T1 FD int, T2 FD/9990, T4 Scaler
5319	10	2003/02/10, 19:52 - 20:07	2,336,280	56.0	T1 FD int, T2 FD/9990, T4 Scaler
5320	10	2003/02/10, 20:08 - 20:21	2,193,744	56.0	T1 FD int, T2 FD/9990, T4 Scaler
5321	10	2003/02/10, 20:25 - 21:15	7,878,228	56.0	T1 FD int, T2 FD/9990, T4 Scaler
5322	10	2003/02/10, 21:23 - 21:27	574,048	56.0	T1 FD int, T2 FD/9990, T4 Scaler
5323	10	2003/02/10, 21:30 - 22:21	9,068,863	56.0	T1 FD int, T2 FD/9990, T4 Scaler

Run	Tape	Time	Events	I_{beam} $[10^9/\mathrm{s}]$	Trigger
5324	10	2003/02/10, 22:23 - 23:28	11,017,422	56.0	T1 FD int, T2 FD/9990, T4 Scaler
5325	10	2003/02/10, 23:29 - 23:39	1,658,945	56.0	T1 FD int, T2 FD/9990, T4 Scaler
5326	10	2003/02/10, 23:40 - 00:23	7,504,337	56.0	T1 FD int, T2 FD/9990, T4 Scaler
5327	11	2003/02/11, 00:45 - 02:17	16,979,862	56.0	T1 FD int, T2 FD/9990, T4 Scaler
5328	11	2003/02/11, 02:19 - 03:06	8,238,980	56.0	T1 FD int, T2 FD/9990, T4 Scaler
5329	11	2003/02/11, 03:09 - 04:19	12,129,803	56.0	T1 FD int, T2 FD/9990, T4 Scaler
5331	11	2003/02/11, 04:29 - 05:30	9,551,419	40.0	T1 FD int, T2 FD/9990, T4 Scaler
5332	11	2003/02/11, 05:31 - 06:42	10,704,391	40.0	T1 FD int, T2 FD/9990, T4 Scaler
5333	11	2003/02/11, 06:43 - 07:21	5,492,237	40.0	T1 FD int, T2 FD/9990, T4 Scaler
5334	11	2003/02/11, 07:21 - 07:55	30,947	40.0	T1 FD int, T2 FD/9990, T4 Scaler
5335	11	2003/02/11, 09:46 - 10:22	5,959,391	60.0	T1 FD int, T2 FD/9990, T4 Scaler
5336	11	2003/02/11, 10:24 - 11:19	10,452,833	64.0	T1 FD int, T2 FD/9990, T4 Scaler
5337	11	2003/02/11, 11:20 - 11:38	3,039,737	64.0	T1 FD int, T2 FD/9990, T4 Scaler
5338	11	2003/02/11, 11:40 - 12:42	11,553,724	?	T1 FD int, T2 FD/9990, T4 Scaler
5339	12	2003/02/11, 12:54 - 13:29	3,253,836	?	T1 FD int, T2 FD/9990, T4 Scaler
5341	12	2003/02/11, 13:37 - 14:25	10,070,980	?	T1 FD int, T2 FD/9990, T4 Scaler
5342	12	2003/02/11, 14:26 - 15:10	8,720,896	?	T1 FD int, T2 FD/9990, T4 Scaler
5343	12	2003/02/11, 15:11 - 16:03	10,682,674	?	T1 FD int, T2 FD/9990, T4 Scaler
5344	12	2003/02/11, 16:05 - 16:55	10,023,876	64.0	T1 FD int, T2 FD/9990, T4 Scaler
5345	12	2003/02/11, 16:56 - 17:48	10,523,739	64.0	T1 FD int, T2 FD/9990, T4 Scaler
5346	12	2003/02/11, 17:50 - 18:10	3,616,043	64.0	T1 FD int, T2 FD/9990, T4 Scaler
5347	12	2003/02/11, 18:12 - 19:04	10,202,086	64.0	T1 FD int, T2 FD/9990, T4 Scaler
5348	12	2003/02/11, 19:06 - 19:58	10,246,917	64.0	T1 FD int, T2 FD/9990, T4 Scaler
5350	13	2003/02/11, 20:16 - 21:09	10,114,827	64.0	T1 FD int, T2 FD/9990, T4 Scaler
5351	13	2003/02/11, 21:11 - 22:05	10,485,967	64.0	T1 FD int, T2 FD/9990, T4 Scaler
5352	13	2003/02/11, 22:06 - 22:59	10,352,102	64.0	T1 FD int, T2 FD/9990, T4 Scaler
5353	13	2003/02/11, 23:00 - 23:52	9,935,866	64.0	T1 FD int, T2 FD/9990, T4 Scaler
5354	13	2003/02/11, 23:53 - ??:44	10,078,142	64.0	T1 FD int, T2 FD/9990, T4 Scaler
5355	13	2003/02/12, 00:46 - 01:05	3,870,400	64.0	T1 FD int, T2 FD/9990, T4 Scaler
5356	13	2003/02/12, 01:07 - 02:00	10,147,065	64.0	T1 FD int, T2 FD/9990, T4 Scaler
5357	13	2003/02/12, 02:01 - 02:55	10,341,215	64.0	T1 FD int, T2 FD/9990, T4 Scaler
5358	13	2003/02/12, 02:56 - 03:51	10,367,282	64.0	T1 FD int, T2 FD/9990, T4 Scaler
5360	14	2003/02/12, 04:03 - 04:58	10,140,807	64.0	T1 FD int, T2 FD/9990, T4 Scaler
5361	14	2003/02/12, 05:00 - 05:59	10,116,176	64.0	T1 FD int, T2 FD/9990, T4 Scaler
5362	14	2003/02/12, 06:00 - 06:58	10,399,196	64.0	T1 FD int, T2 FD/9990, T4 Scaler
5363	14	2003/02/12, 06:58 - 08:04	11,333,492	64.0	T1 FD int, T2 FD/9990, T4 Scaler

Runs used in the analysis of the beam momentum of 2.358 GeV/c.

Run	Tape	Time	Events	$I_{beam}[10^9/s]$	Trigger
5212	2	2003/01/27, 14:56 - 15:35	5,990,563	23.0	T1 FD int, T2 FD/999, T4 Scaler
5213	2	2003/01/27, 15:39 - 16:56	12,028,271	23.0	T1 FD int, T2 FD/999, T4 Scaler
5214	2	2003/01/27, 16:57 - 18:09	10,300,115	23.0	T1 FD int, T2 FD/999, T4 Scaler
5215	2	2003/01/27, 18:11 - 19:22	11,200,771	23.0	T1 FD int, T2 FD/999, T4 Scaler
5216	2	2003/01/27, 19:24 - 20:29	10,162,713	23.0	T1 FD int, T2 FD/999, T4 Scaler
5217	2	2003/01/27, 20:30 - 21:43	10,143,742	23.0	T1 FD int, T2 FD/999, T4 Scaler
5218	2	2003/01/27, 21:45 - 22:00	10,043,759	23.0	T1 FD int, T2 FD/999, T4 Scaler
5219	2	2003/01/27, 23:02 - 00:15	10,037,176	20.0	T1 FD int, T2 FD/999, T4 Scaler
5220	2	2003/01/28, 00:16 - 01:30	10,005,212	20.0	T1 FD int, T2 FD/999, T4 Scaler
5221	2	2003/01/28, 01:30 - 02:48	10,018,096	20.0	T1 FD int, T2 FD/999, T4 Scaler
5222	2	2003/01/28, 02:48 - 03:09	2,906,221	20.0	T1 FD int, T2 FD/999, T4 Scaler
5223	2	2003/01/28, 03:13 - 04:21	10,045,860	20.0	T1 FD int, T2 FD/999, T4 Scaler
5224	3	2003/01/28, 04:33 - 05:45	10,019,495	20.0	T1 FD int, T2 FD/999, T4 Scaler
5225	3	2003/01/28, 05:46 - 06:56	10,121,319	20.0	T1 FD int, T2 FD/999, T4 Scaler
5226	3	2003/01/28, 06:58 - 08:22	10,113,595	20.0	T1 FD int, T2 FD/999, T4 Scaler
5227	3	2003/01/28, 08:24 - 08:27	283,783	14.0	T1 FD int, T2 FD/999, T4 Scaler
5228	3	2003/01/28, 09:05 - 09:36	6,194,908	59.9	T1 FD int, T2 FD/999, T4 Scaler
5280	8	2003/02/02, 14:10 - 14:32	1,692,354	26.0	T1 FD int, T2 FD/9990, T4 Scaler
5281	8	2003/02/02, 14:48 - 16:27	10,415,304	36.0	T1 FD int, T2 FD/9990, T4 Scaler
5282	8	2003/02/02, 16:29 - 18:15	10,563,485	27.0	T1 FD int, T2 FD/9990, T4 Scaler
5283	8	2003/02/02, 18:16 - 19:56	8,566,111	27.0	T1 FD int, T2 FD/9990, T4 Scaler
5284	8	2003/02/02, 20:02 - 20:53	4,686,160	25.0	T1 FD int, T2 FD/9990, T4 Scaler
5285	9	2003/02/02, 21:21 - 22:52	9,893,760	36.0	T1 FD int, T2 FD/9990, T4 Scaler
5286	9	2003/02/02, 22:56 - 00:22	10,115,177	40.0	T1 FD int, T2 FD/9990, T4 Scaler
5287	9	2003/02/03, 00:23 - 01:32	7,137,838	40.0	T1 FD int, T2 FD/9990, T4 Scaler
5288	9	2003/02/03, 01:33 - 03:03	11,888,076	44.5	T1 FD int, T2 FD/9990, T4 Scaler
5289	9	2003/02/03, 03:05 - 04:36	11,690,509	44.5	T1 FD int, T2 FD/9990, T4 Scaler
5290	9	2003/02/03, 04:37 - 06:01	10,006,652	44.0	T1 FD int, T2 FD/9990, T4 Scaler
5291	9	2003/02/03, 06:02 - 07:11	8,589,695	44.0	T1 FD int, T2 FD/9990, T4 Scaler
5292	9	2003/02/03, 07:22 - 08:41	10,359,749	50.0	T1 FD int, T2 FD/9990, T4 Scaler

Bibliography

[1] A. Pevsner et al., *Evidence for a three pion resonance near 550 MeV*, Phys. Rev. Lett. **7** (1961) 421.

[2] Encyclopedia Britannica Online (www.britannica.com), entry 'meson'.

[3] G. Miller et al., *Charge Symmetry, Quarks and Mesons*, Phys. Rept. **194** (1990) 1.

[4] E. Stephenson et al., *Observation of the Charge Symmetry Breaking* $d+d \rightarrow {}^4He + \pi^o$ *Reaction Near Threshold*, Phys. Rev. Lett. **91** (2003) 142302.

[5] K. Hagiwara et al., *Review of Particle Physics*, Phys. Rev. **D66** (2002) 010001, and 2003 partial update for edition 2004 (http://pdg.lbl.gov).

[6] A. Lai et al., NA48, *New measurements of the* η *and* K^0 *masses*, Phys. Lett. **B533** (2002) 196.

[7] M. Abdel-Bary et al., GEM collaboration, *A precision determination of the mass of the* η *meson*, (2005), hep–ex/0505006, accepted by Phys. Lett.

[8] L.C. Liu and Q. Haider, *Signature for the existence of* η *mesic nucleus*, Phys. Rev. **C34** (1986) 1845.

[9] Q. Haider and L.C. Liu, *Formation of an* η *mesic nucleus*, Phys. Lett. **B172** (1986) 257.

[10] H.C. Chiang, E. Oset and L.C. Liu, *The width of bound* η *in nuclei*, Phys. Rev. **C44** (1991) 738.

[11] R. Chrien et al., *Search For Bound States Of The* η *Meson In Light Nuclei*, PRL **60** (1988) 2595.

[12] B.J. Lieb et al., GEM collaboration, *Search for Bound States of the* η *Mesons in Nuclei*, COSY proposal 50, http://www.fz-juelich.de/ikp/gem/Proposals/eta2000.ps, 2000.

[13] C. Wilkin, *Near threshold production of* η *mesons*, Phys. Rev. **C47** (1993) 938.

[14] S. Wycech, A.M. Green and J.A. Niskanen, *Are there* η *helium bound states?*, Phys. Rev. **C52** (1995) 544.

[15] A. Fix and H. Arenhövel, *η–3N problem with separable interactions*, Phys. Rev. **C66** (2002) 024002.

[16] S.A. Rakityansky, S.A. Sofianos, V.B. Belyaev and W. Sandhas, *On the possibility of an* η *meson light nucleus bound state formation*, Few Body Syst. Suppl. **9** (1995) 227.

[17] S.A. Rakityansky, S.A. Sofianos, M. Braun, V.B. Belyaev and W. Sandhas, *Quasi-bound states of* η *nucleus systems*, Phys. Rev. **C53** (1996) 2043.

[18] V.A. Tryasuchev, *On the existence of light η mesic nuclei*, Phys. Atom. Nucl. **60** (1997) 186.

[19] N. Willis et al., *η–helium quasi–bound states*, Phys. Lett. **B406** (1997) 14.

[20] J. Berger et al., *Identification of the $d+p \to {}^3He{+}\eta$ Reaction Very Near Threshold: Cross Section and Deuteron Tensor Analyzing Power*, Phys. Rev. Lett. **61** (1988) 919.

[21] B. Mayer et al., *The Reactions $pd \to {}^3He\eta$ and $pd \to {}^3He\pi^+\pi^-$ near the η threshold*, Phys. Rev. **C53** (1996) 2068.

[22] M. Betigeri et al., GEM collaboration, *Measurement of $pd \to {}^3He\eta$ in S(11) resonance*, Phys. Lett. **B472** (2000) 267.

[23] R. Bilger et al., *Measurement of the $pd \to {}^3He\eta$ cross section between 930 and 1100 MeV*, Phys. Rev. **C65** (2002) 044608.

[24] H.H. Adam et al., *New results on the $pd \to {}^3He\eta$ production near threshold*, Int. J. Mod. Phys. **A20** (2005) 643.

[25] R. Frascaria et al., *Total $dd \to {}^4He\eta$ cross–sections near threshold*, Phys. Rev. **C50** (1994) 537.

[26] R. Kessler, PhD thesis, UCLA, 1992.

[27] P. Berthet et al., *Very backward π^o and η^o production by proton projectiles on a deuterium target at intermediate energies*, Nucl. Phys. **A443** (1985) 589.

[28] J. Banaigs et al., *Observation of the ABC effect in the reaction $dd \to \alpha(mm)^0$*, Phys. Lett. **B43** (1973) 535.

[29] V.H. Long, PhD thesis, Universitè de Paris VI, 1976.

[30] T. Kirchner, PhD thesis, Universitè de Paris (Orsay), 1993.

[31] F. Roudot, PhD thesis, IPN Orsay, 1995.

[32] G. Fäldt, T. Johansson and C. Wilkin, *Near threshold production of η and η' mesons in p p and p d collisions*, Phys. Scripta **T99** (2002) 146.

[33] M.A. Pickar et al., *Near threshold proton induced neutral pion production from deuterium*, Phys. Rev. **C46** (1992) 397.

[34] V.N. Nikulin et al., *The $\vec{d}p \to {}^3He\pi^0$ reaction near threshold*, Phys. Rev. **C54** (1996) 1732.

[35] M. Goldberger and K. Watson, Collision Theory (John Wiley & Sons, Inc., NewYork, London, Sydney, Toronto, 1964).

[36] J.R. Taylor, Scattering Theory (John Wiley & Sons, Inc., New York, London, Sydney, Toronto, 1972).

[37] V. Baru et al., *Charge symmetry breaking as a probe for the real part of $\eta-$nucleus scattering length*, Phys. Rev. **C68** (2003) 035203.

[38] A. Sibirtsev, J. Haidenbauer, C. Hanhart and J.A. Niskanen, *The η^3He scattering length revisited*, Eur. Phys. J. **A22** (2004) 495.

[39] J.C. Peng et al., *Coherent η meson production in the reaction $\pi^- + {}^3He \to \eta + t$*, Phys. Rev. Lett. **63** (1989) 2353.

[40] V. Hejny et al., *Near threshold photoproduction of η mesons from ^{4}He.*, Eur. Phys. J. **A6** (1999) 83.

[41] M. Pfeiffer et al., *Photoproduction of η–mesic ^3He*, Phys. Rev. Lett. **92** (2004) 252001.

[42] A. Sibirtsev, J. Haidenbauer, J.A. Niskanen and U.G. Meissner, *Bounds on the bound η^3He system*, Phys. Rev. **C70** (2004) 047001.

[43] J.M. Laget and J.F. Lecolley, *Direct Evidence for Three–Body Mechanisms in the $p+\vec{d} \to {}^3He+\eta$ Reaction*, Phys. Rev. Lett. **61** (1988) 2069.

[44] J.F. Germond and C. Wilkin, *The $pd \to {}^3He\eta$ reaction at threshold*, J. Phys. **G15** (1989) 437.

[45] K. Kilian and H. Nann, Particle Production Near Threshold, edited by H. Nann and E. Stephenson, , AIP Conference Proceedings No. 221, p. 185, 1990.

[46] G. Fäldt and C. Wilkin, *The reaction $pd \to {}^3He\eta$ near threshold*, Nucl. Phys. **A587** (1995) 769.

[47] G. Fäldt and C. Wilkin, *The $dd \to {}^4He\eta$ Reaction Near Threshold*, Nucl. Phys. **A596** (1996) 488.

[48] C. Wilkin, private communication.

[49] R. Maier et al., *Cooler synchrotron COSY*, Nucl. Phys. **A626** (1997) 395c.

[50] U. Bechstedt et al., *Operating Report of COSY in 2000*, IKP/COSY, Annual Report 2000, Jül–3852, 2001.

[51] S. Barsov et al., *ANKE, a new facility for medium energy hadron physics at COSY–Jülich*, Nucl. Inst. and Meth. **A462** (2001) 364.

[52] H. Dombrowski et al., *The Münster cluster target for internal storage ring experiments*, Nucl. Inst. and Meth. **A386** (1997) 228.

[53] R. Engels et al., *First Polarization Measurement of Hydrogen Atoms Effusing from a Storage Cell into the Lamb–Shift Polarimeter and the Removal of the Components of the Polarized Target to COSY*, IKP/COSY, Annual Report 2004, Jül–4168, 2005.

[54] COSY–11 collaboration, *Drift Chambers with Double Sense Wires for the COSY–11 Facility*, IKP/COSY, Annual Report 1995, Jül–3200, 1996.

[55] R. Schleichert and A. Selikov, *RALEX module – 16 Channel Constant Fraction Discriminator – 8 Channel Meantimer*, KFA–Jülich, Internal report, 1996.

[56] S.N. Dymov et al., *Trigger electronics for the forward and backward hodoscopes of ANKE*, JINR Dubna, Communication of JINR, E10–2002–19, 2002.

[57] A. Wrońska et al., *Simulations of the $dd \to \alpha\eta$ reaction at* ANKE, IKP/COSY, Annual Report 2001, Jül–3978, 2002.

[58] GEANT team, CERN, Geneva, GEANT – Detector Description and Simulation Tool, 1994, CERN Program W5013.

[59] A. Gårdestig, G. Fäldt and C. Wilkin, *An explanation of the ABC enhancement in the $dd \to \alpha X$ reaction at intermediate energies*, Phys. Lett. **B421** (1998) 41.

[60] R. Wurzinger et al., *Study of the ABC enhancement in the $\vec{d}d \to \alpha X^0$ reaction*, Phys. Lett. **B445** (1999) 423.

[61] M.A. Kagarlis, *Pluto++ – a Monte Carlo simulation tool for hadronic physics*, http://www-hades.gsi.de/computing/pluto/html/PlutoIndex.html, 2000.

[62] J. Banaigs et al., *A study of the inclusive reaction $d+d \to {}^4He+X$ the ABC effect, and I=0 meson resonances*, Nucl. Phys. **B105** (1976) 52.

[63] F. Sauli, *Principle of operation of multiwire proportional and drift chambers*, CERN 77–09.

[64] V. Hejny et al., *RootSorter: A New Analysis Framework For ANKE*, IKP/COSY, Annual Report 2002, Jül–4052, 2003.

[65] R. Brun et al., ROOT. An Object–Oriented Data Analysis Framework, CERN, Geneva, 2003, ftp://root.cern.ch/root/doc/Users_Guide_3_10.pdf.

[66] A. Volkov et al., *Method for the calculation of charged particle momentum in magnetic spectrometers*, Nucl. Inst. and Meth. **A306** (1991) 278.

[67] V. Artemov et al., *Particle parameter determination at the ANKE spectrometer*, IKP/COSY, Annual Report 1996, Jül–3365, 1997.

[68] G. Macharaschvili, *Scintillation Counter Response Calibration*, ANKE internal report, http://www.fz-juelich.de/ikp/anke/en/internal_notes/FD_scintillator_calibration_7-2002.ps.gz, 2002.

[69] H. Stein and D. Prasuhn, *Determination of Effective Target Thickness and Luminosity from Beam Energy Losses at the ANKE Cluster Target*, IKP/COSY, Annual Report 2001, Jül–3978, 2002.

[70] A. Khoukaz and T. Mersmann, private communication.

[71] G. Bizard et al., *Experimental study and baryonic exchange interpretation of the reaction $^{2}H(d,n)^{3}He$ in the intermediate–energy region*, Phys. Rev. **C22** (1980) 1632.

[72] E. Byckling and K. Kajantie, Particle Kinematics (John Wiley & Sons, London, New York, Sydney, Toronto, 1973).

[73] H. Machner et al., GEM collaboration, *Study of η–Meson Production in the $\vec{d}+d \rightarrow \alpha+\eta$ Reaction*, COSY proposal 124, http://www.fz-juelich.de/ikp/gem/Proposals/dd2alphaeta.pdf, 2003.

Acknowledgements

Last but not least in this dissertation I want to express my gratitude to those, who supported me in various ways in the course of my PhD studies.

I owe my gratitude to Prof. Hans Ströher for giving me the opportunity to work in his group in Forschungszentrum Jülich and for his kind interest and help in my work in all its phases.

Dr. Volker Hejny, my tutor during the stay in Jülich, as well as a great workmate and unequalled master of systematic experimental work shared with me many hours spent at the experiment and was indispensable during the data analysis. Thank you for your patience in answering the thousands of my questions! ☺

Prof. Andrzej Magiera, the supervisor of my PhD studies, helped me to find an interesting topic. I am also obliged to him for discussing with me the many problems concerning the experiment as well as the analysis.

My Colleagues from Anke helped me to get acquainted with the detection setup as well as the software for the data analysis (in particular Dr. Volker Hejny) and for the simulations (Sergey Dymov). Many thanks for working with me shoulder to shoulder, motivating me when I needed it, and for our coffee-discussions which were quite good lessons in physics where one was not afraid to ask silly questions. I would not have managed without your continuous support…

I am grateful to Prof. Colin Wilkin for his advice concerning the theory behind our experiment, the fatherly attitude ☺, as well as for his eagerness to see the final results. That was really motivating!

My friends from Jülich: Arek Bubak, Agnieszka and Piotr Hawranek, Ania and Tomek Rożek, other members of the 'Polish Mafia' as well as Vera Kleber, Peter Winter and Inti Lehmann. Thank you for the time outside of the institute and helping me to keep my sense of perspective…

I would like to thank My Parents for their love and emotional assistance (though no words will express it…).

I am grateful to My dear husband Wojtek for moving to Jülich with me for a couple of years and for his unconditional love and endless patience.

Podziękowania

W tym miejscu chcę wyrazić moją wdzięczność wszystkim tym, którzy na różne sposoby wspierali mnie podczas moich studiów doktoranckich.

Winna jestem wdzięczność Prof. Hansowi Ströherowi za przyjęcie mnie do swojej grupy eksperymentalnej w Centrum Badawczym Jülich i za jego życzliwe zainteresowanie i pomoc na wszystkich etapach mojej pracy.

Dr Volker Hejny, mój opiekun naukowy podczas pobytu w Jülich, jak również wspaniały kolega i niezrównany mistrz systematycznej pracy doświadczalnej dzielił ze mną godziny spędzone przy eksperymencie i był niezastąpiony podczas analizy danych. Dziękuję Ci za Twoją cierpliwość w odpowiadaniu na tysiące moich pytań! ☺

Prof. Andrzej Magiera, mój promotor, okazał pomoc przy wyborze ciekawego tematu pracy doktorskiej. Jestem mu wdzięczna za wspólne poszukiwanie ze mną rozwiązań wielu problemów dotyczących zarówno eksperymentu jak i analizy danych.

Koledzy z grupy ANKE pomogli mi zapoznać się z układem eksperymentalnym, oprogramowaniem do analizy danych (tu szczególne zasługi dr. Volkera Hejnego) oraz do symulacji (nie sposób nie wymienić Sergeya Dymova). Wielkie dzięki za wspólną pracę, motywowanie mnie w chwilach kryzysu, a także za nasze dyskusje przy kawie, które bywały dobrymi lekcjami fizyki, kiedy to bez obaw kompromitacji można zadać dowolnie głupie pytanie. Nie poradziłabym sobie bez Waszej nieustannej pomocy…

Wdzięczna jestem także Prof. Colinowi Wilkinowi za jego rady dotyczące teoretycznych aspektów naszego eksperymentu, ojcowski stosunek do mnie ☺ oraz za niecierpliwość, z jaką oczekiwał wyników. To naprawdę działało motywująco!

Moi przyjaciele z czasów Jülich: Arek Bubak, Agnieszka i Piotr Hawranek, Ania i Tomek Rożek, pozostali członkowie 'Polskiej Mafii' jak również Vera Kleber, Peter Winter i Inti Lehmann. Dziękuję Wam za czas spędzony wspólnie poza murami instytutu i za pomoc w utrzymywaniu równowagi…

Chcę też podziękować moim Rodzicom za ich miłość i wsparcie emocjonalne (choć wiem, że żadne słowa nie są w stanie tego oddać…).

Dziękuję również mojemu drogiemu mężowi Wojtkowi za to, że przeprowadził się ze mną na parę lat do Jülich oraz za jego bezwarunkową miłość i nieskończoną cierpliwość.